

Unclassified

NEA/CSNI/R(2016)2

Organisation de Coopération et de Développement Économiques
Organisation for Economic Co-operation and Development

23-Feb-2016

English text only

**NUCLEAR ENERGY AGENCY
COMMITTEE ON THE SAFETY OF NUCLEAR INSTALLATIONS**

NEA/CSNI/R(2016)2
Unclassified

The Nuclear Energy Agency–Paul Scherrer Institut Computation Fluid Dynamics Benchmark Exercise

JT03390545

Complete document available on OLIS in its original format

This document and any map included herein are without prejudice to the status of or sovereignty over any territory, to the delimitation of international frontiers and boundaries and to the name of any territory, city or area.

English text only

ORGANISATION FOR ECONOMIC CO-OPERATION AND DEVELOPMENT

The OECD is a unique forum where the governments of 34 democracies work together to address the economic, social and environmental challenges of globalisation. The OECD is also at the forefront of efforts to understand and to help governments respond to new developments and concerns, such as corporate governance, the information economy and the challenges of an ageing population. The Organisation provides a setting where governments can compare policy experiences, seek answers to common problems, identify good practice and work to co-ordinate domestic and international policies.

The OECD member countries are: Australia, Austria, Belgium, Canada, Chile, the Czech Republic, Denmark, Estonia, Finland, France, Germany, Greece, Hungary, Iceland, Ireland, Israel, Italy, Japan, Luxembourg, Mexico, the Netherlands, New Zealand, Norway, Poland, Portugal, the Republic of Korea, the Slovak Republic, Slovenia, Spain, Sweden, Switzerland, Turkey, the United Kingdom and the United States. The European Commission takes part in the work of the OECD.

OECD Publishing disseminates widely the results of the Organisation's statistics gathering and research on economic, social and environmental issues, as well as the conventions, guidelines and standards agreed by its members.

NUCLEAR ENERGY AGENCY

The OECD Nuclear Energy Agency (NEA) was established on 1 February 1958. Current NEA membership consists of 31 countries: Australia, Austria, Belgium, Canada, the Czech Republic, Denmark, Finland, France, Germany, Greece, Hungary, Iceland, Ireland, Italy, Japan, Luxembourg, Mexico, the Netherlands, Norway, Poland, Portugal, the Republic of Korea, the Russian Federation, the Slovak Republic, Slovenia, Spain, Sweden, Switzerland, Turkey, the United Kingdom and the United States. The European Commission also takes part in the work of the Agency.

The mission of the NEA is:

- to assist its member countries in maintaining and further developing, through international co-operation, the scientific, technological and legal bases required for a safe, environmentally friendly and economical use of nuclear energy for peaceful purposes;
- to provide authoritative assessments and to forge common understandings on key issues, as input to government decisions on nuclear energy policy and to broader OECD policy analyses in areas such as energy and sustainable development.

Specific areas of competence of the NEA include the safety and regulation of nuclear activities, radioactive waste management, radiological protection, nuclear science, economic and technical analyses of the nuclear fuel cycle, nuclear law and liability, and public information.

The NEA Data Bank provides nuclear data and computer program services for participating countries. In these and related tasks, the NEA works in close collaboration with the International Atomic Energy Agency in Vienna, with which it has a Co-operation Agreement, as well as with other international organisations in the nuclear field.

This document and any map included herein are without prejudice to the status of or sovereignty over any territory, to the delimitation of international frontiers and boundaries and to the name of any territory, city or area.

Corrigenda to OECD publications may be found online at: www.oecd.org/publishing/corrigenda.

© OECD 2016

You can copy, download or print OECD content for your own use, and you can include excerpts from OECD publications, databases and multimedia products in your own documents, presentations, blogs, websites and teaching materials, provided that suitable acknowledgment of the OECD as source and copyright owner is given. All requests for public or commercial use and translation rights should be submitted to rights@oecd.org. Requests for permission to photocopy portions of this material for public or commercial use shall be addressed directly to the Copyright Clearance Center (CCC) at info@copyright.com or the Centre français d'exploitation du droit de copie (CFC) contact@cfcopies.com.

COMMITTEE ON THE SAFETY OF NUCLEAR INSTALLATIONS

The NEA Committee on the Safety of Nuclear Installations (CSNI) is an international committee made up of senior scientists and engineers with broad responsibilities for safety technology and research programmes, as well as representatives from regulatory authorities. It was created in 1973 to develop and co-ordinate the activities of the NEA concerning the technical aspects of the design, construction and operation of nuclear installations insofar as they affect the safety of such installations.

The committee's purpose is to foster international co-operation in nuclear safety among NEA member countries. The main tasks of the CSNI are to exchange technical information and to promote collaboration between research, development, engineering and regulatory organisations; to review operating experience and the state of knowledge on selected topics of nuclear safety technology and safety assessment; to initiate and conduct programmes to overcome discrepancies, develop improvements and reach consensus on technical issues; and to promote the co-ordination of work that serves to maintain competence in nuclear safety matters, including the establishment of joint undertakings.

The priority of the CSNI is on the safety of nuclear installations and the design and construction of new reactors and installations. For advanced reactor designs, the committee provides a forum for improving safety-related knowledge and a vehicle for joint research.

In implementing its programme, the CSNI establishes co-operative mechanisms with the NEA Committee on Nuclear Regulatory Activities (CNRA), which is responsible for issues concerning the regulation, licensing and inspection of nuclear installations with regard to safety. It also co-operates with other NEA Standing Technical Committees, as well as with key international organisations such as the International Atomic Energy Agency (IAEA), on matters of common interest.

EXECUTIVE SUMMARY

The OECD Nuclear Energy Agency-Paul Scherrer Institut (NEA-PSI) Benchmark was initiated to test the capability of state-of-the-art Computational Fluid Dynamics (CFD) and dedicated containment codes to predict the important physical processes occurring in a containment volume following a postulated severe accident in which there is a significant build-up of hydrogen in the containment atmosphere.

To provide a suitable experimental data base for the benchmark exercise, a new test was carried out during February-March 2013 within one, comprehensively-instrumented vessel of the PANDA integral containment facility, located at PSI in Switzerland. The facility had been used in the past within the context of several NEA-sponsored benchmarking initiatives, and as a result the members of the PANDA experimental team have acquired considerable experience in performing containment tests of the type required here. However, some extra care was needed in this case: namely, that precise information on measurement error, jet injection boundary conditions, was provided in a consistent package, which made up the benchmark specifications. Also, the invitation to participate was made to a wider audience, since this test was 100% PSI funded.

This benchmark was specifically aimed at examining the erosion of a hydrogen-rich, stratified layer, occupying the upper reaches of a containment volume, by the impingement of a buoyant, vertical jet, placed off-centre with respect to the axis of the vessel, this to induce significant three-dimensional motions in the flow. The test itself was carried out at room temperature; helium and air were used as simulant gases, a helium-rich layer of gas at the top providing the initial upper-vessel stratification. The buoyancy of the jet (with respect to the air initially surrounding it) was provided by an increased helium concentration at injection, and with a slightly elevated temperature. The test instrumentation consisted of temperature and gas concentration measurements at strategic locations throughout the volume, and by PIV (Particle Imaging Velocimetry) measurements of two (vertical and lateral) velocity components in the jet expansion and interaction region.

Participants in the benchmark were given precise details of the test geometry, by way of official design drawings and, to aid mesh generation, CAD (Computer-Aided Design) files in standard formats. In addition, the material properties of the gases in the containment atmosphere (air and helium) were also provided, together with those of all the steel structures making up the confinement. Initial test conditions, in terms of the gas concentrations at all elevations in the vessel, the temperature conditions, and gas concentration and velocity profiles at the exit to the injection line were also given. To prevent pressurization, a venting system was introduced at the base of the vessel, far beneath the zone of interest. Nevertheless, adequate details of this arrangement were also provided.

Test conditions were chosen so that complete erosion of the stratified layer would occur within a two-hour period following initiation of the jet flow. Numerical data were requested at specified intervals during the transient, at the precise locations at which measurements had been made, and where the data were meaningful. Both mean and rms (root-mean-square) quantities were requested by the benchmark organisers. A special ftp (file transfer protocol) site was set up at PSI, where all the geometry and initial flow data were stored, ready for downloading. This site also operated as a *Dropbox*, where participants eventually uploaded their numerical data sets.

An organising committee was set up early in 2013 to oversee the benchmark exercise. Detailed specifications were drawn up ahead of a formal announcement of the benchmark activity, and an invitation to attend a kick-off meeting, held on April 26, 2013 at the NEA headquarters in Paris, was sent out to more than 750 (potentially) interested parties. Of these, 49 formally registered interest in the exercise, and consequently all received the detailed specifications and associated CAD files. The specifications also included instructions for the standard formatting of the requested data files, this to facilitate easy processing of the numerical data once it had been uploaded to the ftp site.

The specifications were finalized on 31 July 2013, and a deadline date of 30 May 2014 was set for participants to present their numerical data files to the organisers for synthesis. An Open Meeting was subsequently convened on 4 June 2014, again taking place at the NEA HQ in Paris, at which time the test data were opened for the first time. Participants were warned that if they had made the decision to present their blind predictions by the stipulated deadline, they would not later be able to withdraw or update them following release of the measured test data, and that their blind numerical predictions would subsequently be included in the synthesis procedure.

Of the 49 officially registered participants, 29 actually requested a username and password on the PSI ftp site. Of these, 19 submitted blind CFD results by the deadline date, and these have consequently been included in the synthesis report, which was presented as an invited paper at the joint OECD/NEA-IAEA CFD4NRS-5 Workshop held at ETH Zurich on 9-11 Sept. 2014. Of the simulation results submitted, the majority (twelve) were obtained using the three major commercial CFD software packages: ANSYS CFX, FLUENT and STAR-CCM+. The rest were derived from the open-source software OpenFOAM (one), various in-house CFD codes (four) and from the dedicated containment modelling code GOTHIC (two). These same participants, in return for their participation, were offered full access to the test data.

The principal conclusions arising from this exercise are:

- Containment modelling still remains a significant challenge for CFD codes, and those who use them, even in the absence of complex physical phenomena such as phasic exchange; i.e. steam condensation.
- As a consequence of the computational overhead associated with simulating a long transient in a large confinement volume, strict application of Best Practice Guidelines (BPGs) is unworkable at the present time.
- As a consequence of this shortfall, a good measure of experience is needed on the part of the numerical analyst. Not surprisingly, therefore, best comparisons were obtained from those with previous experience in the simulation of the erosion of stratified layers, particularly in the context of previous PANDA tests.
- The present state-of-the-art in turbulence modelling in terms of RANS (Reynolds- Averaged Navier-Stokes) formulations appears to be adequate for simulations of this type.
- The employment of advanced turbulence models, such as LES (Large-Eddy Simulation), which is anyway unnecessarily time consuming, or RSM (Reynolds Stress Modelling), which sometimes can induce numerical instabilities, appears not to be a prime requisite here.
- Very few of the modellers appear to have demonstrated that they can accurately reproduce the spreading and subsequent decay of a free jet in undisturbed surroundings, as occurs in this present transient, at least at early times. There is a wealth of experimental data on this. Unless the jet-spreading process is properly captured, the timing of all other events will suffer as a consequence. Was this simple pre-requisite of accurate modelling properly investigated?

- Results as good as the best CFD analyses were obtained by one user of the GOTHIC containment code using (relative to CFD) very coarse meshing. However, the far worse results obtained by the other GOTHIC user imply that the success of such coarse-mesh approaches depends strongly on user experience.
- Perhaps it is worth pointing out that the two overall “best” results were both obtained using the Scale-Adaptive Simulation (SAS) turbulence model, in total contrast to the OECD-Vattenfall T-junction benchmark, in which use of this model consistently filled the lowest ranking positions.

In summary, the benchmark exercise, like its predecessors, has proven to be very popular, topical, and of international appeal. First-class experimental data were obtained from the PANDA test by a specialist team of highly professional people, all with previous experience in the field. They produced error estimates on their actual data measurements — such information is invaluable to those given the task of evaluating the accuracy of the numerical predictions, and quantifying them in terms of a ranking procedure. Synthesis of the results was also undertaken by someone with previous relevant experience. Since all the participants were granted full anonymity in this exercise, the authors of this document consider it is within their competence to reach the conclusions given, independently of the participants’ input. However, provision has been made for all participants to express their individual opinions on how they consider the benchmark exercise to have been conducted and/or evaluated. The comments received have been reproduced verbatim in Annex 4 of this report.

Resources are not available to organize and evaluate an ‘open’ benchmark exercise based on this test (i.e., one for which the test data are available before the numerical simulations are carried out), but it is hoped that many participants will take the opportunity to use the highly valuable test data they now have at their disposal to improve the quality of their blind numerical predictions, and report their experiences accordingly in the open literature.

ACKNOWLEDGEMENT

This report was prepared by and this benchmark led by B.L. Smith, M. Andreani, R. Kapulla, A. Badillo, G. Mignot and S. Paranjape of the Thermal Hydraulics Laboratory at the Paul Scherrer Institute (PSI). The experiment was performed by and the data for the benchmark were provided by PSI. M.P. Kissane was the NEA official responsible.

TABLE OF CONTENTS

1. MOTIVATION AND BACKGROUND	13
1.1 The CFD4NRS Workshop Series.....	14
1.2 Construction of the CFD for NRS Wiki Pages	14
1.3 Benchmark Exercise on Thermal Fatigue	15
1.4 Benchmark Exercise on Turbulence in a Rod Bundle Generated by Spacer Grids	15
1.5 Benchmark Exercise on Erosion of a Stratified Layer by a Buoyant Jet in a Large Volume	16
2. ORGANISATIONAL PROCEDURES	19
2.1 CSNI Approval	19
2.2 The Work of the Benchmark Organising Committee	20
3. EXPERIMENTAL FACILITY	23
3.1 General Layout.....	23
3.2 Instrumentation	24
3.3 Initial and boundary conditions.....	25
3.4 Inlet tube exit velocities	27
3.5 In-vessel measurements	31
3.6 Summary of experimental findings.....	37
4. COMPUTATIONS	39
4.1 Introduction.....	39
4.2 Summary of submissions	39
4.3 Available data for comparison	42
5. SYNTHESIS OF RESULTS	45
5.1 Main results and comparisons.....	45
5.2 Ranking of the submissions	52
5.2.1 Ranking based on comparisons of stratification layer erosion time.....	52
5.2.2 Ranking by comparison with all helium concentration time histories	53
5.2.3 Ranking by comparison with PIV data.....	54
5.2.4 Ranking by comparison with temperatures	56
5.3 Global ranking.....	57
5.4 Comparison between selected variables for the highest-ranking simulations.....	59
5.5 Summary of the synthesis of results.....	62
6. FINAL REMARKS	65
Acknowledgments	67
References	68

ANNEX 1: Announcement OECD/NEA sponsored CFD Benchmark exercise:	
erosion of a stratified layer by a buoyant jet in a large volume	71
ANNEX 2: Specifications OECD/NEA—PSI CFD Benchmark specifications final version	75
A0. PRELIMINARY REMARKS	75
A1. GEOMETRICAL INFORMATION	77
A1.1 Experimental Test Section.....	77
A1.2 Details of the Gas Injection and Vent Line Arrangements.....	79
A2. MATERIAL PROPERTIES	81
A3. INITIAL AND BOUNDARY CONDITIONS	82
A4. NUMERICAL DATA REQUESTED.....	92
A4.1 Introduction	92
A4.2 Coordinate System Used for Reporting.....	93
A4.3 Location of Instrumentation	93
A4.4 Data File Formats	97
A4.5 Basic Information of Numerical Model and Method of Solution	100
A6. CONCLUDING REMARKS	101
A6.1 Organizing Committee	101
A6.2 Schedule	101
A6.3 Submittal Procedures.....	102
A7. List of attachments referenced in the text and available on the ftp site	102
A8. Tables of measured injection line velocity profiles	103
ANNEX 3: Nomenclature	113
ANNEX 4: Comments from participants	115

1. MOTIVATION AND BACKGROUND

A meeting jointly sponsored by the IAEA* and the OECD/NEA‡: *An Exploratory Meeting of Experts to Define an Action Plan on the Application of Computational Fluid Dynamics (CFD) Codes to Nuclear Reactor Safety (NRS) Problems*, took place in Aix-en-Provence, France on 15-16 May, 2002 [1]. Thereafter a follow-up meeting took place: *Use of Computational Fluid Dynamics (CFD) Codes for Safety Analysis of Reactor Systems including Containment*, convened in Pisa, Italy on 11-14 Nov., 2002 [2]. These joint meetings resulted in the formulation of an action plan recommending the creation of three Writing Groups, whose work would be overseen by the WGAMA# committee of the OECD/NEA, and with mandates to carry out the following tasks:

- WG1 Provide a set of guidelines for the application of CFD to NRS problems;
- WG2 Evaluate the existing CFD assessment base, identify any gaps, and initiate activities aimed at broadening the assessment database;
- WG3 Summarise the extensions needed to CFD codes for application to two-phase NRS problems.

Work began early in 2003. Teams of experts were assigned to each of the groups, representing the following OECD member countries: the Czech Republic, France, Germany, Italy, Japan, S. Korea, the Netherlands, Norway, Sweden, Switzerland and the USA. Preliminary reports were submitted to the WGAMA group in September 2004. These scoped the work needed to be carried out to fulfil the respective mandates, and also made recommendations on how to achieve the defined objectives. In January 2005, all three groups were reformed to carry out their respective assignments. The work was concluded in December 2007, and CSNI reports were eventually issued by each group describing the work undertaken [3,4,5].

The WG2 Writing Group provided evidence to show that CFD is a tried-and-tested technology, and that the main industrial-level CFD vendors were themselves taking active steps to quality assure their software products by testing them against standard test data, and through active participation in international benchmarking exercises. However, in a period of low growth in the nuclear power industry (beginning in the 1980s), the primary driving forces for the development of CFD technology remained for several years in non-nuclear areas, such as in the aerospace, automotive, marine, turbo-machinery, chemical and process industries, and to a lesser extent the environmental and biomedical industries. In the power-generation arena, the principal applications were again non-nuclear: combustion dynamics for fossil-fuel burning and gas turbines, vanes for wind turbines, etc. A resurgence of interest in nuclear occurred from 2005 to 2011, a

*International Atomic Energy Agency

‡Organisation for Economic Cooperation and Development, Nuclear Energy Agency

#Working Group on the Analysis and Management of Accidents

period which coincided with the issue of the WG reports, but has now been interrupted again as a consequence of the Fukushima Daiichi accident on March 11, 2011.

During the period in which the WG2 group met, and accepting the commission to not only report on the existing assessment databases for the application of CFD to nuclear reactor safety issues, but to also take active steps to broaden and extend the databases, three new initiatives were proposed to WGAMA]:

1. To organise a new series of international workshops to provide a forum for experimenters and numerical analysts to meet and exchange information;
2. To encourage nuclear departments at universities and research organisations to release previously unpublished test data to form the basis of international numerical benchmarking exercises; and
3. To establish a Wiki-type web portal to give online access to the information collated by the WGs, as documented in their final reports, and, via user input, to provide a means for updating and extending the information they contained. A special *CFD Task Group* was subsequently convened by WGAMA for this purpose.

1.1 The CFD4NRS Workshop Series

The first of the international workshops took place in Garching, Germany in 2006 [6], and was organised directly by the WG2 group, which was still sitting at this time. Selected papers from the workshop were subsequently published in a special issue of Nuclear Engineering and Design [7]. Further workshops in the series, as well as the benchmarking and webpage initiatives, were organised by the smaller *CFD Bureau*, formed later by WGAMA. This group initially consisted of the chairmen of the three Writing Groups, together with the NEA secretariat currently assigned to this task.

The second workshop in the series, XCFD4NRS, took place in Grenoble, France in September 2008 [8], and concentrated more on the multi-phase aspects of CFD modelling, the prime focus of the WG3 Writing Group. The third workshop, CFD4NRS-3, was convened in Washington DC, USA in September 2010; the fourth, CFD4NRS-4, in Daejeon, Korea in September 2012, and the most recent, CFD4NRS-5, at the Swiss Federal Technical University (ETH), Zurich in September 2014. This last venue was chosen so that participants in the present benchmark could visit the PANDA facility at the Paul Scherrer Institute (PSI), and a fieldtrip was organised to this purpose on the last day of the workshop.

1.2 Construction of the CFD for NRS Wiki Pages

It was foreseen that the original CSNI documents [3,4,5], reporting the activities of the three Writing Groups, like any state-of-the-art reports, would only up-to-date at the time of writing, and, given the rapidly expanding use of CFD as a refined analysis tool in nuclear safety studies, the information they contained would soon become outdated. To preserve their usefulness and topicality, regular improvements and extensions to the documents would be necessary, and were set into motion. It was decided that the most efficient vehicle for updating the information would be to create a Wiki-type web portal. Consequently, in a pilot study, a dedicated webpage was created on the NEA website using Wikimedia software [9]. The WG1 and WG2 documents, in the forms they appeared in the respective archival documents [3,4], were subsequently uploaded to provide online access to the material they contained.

In a subsequent OECD/NEA initiative, carried out between 2010 and 2012, a specially convened CFD Task Force was organised under the auspices of WGAMA to update and extend the three original Writing Group (WG) documents. This resulted in the release in 2014 of a set of updated CSNI reports [10,11,12], which considerably extended the three areas covered by the original documents. While this work was in progress, and under the terms of an OECD/NEA-PSI sub-contract, the CFD webpages were also updated in 2014, and,

at the time of writing of this document, all the webpages are now fully consistent with the revised CSNI documents [13].

All the main chapters of the WG documents have been made active links to the subject material on the webpages, and these have been subdivided where necessary. Active links are installed at all levels to enable the user to navigate quickly to other parts of the respective documents. All webpage addresses, for example to the commercial CFD sites, are also active, and it is planned to install similar links for the journal references too, which would be useful for registered subscribers with electronic access to the material. However, the most useful feature of the web portal, as originally conceived, remains in place: it provides the opportunity to modify, correct, update and extend the information contained there, the Wiki environment being the primary vehicle for this. Of course, all modifications and extensions are subject to WGAMA and CSNI approval.

1.3 Benchmark Exercise on Thermal Fatigue

During a meeting of the three Writing Group chairmen convened in Grenoble in September 2008 at the conclusion of the 2nd of the workshops, XCFD4NRS [8], discussions were held concerning candidate experiments around which to organise a new international CFD benchmarking exercise; both single-phase and two-phase application areas were considered. It was generally acknowledged that it would be desirable to have the opportunity of performing a “blind” benchmark, in which the test data were not known in advance, and this would entail finding a completed experiment for which the data had not yet been released, or encouraging a new experiment (most likely in an existing facility) to be undertaken especially for this purpose. The group took on the responsibility of finding a suitable experiment, for providing the organisational basis for launching the benchmark exercise (though not on the scale of an International Standard Problem, ISP), and for the synthesis of the results. An early opportunity came in the area of high-cycle thermal fatigue associated with flow mixing in a T-junction. Vattenfall R&D, Älvkarleby, Sweden, agreed to release previously unpublished test data from one of their T-junction experiments in support of this benchmarking activity, and assigned the member of their staff who had performed the experiment to the OECD/NEA *CFD Bureau* to provide hands-on information to assist in the compilation of the test specifications.

The benchmark exercise was carried out, under the supervision of WGAMA, between 2009 and 2011, terminating in the issue of a full CSNI report [14], a paper delivered at the 14th Int. Topical Meeting on Nuclear Reactor Thermal Hydraulics (NURETH-14) in Toronto [15], an archival version of which subsequently appeared in the special issue of Nuclear Engineering and Design dedicated to this conference [16]. Of the 69 participants who originally registered interest in participating in the exercise, 29 submitted blind CFD results ahead of the deadline cut-off date, all of which were then included in the subsequent synthesis and ranking procedures. The full test data were then released to these participants, subject to them signing a property-rights agreement. The procedural steps established during the coordination of this benchmark activity have been used as a template for the two subsequent CFD benchmark exercises, the most recent of which constitutes the body of this document.

1.4 Benchmark Exercise on Turbulence in a Rod Bundle Generated by Spacer Grids

The Korea Atomic Energy Research Institute (KAERI) had formally participated in the T-junction benchmark exercise, and subsequently made approaches to the *CFD Bureau* with the offer of providing previously unpublished test data to serve as a basis for a benchmarking activity based on the issue of turbulent mixing downstream of a spacer grid in a rod bundle geometry. It was recognised that an international benchmarking activity of this nature would be welcome, since the design of spacer grids in fuel

rod bundles is highly proprietary information, this being true also in Korea, of course. However, KAERI were prepared, at their own expense, to design, manufacture and test, in their MATiS-H facility, spacer grids of a “generic” type, and offer the data to the CFD community in the framework of an OECD/NEA benchmarking activity. CAD files of two generic designs of grid spacer — of split-type and swirl-type — were also offered, as an aid to grid generation.

Tests were subsequently performed under single-phase, isothermal conditions, to focus attention on the turbulence characteristics of the flow generated by the two grid geometries to the exclusion of other complications, such as heat transfer, buoyancy, and two-phase flow conditions. High-quality Laser Doppler Velocimetry (LDV) techniques in three dimensions were employed to provide time-averaged (mean and rms) velocity data suitable for the assessment of the turbulence models incorporated in CFD codes. It is often stated, both within and outside the nuclear community, that turbulence modelling is the last mountain to climb in single-phase fluid dynamics, and this exercise, with its direct correspondence to fuel rod cooling and safety margins to CHF (Critical Heat Flux) — the ultimate limiting factor on core coolability — would provide a solid foundation for the use of CFD modelling approaches in this important design area.

Certainly, there had already been a considerable amount of research activity on the subject, e.g. [17-20], but till then no direct means to quantify the status of the application of CFD to the technology in terms of a blind comparison exercise had previously been undertaken. Following similar procedures to those used before, the benchmark exercise was carried out (under the supervision of WGAMA) between 2011 and 2013, resulting in the issue of a full CSNI report [21], and two papers delivered at the 15th Int. Topical Meeting on Nuclear Reactor Thermal Hydraulics (NURETH-15) in Pisa, Italy [22,23]. Of the 48 participants who originally registered interest in participating, 25 submitted blind CFD results ahead of the cut-off date prior to the test data being opened, all of which were then included in the subsequent synthesis and ranking procedures. Again, the participants were rewarded for their efforts by being supplied these valuable test data.

1.5 Benchmark Exercise on Erosion of a Stratified Layer by a Buoyant Jet in a Large Volume

This benchmark derives from the need to quantitatively assess the potential of the hydrogen generated during a severe accident, following core degradation, to form an explosive mixture in the upper part of the containment, and the subsequent penetration and erosion of this hydrogen-rich layer, induced by buoyant jets rising from beneath. The 3-D nature of the flow generated invites the use of CFD (or CFD-type) approaches, but such applications are often restricted by the lack of adequate validation data of the basic physical phenomena at the appropriate scale. The benchmark therefore aimed to provide invaluable data in the quest to improve the reliability of numerical simulation approaches in such situations. The recent accident at the Fukushima Daiichi complex in Japan in March 2011 has refocused attention on this issue globally.

The benchmark is based on an experiment carried out in March/April 2013 in the PANDA facility at the Paul Scherrer Institute (PSI), Switzerland. One of the drywell tanks was isolated from the rest of the facility for this purpose. Prior to the test, the vessel (volume approximately 90 m³) was filled with air and helium, at rest, in a stably-stratified configuration at a uniform temperature of around 20°C, and at atmospheric pressure. At the start of the transient, a helium/air mixture, at a mildly elevated temperature, was injected into the volume via a vertical pipe off-set from the central axis of the vessel, this to generate important three-dimensional motions in the containment atmosphere, and to thereby create a need for three-dimensional numerical simulation.

The benchmark aimed to examine the turbulent mixing of a two-component gas mixture (air and helium), driven by buoyancy and inertial forces, in a containment environment. Notwithstanding the absence of the complications associated with condensation phenomena, the exercise still constituted a considerable

challenge to numerical analysts working in the field. As with the previous two benchmarks in the series, the measured data from the experiment remained closed until the numerical predictions had been collected, thus creating conditions for a ‘blind’ benchmark exercise.

For the purposes of the associated numerical simulations, the air/helium concentration, temperature and mean velocity profiles just above the nozzle exit were provided as boundary conditions. As described below, the velocity profiles at the exit of the inlet pipe were obtained from an ex-vessel experiment, for which the temperature was lower than in the actual test. Although this fact was declared openly in the specifications, some users obviously found some inconsistency between the given mass flow rate in the test and the value obtained by integrating the velocity profiles.

Subsequent events were monitored using a number of measuring instruments, including PIV, a mass spectrometer, and thermocouples, placed at strategic locations. The vessel was vented at the bottom to prevent pressurization. Participants were requested to supply transient data at selected locations for direct comparison against measured data taken over a two-hour period following initiation of the jet flow.

2. ORGANISATIONAL PROCEDURES

2.1 CSNI Approval

The offer of previously unreleased experimental data to act as a basis for the 3rd benchmark activity organised by the *CFD Bureau* was put before the WGAMA committee in September 2012. A CAPS[†] was prepared, and delivered to the members of WGAMA for consideration. The points put forward to support the proposal were:

- This was the third of the mandate items proposed by the original WGAMA Special CFD Group in 2007, and the other two items – the organisation of the CFD4NRS workshops and the setting up of a web-based portal for information relating to the use of CFD in NRS – were already approved and ongoing.
- Two very successful CFD benchmark activities, one based on the T-junction experiment performed at Vattenfall R&D, and the second, based on the MATiS-H rod-bundle test loop at KAERI, had just concluded; the present benchmark would be organised along similar lines.
- The Special CFD Group, subsequently renamed the CFD Bureau, would undertake the synthesis of the numerical results, including the comparison with measured data, and report its findings at the next scheduled Workshop in the series, CFD4NRS-5, already approved by WGAMA, to be held in September 2014 at the Swiss Federal Technical University (ETH), Zurich.
- The exercise would complement ongoing containment studies, but for which the test data are restricted.
- The 3-D nature of the gaseous flows generated in containments invites the use of CFD (or CFD-type) approaches, but such applications are presently hindered by the lack of adequate validation data of the basic physical phenomena at the appropriate scale. The proposed benchmark activity would provide invaluable data in this regard.
- Because of the recent accident at the Fukushima Daiichi plant, there is increased interest in containment modelling studies worldwide. It is anticipated therefore that many organisations would be interested in assessing their analytical skills in the framework of such an internationally sponsored programme.
- The activity fulfils increased public expectation of safety in the use of nuclear energy by creating a transparent technical basis for safety assessment by the application of new best-estimate numerical tools in NRS.

After some discussion, the CAPS was approved by WGAMA, passed on to the Project Review Group (PRG) for assessment, and finally endorsed by the CSNI in December 2012. Following these milestones in preparation, work on organising the benchmark activity began early in 2013.

[†] *CSNI Activity Proposal Sheet*

2.2 The Work of the Benchmark Organising Committee

The organising committee was formed from the current members of the *CFD Bureau* at the time, together with the member of the PSI team who would perform the synthesis of results (M. Andreani). Table 2.1 lists the members of the committee, their affiliations, and their principal functions within the scope of this benchmark exercise.

Table 2.1: Members of the OECD/NEA–PSI containment CFD benchmark organising committee.

Brian L. Smith	PSI, Switzerland	Chairman
Michele Andreani [†]	PSI, Switzerland	To perform synthesis of results
Dominique Bestion	CEA, France	Expert, and special advisor on workshop organisation
Ghani Zigh	US NRC, USA	Expert on modelling containment fires
Martin Kissane	OECD/NEA, France	Technical secretary

[†] Replacing D. Paladino (PSI) on the original committee list.

A date was fixed for a kick-off meeting of the benchmark exercise (25 April, 2013), and the technical secretary made the arrangements for this to take place at the NEA Headquarters in Paris. An announcement was prepared (reproduced in Annex 1) and sent out to more than 750 prospective participants on March 7, 2013 with an invitation to (i) attend the kick-off meeting; and/or (ii) register as a participant in the benchmarking exercise. In total, 49 registrations were made from organisations from 17 countries. Table 2.2 lists the countries specifically, and the number of registrations per country. As a consequence of their declared interest, all registered participants subsequently received the official benchmark specifications. The kick-off meeting was attended by 26 delegates, from 11 countries, plus 8 observers.

Table 2.2: Registrations to the OECD/NEA–PSI containment CFD benchmark.

China [†]	1	Italy	6	Spain	3
Finland	1	Japan	3	Sweden	1
France	10	S. Korea	1	Switzerland	4
Germany	3	Romania	1	UK	2
Greece	1	Russia	7	USA	3
Hungary	1	Slovenia	1		

[†] By special permission, China not having the status of being an official member of the OECD.

To set the scene at the kick-off meeting, D. Paladino from PSI, head of the PANDA experimental team, gave an outline of the PANDA test facility, and the specific details of the benchmark test, which had recently been carried out. He also provided details of the data to be given to participants (test geometry, initial conditions, etc.), and those requested from them in terms of numerical predictions. In addition, B. L. Smith (on behalf of M. Andreani) outlined the procedures for handling the numerical data files, the setting up of the special ftp site at PSI, and first thoughts on the strategy to be followed in performing an effective synthesis of the results.

The final timetable for the benchmark activity is given in Table 2.3. A draft version of the benchmark specifications was circulated to all registered participants on May 31, 2013, giving the details of the

geometrical set-up, and the range of flow parameters to be considered (though actual values had not yet been finalized). This preliminary information was provided to enable participants to begin their mesh construction. An invitation was extended for feedback concerning errors, clarity, ambiguity and possible misunderstandings in the wording of the specifications. A number of comments were received, and answered appropriately by the organisers via email correspondence. This led to some minor modifications being made to the benchmark specifications, to give greater clarity.

Complete specifications (including now precise details of all flow parameters) were re-issued on July 31, 2013, with again an invitation for comments. This was followed by the issue of the *Final Benchmark Specifications* document on August 28, 2013. This gave participants around nine months to complete their calculations, and to submit their numerical results by the deadline date of May 30, 2014.

Table 2.3: Timetable for the OECD/NEA–PSI CFD containment benchmark.

April 25, 2013	Kick-Off Meeting
May 31, 2013	Distribution of a provisional version of the Benchmark Specifications (geometry plus range of flow parameters)
July 31, 2013	Distribution of draft version of the Benchmark Specifications (geometry plus precise flow parameters)
August 15, 2013	Deadline for comment/queries from participants concerning the Benchmark Specifications to be returned to the organisers
August 28, 2013	Distribution of the final version of the Benchmark Specifications
May 30, 2014	Deadline (NOT EXTENDED!) for receipt of simulation results
June 4, 2014	Open Benchmark Meeting (first opening of the test data)
Sept. 10, 2014	Presentation of results, and synthesis, at the CFD4NRS-5 Workshop

The deadline for submission had to be rigidly enforced, because of the imminent release of the test data at the Open Benchmark Meeting just a few days later. Participants were encouraged to upload their data files to the PSI ftp site in good time, for there would be little opportunity to repeat the upload if there were any file-transfer communication problems. A special Python [24] script was prepared at PSI, and circulated in advance, so that participants could test whether their simulation data were strictly in accordance with the formatting instructions given in the benchmark specifications. This precaution was necessary to fully automate the processing of the data files, and to save unnecessary effort in correcting them.

Reminders that the deadline for submission was approaching were sent to all registered participants in the days leading up to the deadline date for submission. Participants were also reminded that following the opening of the test data on June 4, 2014, they would not be permitted to exchange or withdraw their submitted numerical results, which would then automatically become part of the official benchmark synthesis. In return for their participation, they would receive the test data from the benchmark experiment in full.

The PSI ftp site was managed by M. Andreani, in collaboration with the PSI Information Technology (IT) department. Provision was made for up to 60 user accounts, all of them password protected. Registered participants were requested to ask for an account: (i) if they wished to download the benchmark specifications directly, including the design drawings and CAD files, and (ii) to gain the privileges necessary to subsequently upload the data files containing their numerical predictions. Apart from a number

of users with observer status on the site, of the 49 who originally registered interest in participating in the benchmark activity, 29 officially requested a username and password on the ftp site.

Also, it was made clear from the outset (i.e. at the *Kick-Off Meeting*) that only one set of blind numerical predictions would be accepted by the organisers from each participant. The registration procedure set up on the ftp site effectively precluded the opportunity for multiple uploads anyway. In cases of multiple uploads from the same organization, though with different user names, these would be scrutinized carefully for complicity. The organisers wanted each participant to submit what he/she considered to be their “best” numerical predictions. What was to be avoided was that a particular group was not sure which mesh to employ, or which turbulence model to use, and would make multiple registrations to bypass the one-participant/one-simulation principle on which this benchmark exercise was based. Fortunately, no examples of such complicity were detected.

Overall, communication between participants and organisers (via email) went well, as did the uploading, and exchanging, of the numerical data files. Each participant was given the option to exchange the files submitted for updated ones at any time up to the deadline date, but then access to the *Dropbox* on the ftp site was blocked, and no further exchanges, or withdrawals, were then be permitted.

In total (after removing one or two incomplete data sets), 19 submissions were received by the deadline, and these form the basis of the synthesis procedure subsequently carried out by M. Andreani (PSI) and A. Badillo (PSI), and reported at the CFD4NRS-5 Workshop. In addition, a special Poster Session was organised at the workshop, where participants could display their results without the need to write an accompanying paper. There were 10 participants who took advantage of this offer. Any subsequent post-test simulations they had performed since release of the test data could also be shown at this time, at their discretion.

After opening of the test data for the first time on June 4, all the 19 participants were entitled to receive the test data in full. A mutual confidentiality agreement was drawn up to protect the proprietary rights of both the measured and numerical data sets. One participant had internal problems with his parent organization concerning this agreement, but the remaining 18 participants did sign, and subsequently received the test data, as promised.

3. EXPERIMENTAL FACILITY

3.1 General Layout

A full description of the experimental rig was included as part of the official Benchmark Specifications; for completeness, these are reproduced in full in Annex 2 here. In addition, a paper [25] was presented at the CFD4NRS-5 Workshop detailing the experimental part of the benchmark exercise. Again for completeness of this document, the salient points are presented in this Section.

The benchmark experiment was performed in one of the PANDA drywell vessels, of inner diameter 4 m and height 8 m, as shown in Fig. 3.1. The air-helium mixture forming the jet, of density ρ_j and nominal tube exit velocity $v_{j,n}$, is injected through a pipe positioned off-axis by 648 mm with respect to the axis of symmetry of the vessel. For the calculation of the nominal velocity, the formation of boundary layers at the inner tube walls was neglected, and a constant velocity across the (horizontal) tube exit plane was assumed. The injection tube has a 180° bend 2200 mm below the tube exit (see Fig. 3.1). The straight tube past the bend has a length of some 30 hydraulic diameters, which is considered long enough (for the tube exit Reynolds number of 20 000) for possible disturbances introduced by the bend to have been removed by turbulence before the gas mixture is injected into the vessel. This assumption was confirmed by the tube exit velocity measurements taken, as described later. It was observed that the velocity profile at the tube exit displayed the expected top hat characteristics, with narrow boundary layers, typical of highly turbulent pipe flow.

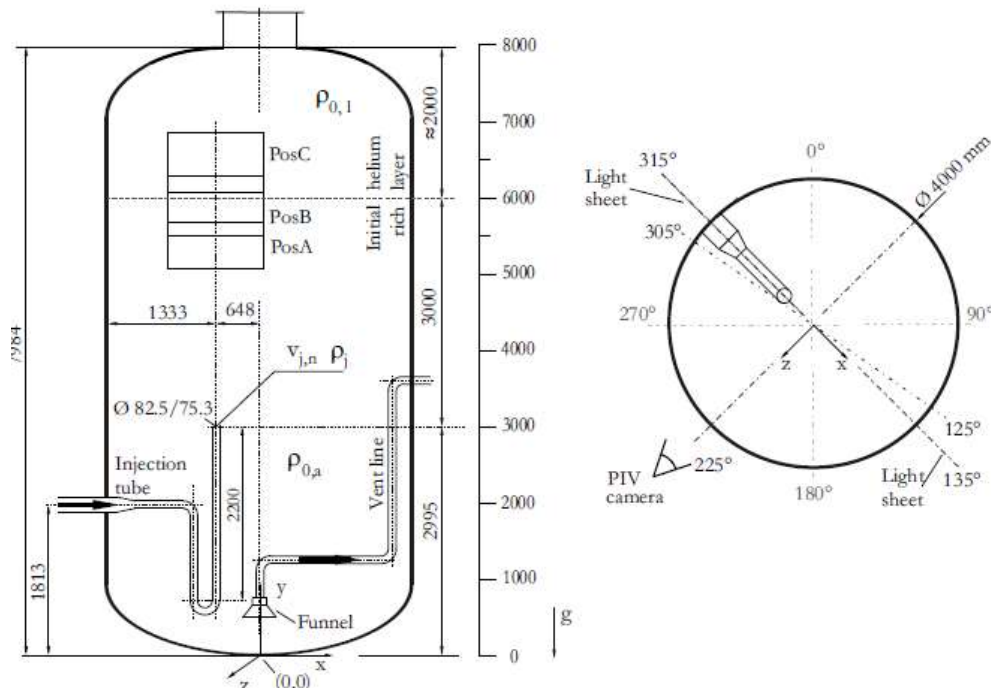


Fig 3.1: Schematic side and top views of the PANDA dry-well vessel: the helium-rich layer is located in the vessel dome; dimensions are given in mm.

In contrast to some past jet experiments in PANDA, in which a smooth contraction nozzle at the pipe exit was used to pronounce the top hat velocity profile by compressing the boundary layers, here an injection pipe of constant nominal inner diameter of $d_t = 75.3$ mm was employed. Testing for the circularity of the tube, the actual inner diameter measured at the pipe exit in two perpendicular directions was $d_{t,a} = 75.4$ mm and $d_{t,b} = 75.6$ mm, in good agreement with the nominal, constant value ($d_t = 75.3$ mm), which was used henceforth.

During the experiment, the pressure was kept constant at 0.994 bar absolute by venting the gases from the bottom of the vessel via a funnel (orientated downwards) connected to a flexible hose, see Fig. 3.1. The injection tube exit was located 2995 mm above the inside wall at the bottom of the vessel. The origin of the coordinate system adopted is also located at this internal bottom position of the vessel, as is the light sheet for the PIV recordings, coinciding with the x-y plane.

3.2 Instrumentation

For the 2D velocity measurements, a Particle Image Velocimetry (PIV) system was employed. The PIV camera was mounted in front of the upper vessel window on a translation stage consisting of two goniometers and a rotation table. By vertically inclining the camera, it was possible to record three different fields-of-view (FOVs) to follow the progression of the helium layer as it became eroded. The three FOVs are labelled PosA, PosB and PosC in Fig. 3.1.

An example of a raw PIV image recorded at PosB is shown in Fig. 3.2a. The image gives a visual impression of the jet-layer interaction zone. The (seeded) jet entering from below impinges on the (non-seeded) helium-rich layer, and penetrates the stratification interface. The corresponding instantaneous velocity field, with some selected stream lines, is given in Fig. 3.2b. Olive oil, dispersed into small droplets by a spray nozzle, provided the seeding particles for the PIV. These were injected into the jet stream directed into the vessel through the injection line. The PIV system setup for the in-vessel measurements provided 2D velocity fields with an acquisition frequency of 5 Hz. For the calculation of statistical quantities, 1024 image pairs were averaged, resulting in an overall averaging time of 204.8 s.

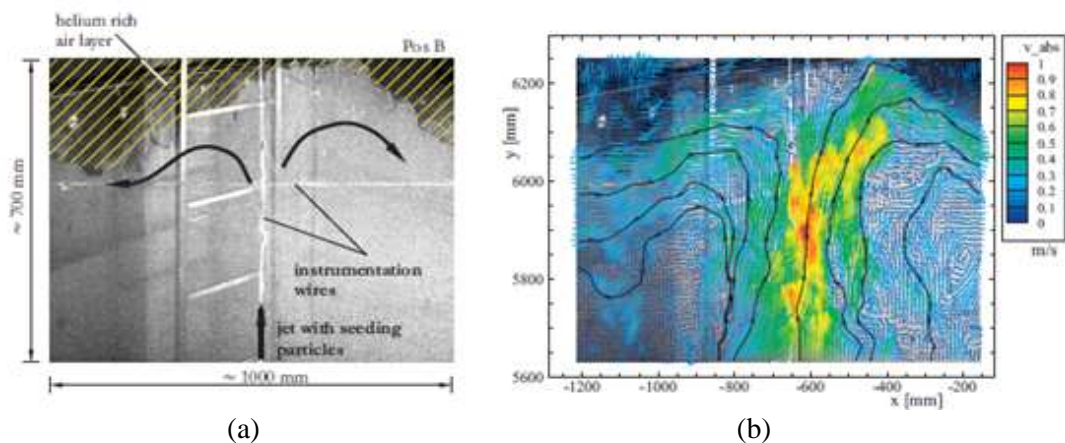


Fig. 3.2: A typical PIV raw image showing: (a) the seeded jet in the lower part, the non-seeded helium-rich layer at the top, and the instrumentation wires; and (b) the corresponding instantaneous velocity field and selected stream lines; dimensions are given in mm.

The PIV system consisted of a Quantel Twin B double-pulse laser, with maximum output energy of 380 mJ, and a double-frame CCD camera type Imager Pro X (identical to a PCO.1600 camera), with a resolution of 1600×1200 pixels. After calibration of the images, a resolution of 0.715×0.715 mm²/pixel was achieved, corresponding to an effective spatial resolution of 11.5×11.5 mm² for the velocity field. The absolute

statistical error for the mean velocity, with confidence band of $\pm 95\%$, was then estimated at $\varepsilon = \pm 0.014$ m/s, on average.

The gas concentration was measured in the facility by means of two (MS) mass spectrometers. Gas was continuously sampled, and sent to the MS systems through capillaries. Each of these lines was equipped with a thermocouple to record the temperature of the gas at the associated capillary inlet. The MS measurements were sequential, and only one line could be selected at any given time, this by means of a multi-port rotating valve. When selected, the sampled gas was sent to a quadrupole mass spectrometer, which then gave the partial pressure of the selected (air and helium) gas stream. From the respective partial pressures, and the temperature, the molar fractions and densities could then be calculated. The MS capillaries, as well as the thermocouples themselves, were mounted on instrumentation wires throughout the vessel. Both a horizontal and vertical instrumentation wire are visible in the PIV recording pictured in Fig. 3.2a. The measurement error of the MS system is estimated to be 1% absolute.

For the measurement of gas temperatures, Type-K thermocouples (TCs), each of diameter 1 mm were employed. Three of these, out of a total number of 266 used in this experiment, were specifically calibrated for the temperature range 40°C to 200°C by an external agency. Based on the deviations from the actual readings from the set value obtained, a common calibration curve to compensate for any offset was derived for these three TCs and then applied to the entire set. With the compensation of the offset applied, and from the calibration at the PTB, an error of $\varepsilon_{tc} = \pm 0.7\text{K}$, with a confidence band of $\pm 95\%$, was estimated for each of the temperature readings.

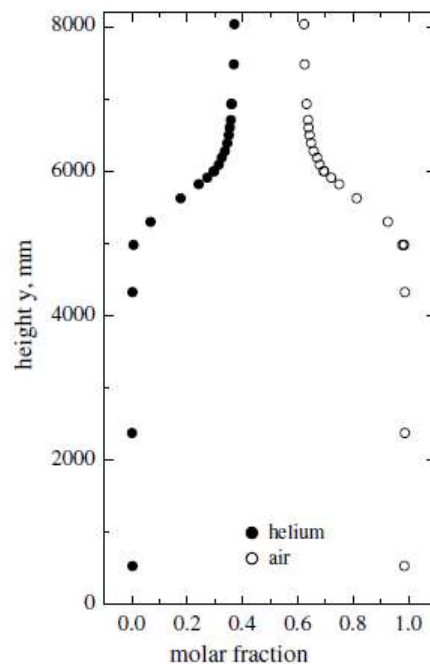


Fig. 3.3: Initial air and helium molar fraction as a function of height in the vessel.

3.3 Initial and boundary conditions

Prior to the test, stratified air/helium conditions were established in the test vessel. A helium-rich air layer of density $\rho_{0,l}$ occupied the region $y > 6000$ mm (Fig. 3.1), while pure air of density $\rho_{0,a}$ occupied the region $y < 5000$ mm. In the transition region between these levels, the helium content increased continuously upwards from close to zero to $\chi = 0.37$, as displayed in Fig. 3.3. Data have been compiled principally from measurements taken along the axis of the vessel, though off-axis measurements were also taken to demonstrate the flatness of the (initial) horizontal stratification. Exact details in tabular form are given in

Annex 2. These were sent to all registered participants. The deviation from the nominal values was estimated to be below 1%.

The air mass flow rate to the injection line was measured using a thermal mass flow meter to an accuracy of 1.5% of the measured value (according to the manual supplied with the instrument). The mass flow rate was averaged over 6588 s (3294 data points sampled at 0.5 Hz), giving a mean flow rate of 21.53 g/s, with a standard deviation of 0.23 g/s. The total mass flow rate was held constant throughout the test.

The mass flow rate of helium was also measured with a thermal mass flow meter of the same type, and the sampling frequency and sampling time were the same. However, the helium mass flow meter had been calibrated by the manufacturer using air. Since the conversion from the air calibration to a helium mass flow rate involved some uncertainties, it was decided to use a number of conversion methodologies, and to assess their deviation from each other:

1. The manufacturer's calibration method was used, together with the supplied software for the air to helium conversion;
2. The manufacturer's calibration method was used, combined with the ratio of the specific heats for air and helium;
3. The actual flow meter measurement was compared with that calculated to increase the pressure in the PANDA vessel by a specified amount;
4. The available MassSpec data were used to calculate the helium mass flow in the injected air-helium mixture, while the air flow rate was measured with a standard thermal mass flow meter.

Subsequently, the mass flow meter was sent to an independent calibration laboratory. After this:

5. The revised calibration coefficients were used;
6. The revised calibration coefficients were used in combination with the specific heat ratio of helium and air.

Combining all six methods, and using standard statistical assessment methods, it was estimated that the mean helium mass flow rate in the jet was 0.42 g/s, with an error of 0.022 g/s, at a confidence level of 99%.

The jet Reynolds number $Re_{j,b}$ at the tube exit:

$$Re_{j,b} = \frac{v_{j,b} d_t}{\nu_j}, \quad (1)$$

was calculated using the nominal inner diameter of the tube ($d_t = 75.3$ mm), and the bulk velocity $v_{j,b}$. Since the flow rate was kept constant throughout the experiment, this Reynolds number completely characterizes the momentum flux of the jet.

To characterize the initial buoyancy, the source densimetric Froude number is employed:

$$Fr_0 = \frac{v_{j,b}}{\left[(\rho_{0,a} - \rho_j) / \rho_{0,a} g d_t \right]^{1/2}}, \quad (2)$$

Inserting appropriate values gives $Fr_0 = 15.6$, which indicates a 'jet-like', momentum-dominated, flow at the exit of the injection tube, at least initially.

To characterize the initial stratification strength, and the buoyancy conditions, two (initial) density differences are defined: that between the jet and the ambient surroundings:

$$\Delta\rho_{0,ja} = (\rho_{0,a} - \rho_j) / \rho_{0,a} \times 100, \quad (3)$$

and that between the helium-rich layer and the jet:

$$\Delta\rho_{0,jl} = (\rho_{0,l} - \rho_j) / \rho_{0,l} \times 100. \quad (4)$$

Initially ($t = 0$), just above the tube exit, the upward jet experiences a positive buoyancy force, with $\Delta\rho_{0,ja} \approx +11\%$, so the momentum decay along the axis of the jet due to its spreading will be partly compensated by this effect; or there may even be a mild acceleration. As the jet approaches the helium rich layer, the ‘ambient’ density progressively decreases (Fig. 3.3), and the jet becomes increasingly negatively buoyant ($\Delta\rho_{0,ja} \approx -36\%$), as it penetrates the helium-rich layer, whereupon the axial momentum would decay very rapidly with height. Note that this latter estimate neglects the entrainment of ambient gas into the jet on its way from the tube orifice to the helium-rich layer, and the associated density increase, but does at least provide a limiting case. However, the point being made here is that both density difference estimates indicate the inadequacy of the Boussinesq approximation to represent the buoyancy effect, and it is hoped that this is properly taken into account in the numerical simulations.

3.4 Inlet tube exit velocities

PIV measurements of the instantaneous values of the Cartesian horizontal and vertical velocity components (u,v) of the gas mixture emerging from the injection pipe outlet were made in a stand-alone test with the injection line removed from the PANDA vessel, though still connected to the same helium and air supply lines used in the actual test; this for better access to the measuring equipment. Measurements were taken in five horizontal planes over the internal pipe cross-section, each positioned 6 mm above the injection pipe outlet. From the horizontal measurement planes, velocity profiles were extracted at $y = 7.3$ mm above the outlet; a position corresponding the closest approach to $y/d_t = 0.1$. A schematic of the experimental arrangement is shown in Fig. 3.4. The gas mixture in this stand-alone test was not pre-heated, the ambient temperature being estimated at 15°C , though this should have negligible influence on the velocity profile, given the proximity of the measurement plane to the pipe exit, and the magnitude of the jet Froude number ($Fr_j = 15.6$).

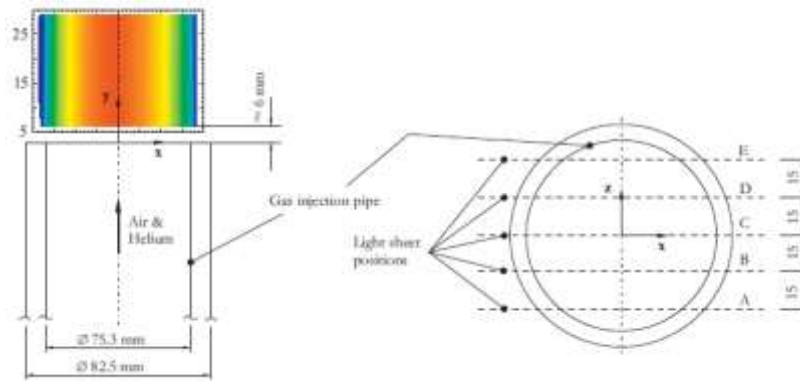


Fig. 3.4: Relative positions of the FOVs of the PIV velocity measurements at the exit of the injection line; note the local coordinate system used for the measurement planes A-E which differs from the one given in Fig. 3.1.

The tube exit measurements provided 2D velocity fields at an acquisition rate of 7.5 Hz. For the calculation of statistical quantities, 4096 image pairs were averaged. The PIV system was the same as that used for the in-vessel measurements, consisting of a Litron nano L double pulse laser with maximum output energy of 200 mJ; the light sheet thickness was approximately 1 mm. The optical recording system consisted of the camera and a Nikon lens (AF Nikkor, $f = 50$ mm), the aperture being set to $f_{\#} = 4$. The base analysis was performed with DaVis 8.1, and the extended analysis with in-house routines written in MATLAB software. After calibration of the images, a resolution of 0.088×0.088 mm²/pixel was obtained, and this corresponds to an effective spatial resolution of 0.53×0.53 mm² for the velocity field. The measured velocity mean and rms profiles for the two components are shown in Fig. 3.5, and the turbulence statistics in Fig. 3.6. These data were extracted at a distance $y/d_t = 0.097$ above the tube exit. Due to technical restrictions, and time

constraints, it was not possible to measure the third velocity component w ; that is the component in the z direction of Fig. 3.4. However, the assumption of axi-symmetric outlet conditions is expected to prevail in this test, so this measurement is probably superfluous anyway.

The radial (i.e. in the x -direction) distances are normalized with respect to the nominal pipe diameter $d_t = 75.3$ mm, and the velocities are normalized with respect to the axial velocity $v_c = 5.35$ m/s along the centre line ($x = z = 0$). The procedure adopted for calculating the mean velocity components, and time-averaged standard deviations, from the instantaneous velocity data collected was as follows:

$$\bar{u} = \frac{1}{N} \sum_{i=1}^N u_i, \quad (5)$$

$$u' = \sqrt{\frac{1}{N} \sum_{i=1}^N (u_i - \bar{u})^2}, \quad (6)$$

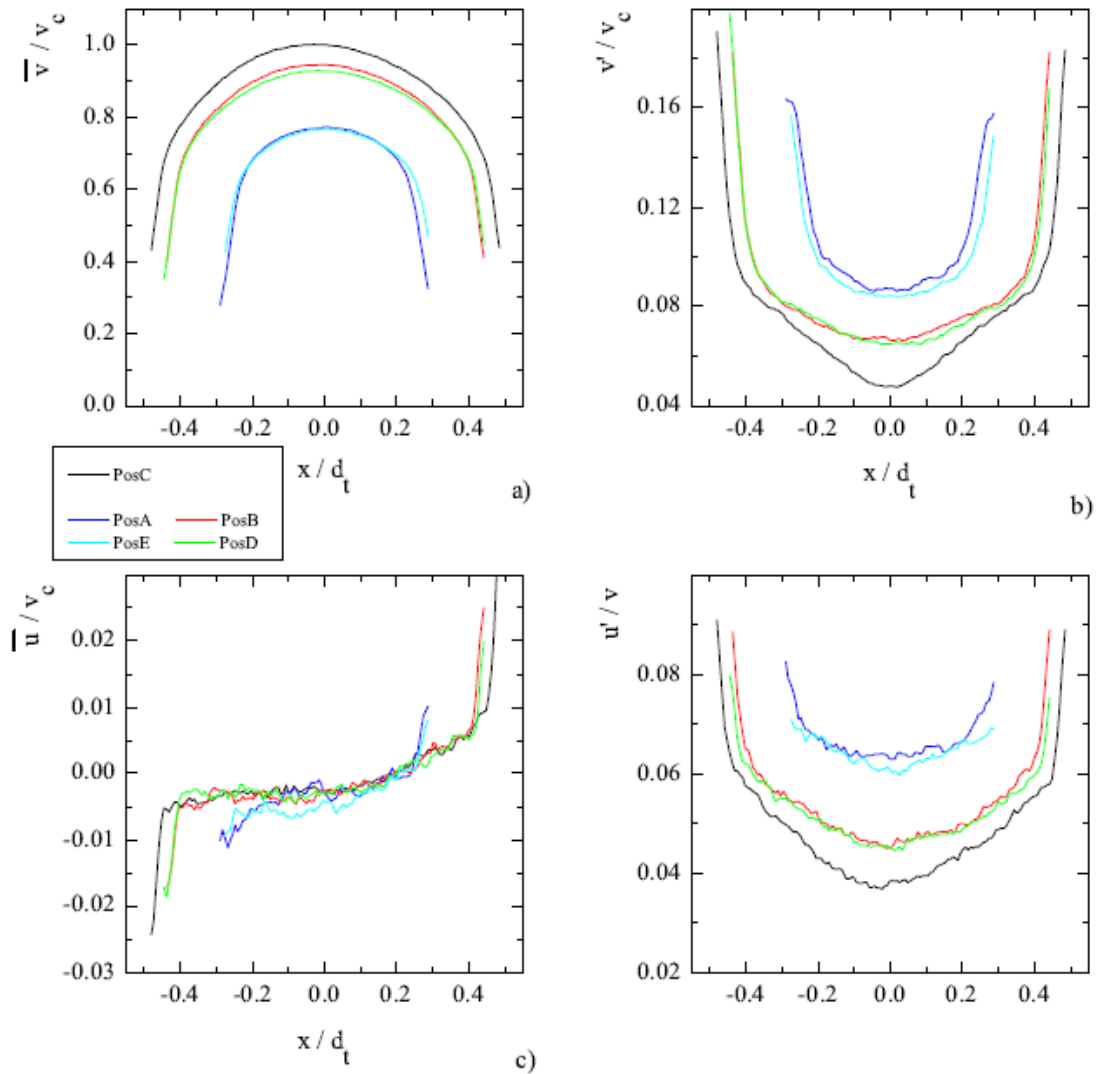


Fig. 3.5: Normalized mean axial and lateral velocity profiles (plots a and c) and the corresponding fluctuating quantities (plots b and d) for the measurement lines A-E (Fig. 3.4) at $y/d_t = 0.097$: i.e. just above the injection pipe exit.

Additionally, the normal and shear Reynolds stresses, and the turbulent kinetic energy, is calculated according to:

$$\overline{u'u'} = \frac{1}{N} \sum_{i=1}^N (u_i - \bar{u})^2, \quad \overline{v'v'} = \frac{1}{N} \sum_{i=1}^N (v_i - \bar{v})^2 \quad (7)$$

$$\overline{u'v'} = \frac{1}{N} \sum_{i=1}^N (u_i - \bar{u})(v_i - \bar{v}), \quad (8)$$

$$k = \frac{1}{2} \{2(\overline{u'u'}) + \overline{v'v'}\}, \quad (9)$$

Here, N is the number of instantaneous velocity recordings used in forming the average: these were taken from 4096 statistically independent samples, obtained at a sampling frequency of 7.5 Hz, which corresponds to an overall averaging time of 546 s (9.1 min.). To calculate k using Eq. (9), the assumption of axial symmetry has been employed, the third velocity component w not having been measured directly. For the normalized axial mean velocity profiles $\bar{v}(x/d_t) = v_c$ (Fig. 3.5a), measured in five planes, good agreement was obtained between planes A and E, and between B and D, equally displaced by 30 mm and 15 mm, respectively, from the plane through the centre C, confirming the assumption of an axi-symmetric profile across the entire tube exit, as assumed in Eq. (9). This holds true also for the other turbulence statistics. It should be noted that, in the core region of the jet ($-0.1 < x/d_t < 0.1$), a non-zero value for the mean lateral velocity component u has been recorded for all the measurement planes (Fig. 3.5c). This is considered a consequence of the slightly rotated camera angle with respect to the jet axis, resulting in a ‘virtual redistribution’ of the vertical velocity in the lateral velocity direction, which of course should be zero in the core of the jet. If the central measurement plane C is regarded as representative ($u = 0.013$ m/s, $v = 5.35$ m/s), this would indicate a camera inclination of 0.14° . Removing this bias, the ‘true’ axial velocity would then be 5.35001 m/s instead of the 5.35 m/s adopted, an entirely negligible error. The measured profiles were further examined by comparing them against appropriate data from the literature. In all cases, the accuracy of the profiles was completely vindicated, and certainly more than adequate for the purposes of this benchmark exercise. Full details are given in [25].

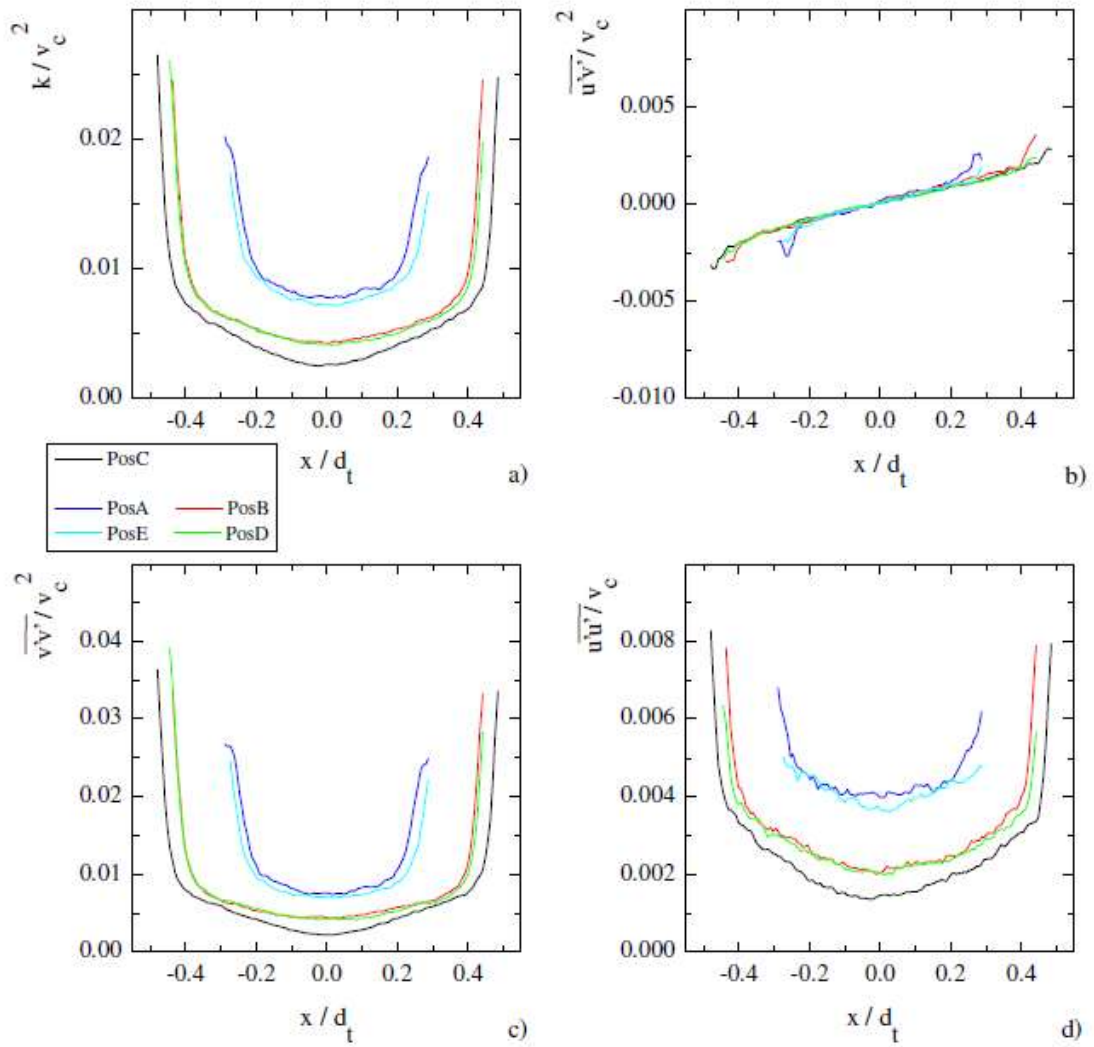


Fig. 3.6: Turbulence quantities at $y/d_t = 0.097$ above the injection pipe exit: (a) normalized turbulent kinetic energy k (Eq. 10); and the normal and shear Reynolds stresses (Eqs. 8, 9) for each of the measurement planes A-E (Fig. 3.4).

3.5 In-vessel measurements

To establish the initial stratification conditions in the vessel, helium was injected through a pipe situated 2 m below the top of the vessel dome. The time to achieve a uniform helium concentration of 0.37 molar fraction in the region above the injection level was established through scoping tests. The initial density profile for this benchmark experiment, measured at $y = -648$ mm off-axis (Fig. 3.1), is shown in Fig. 3.7. In the lower part of the vessel we have initially an air atmosphere at room temperature ($T = 22^\circ\text{C}$, $p = 0.994$ bar), while the helium-air mixture, with the lower density, is trapped in the vessel dome, creating the initial stratification.

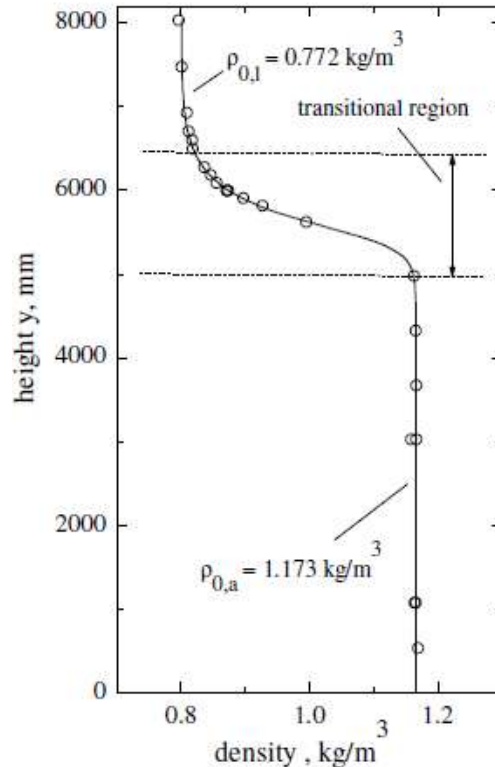


Fig. 3.7: Initial gas density ($t_0 = 0$) as a function of height in the vessel.

The transient is initiated by opening a valve to release the air-helium gas mixture to the injection line ($t_0 = 0$), and is deemed to have finished when the helium-rich layer has been completely eroded; i.e. when the mixture density has equalized in the entire vessel ($t \approx 5300$ s). Mean velocities and velocity fluctuations were measured using PIV in the three window regions PosA, PosB, PosC shown in Fig. 3.1, all above and around the axis of the injection pipe. These raw measurements were processed to produce averaged values (over time intervals of 204.8 s) throughout the entire transient. The measured data appearing below refer to the central time t_c of this averaging period; i.e. at $\Delta t = \pm 102.4$ s around each data item.

An overview of the PIV recordings obtained during the experiment is given in Table 3.1. Mean velocity ($|\bar{v}| = \sqrt{u^2 + v^2}$) maps, together with the corresponding turbulent kinetic energy k (Eq. 9) maps, measured in the air/helium jet as it impinges onto the helium-rich air layer from below, are presented in Fig. 3.8 at the selected times given in Table 3.1. The time steps cover the instances from the beginning of the injection (Fig. 3.8a), later, when the erosion process has advanced (Figs. 3.8b, 3.8c), and finally at the time the erosion zone is on the point of leaving the FOV entirely, i.e. above the level $y = 6900$ mm (Fig. 3.8d). Streamlines have been calculated from the underlying velocity field to guide the eye. These streamlines are

identical for the corresponding $|\bar{v}|$ and k maps. The axis of the injection line (at $x = -648$ mm) is indicated by the dashed line. Since the seeding particles for the PIV measurements are transported with the jet, the helium layer unaffected by the jet remains non-seeded, so no velocity data are available in these (small) regions. This feature becomes particularly visible for the k maps in the top parts of Figs 3.8g and 3.8h, where, artificially, a value $k = 0$ is recorded. Additionally, to assess the quality of the data, the statistical quantities have been thresholded, calculated on a minimum of 900 valid vectors. This results in the abrupt changes in the quantities in areas with a lower number of valid vectors. One finds also minor horizontally and vertically oriented distortion zones caused by the instrumentation wires used for the temperature and mass spectrometer measurements (Fig. 3.2). These areas were masked during the analysis, and the resulting gaps were filled using linear interpolation from nearby values to facilitate the calculation of streamlines.

Table 3.1: Labels of the PIV measurements performed (N01 to N08), FOV (A to C), and central sampling time t_c .

Number	Position	t_c (s)		Number	Position	t_c (s)
N01	A	111		N05	C	1795
N02	B	715		N06	C	2030
N03	B	978		N07	C	2286
N04	B	1213		N08	C	2550

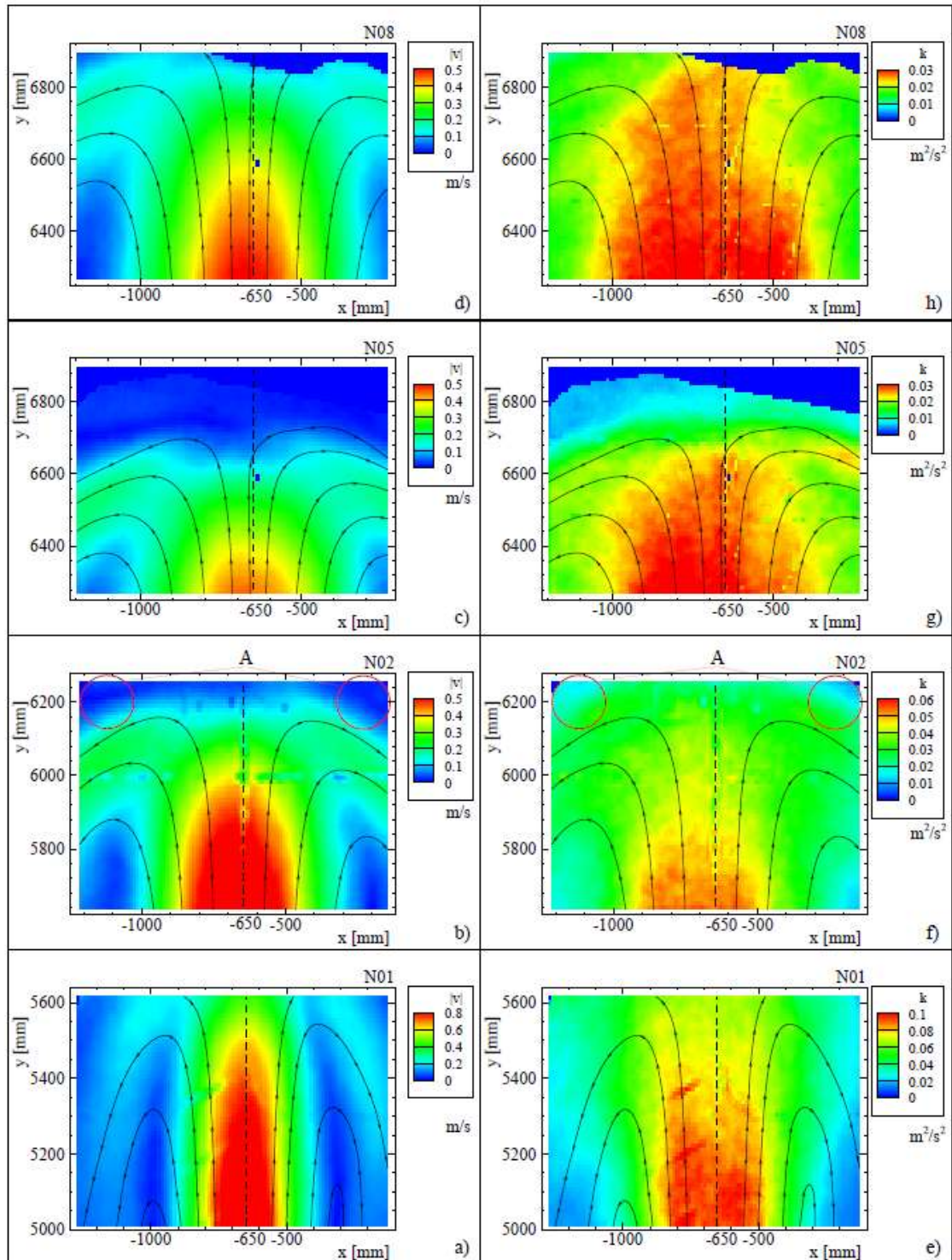


Fig. 3.8: Selected velocity magnitude maps $|v|$ (a to d) and the corresponding turbulent kinetic energy k maps (e to h) recorded during the erosion process of the helium-rich layer.

As a consequence of its momentum, the jet penetrates deeply into the helium rich layer, but is strongly decelerated by the negative buoyancy (Figs. 3.8b, 3.8c), and is finally arrested completely. Fluid

accumulates in a continuous process in this mixing zone and part of it flows back via a narrow annular region surrounding the upward moving jet, as depicted by the streamlines (Fig. 3.8a). The jet decelerates additionally as a consequence of the shear created by this downward annular flow against the upward jet motion, part of the annular flow being re-entrained into the rising jet. The main difference between the early stage of the erosion process (N01) and at later times (N02, N05, N08) is the stronger confinement of the flow around the jet (Fig. 3.8a versus 3.8b). This difference may be attributed to three effects: (i) the spreading of the jet due to entrainment of ambient fluid; (ii) the increasing resistance the helium rich layer imparts to the jet propagation; and (iii) the continuous entrainment and downwards transport of the helium-rich layer, which progressively decreases the ‘ambient’ mixture density.

Initially (N01), the jet impacts the transition region of the stratification (Fig. 3.7), where the density decreases from 1.166 to 0.80 kg/m³ over a distance of 1 m. The negative buoyancy initially imposed by the layer on the jet is weaker than at later times, progressively as the transition region is eroded (N02 → N05 → N08); see also [26]. Also, initially (N01), the jet at the tube exit experiences a positive buoyancy due to the density difference between it and the air around it $\Delta\rho_{0,ja} \approx 11\%$, which provides additional impetus. This positive buoyancy effect decreases over time through the downwards progression of the helium-rich layer.

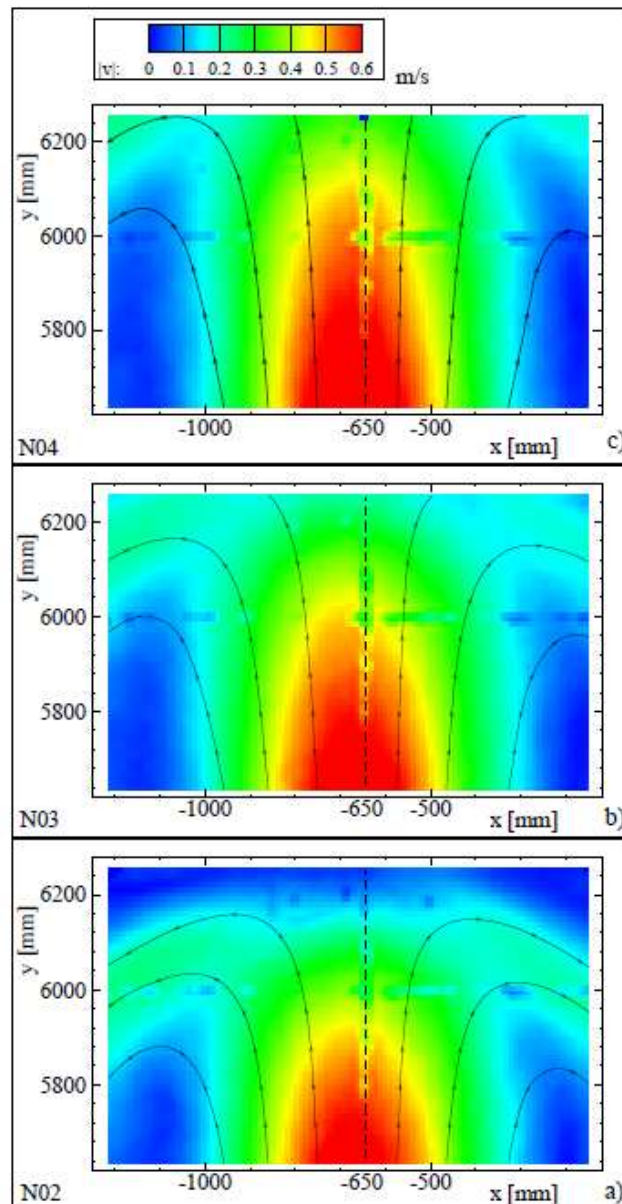


Fig. 3.9: Development of the velocity magnitude field for position B (Table 3.1) at times $t = 715, 978, 1213$ s.

During the erosion process, the secondary flow structure changes from a more downwards oriented annular type to a more horizontally oriented mushroom type of flow (Fig. 3.8, N02 to N08), as indicated by the streamlines. This erosion process is shown from another perspective for the velocity field recorded at the fixed position B (Fig. 3.9) at three different times. The erosion front moves progressively upwards (N02 \rightarrow N03 \rightarrow N04) with increasing time, the radii of curvature of the streamlines increase, until finally the mixing zone is above the field of view altogether (N04). The observations for the velocity magnitude field apply also to the turbulent kinetic energy maps (Fig. 3.8e versus 3.8g). Initially, $k \approx 0.1 \text{ m}^2/\text{s}^2$ in the core of the jet (N01), but is later distributed over a wider region, and reduces to $k \approx 0.03 \text{ m}^2/\text{s}^2$ (N08).

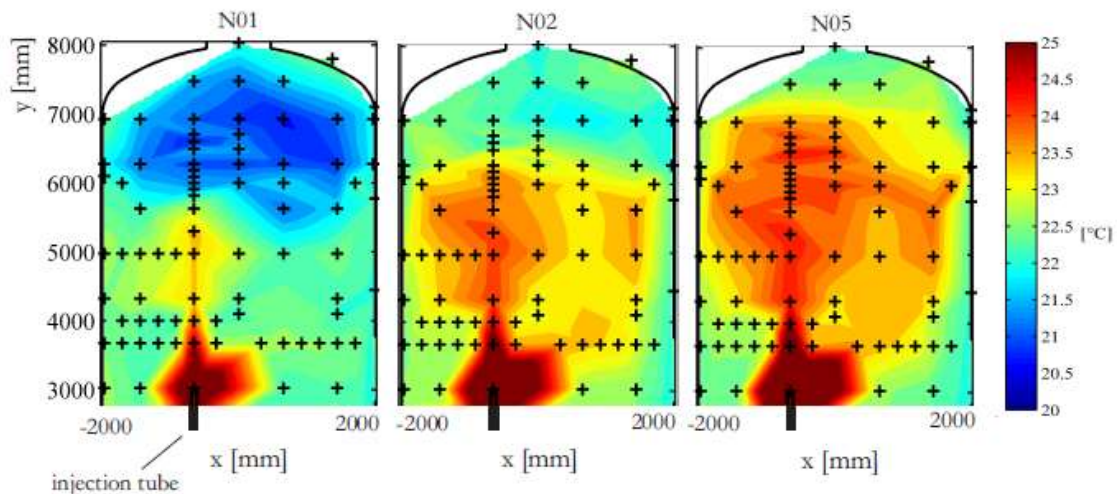


Fig. 3.10: Temperature contour maps for the entire vessel.

The three temperature contour maps presented in Fig. 3.10 correspond to the PIV measurements in Fig. 3.8 for times N01, N02 and N05 (Table 3.1), and have also been averaged over the same interval, $\Delta t = 204.8$ s. The contours were calculated by linearly interpolating the temperatures recorded at the thermocouple measurement locations depicted by the black crosses. The jet flow was injected with a slightly elevated temperature compared to elsewhere in the vessel specifically so that these contours could be drawn. It should be noted that the density difference between jet and ambient resulting from $\Delta T = 5$ K is very small compared with that due to the helium content in the jet (11% initially). For N01 (left image in Fig. 3.10), immediately following jet initiation, the somewhat cooler ($T \approx 20^\circ\text{C}$) helium rich layer in the vessel dome (resulting from the helium injection process) is clearly visible. Subsequently, the off-axis positioning of the injection line results in a left-right asymmetry in the global temperature maps, which persists over the entire transient.

The helium molar fraction χ_{he} along the jet axis ($x = -648$ mm) as a function of time for some selected vertical locations are presented in Fig. 3.11. Additionally, the molar fraction of helium measured at the tube exit in the jet is provided with the measurement at the location $y = 3000$ mm. Initially, the helium content of the jet decreases from $\chi_{\text{he}} \approx 0.13$ at the tube exit to $\chi_{\text{he}} \approx 0.05$ at position $y = 4326$ mm, still somewhat below the helium-rich transition layer ($y > 5000$ mm) through the entrainment of ambient gas from the surroundings, which consist of almost pure air at this early stage of the transient. As a result of the continuous erosion of the helium-rich layer at the top of the vessel, and the downwards transport of helium, the helium content of the ambient increases such that χ_{he} in the jet at this same position, $y = 4326$ mm, increases progressively over time.

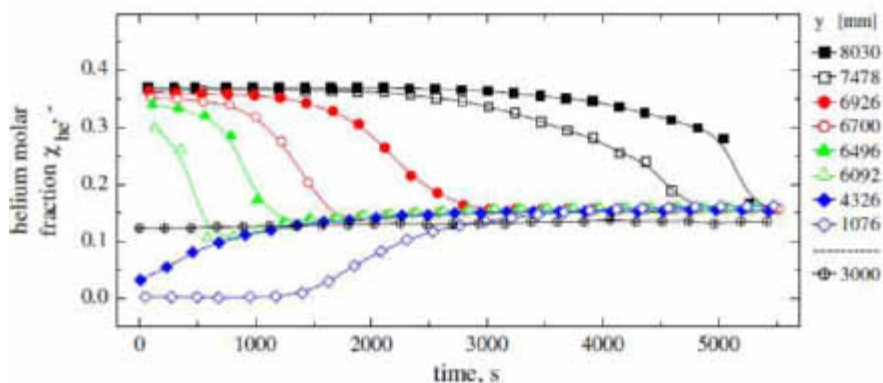


Fig. 3.11: Helium molar fraction at selected locations along the jet axis ($x = -648$ mm) as a function of time with the vertical measurement location as parameter.

The molar fraction at the tube exit is provided at $y = 3000$ mm.

At the initial stage of the erosion process, it is expected that the secondary flow described previously does not descend all the way down to the level of the jet orifice — and eventually down to the base of the vessel — but only down to an intermediate level where the density of the mixture of the annular flow matches that of its surroundings, causing the fluid to spread out radially; this behaviour had been noted before in similar experiments [27,26]. Consequently, the measurement location at the bottom of the vessel ($y = 1076$ mm) indicates no helium transport into this region until $t \approx 1500$ s. The helium content measured at those points initially located in the helium-rich layer ($y \geq 6000$ mm) decreases with time, those at lower elevations faster than the ones above. The helium content at all positions ultimately approaches a common level of $\chi_{\text{he}} \approx 0.15$, a state for which the gas in the entire vessel may be considered homogeneously mixed.

3.6 Summary of experimental findings

To provide an experimental basis for this benchmark exercise, a comprehensively instrumented containment experiment was carried out in one of the drywell vessels of the large-scale PANDA facility at the Paul Scherrer Institute. The experimental details necessary to enable participants in the benchmark to perform their ‘blind’ simulations are given in their entirety in Annex 2 of this document. The collection of the measured data by which the numerical predictions have been assessed has been outlined in this section. Exact measured profiles at the positions at which the ‘blind’ numerical predictions had been requested were supplied to those participants who had submitted their data by the deadline date.

At the exit of the injection line, flow parameters were chosen that resulted in an initial Reynolds number $Re_0 = 20'000$, hence fully turbulent jet inlet conditions. The Froude number $Fr_0 = 13.6$ at the pipe exit indicates a momentum-dominated flow in this region, at least initially. The flow parameters were such that the Froude number for the jet/interface interaction was $Fr_{j,I} \approx 1$, this being the most challenging case for the CFD practitioners from previous PANDA experiments of a similar type in the context of the SETH-2 project [28].

For the tube-exit measurements, taken during an ex-vessel test, using a two-component PIV system, excellent agreement has been found for the mean axial velocity profile with those reported in the literature for different pipe-flow configurations. Fluctuating velocities were also derived from the instantaneous velocity measurements taken, as well as the normal and shear Reynolds stresses. These data were supplied to all registered participants.

The experiment was conducted at room temperature, though the jet was mildly heated with respect to the initial gas mixture in the vessel in order to produce temperature maps. However, most of the buoyancy of the jet was provided by adding helium at a specified concentration.

From the PIV measurements in the the jet/interface interaction region, via three windows into the vessel, and augmented by mass spectroscopy measurements of helium concentration at strategic locations, and by the matrix of thermocouples, a comprehensive pictorial image of the evolving flow field could be constructed, which depicted clearly the evolution of the flow taking place.

The vertical jet initially is positively buoyant with respect to its surroundings, but becomes increasingly negatively buoyant as it penetrates the helium-rich stratification layer above, and then the axial velocity of the jet decays very rapidly with height. The PIV measurements taken clearly reflect this process. Fluid accumulates in the mixing zone, and returns via a narrow annulus around the upward-directed jet flow, generating shear forces. By this transient mechanism, the helium-rich layer is continuously eroded, and helium is transported to the lower parts of the vessel. The jet’s positive buoyancy at the tube exit decays over time, until eventually all the gas mixture in the vessel has become homogenized.

The visual description of the entire time-dependent erosion process was captured by the different instrumentation employed, the data combining in a consistent manner. In addition, very precise local data have been collected at precise locations, and a selection of these was assembled to form the basis of the quantitative data by which the numerical benchmark predictions were to be assessed. Both mean and

(averaged) root-mean-square data were made available, together with standard deviations regarding measurement error. Detailed comparisons are presented in Section 5.

4. COMPUTATIONS

4.1 Introduction

As stated above, of the 49 official registrations received 19 registrants submitted complete (or near complete) results before the deadline date. These form the basis of the synthesis of results described in Section 5. From the PANDA experiment undertaken to form the basis of this 3rd CFD benchmark exercise, a unique set of high-quality measured data have been produced, including velocity measurements in the area of the interaction of the buoyant jet with the density interface. The information provided to the registered participants was: the technical specifications, which include the details of the data requested before release of the detailed measurements; CAD drawings of the PANDA facility; results from off-line characterization tests on the velocity profiles at the outlet of the air-helium injection line; and a list of variables for which the participants were asked to submit their simulation results (in X-Y format).

Blind calculation results, as well as essential information on the codes and models used for the simulations, were submitted by the nineteen participants. In consideration of the limited scope of the OECD/NEA CFD benchmarking exercises (which cannot be compared with the CSNI International Standard Problems, ISPs), no accompanying report was requested from the participants, and thus only incomplete information could be gathered on mesh, modelling details, application of Best Practice Guidelines, etc. Therefore, due to the limited information available, and the agreement that a first synthesis of the results would be prepared by the PSI team without feed-back from the participants (as had been undertaken for the previous two benchmark exercises in the series), this report does not include any analysis of the results, which is expected to be conducted by the individual participants themselves, but only includes the comparisons of the submitted variables with the corresponding test data, highlighting the agreement between calculations and results, and some observations on specific aspects of the simulations that warrant further analysis. In Section 5 below, the word “synthesis” will still be used, but the reader is warned that this Section is more a summary of the simulation activity rather than an actual wrap-up of the exercise. Nevertheless, some specific conclusions and suggestions will be included, which could be useful for any further analysis of the data, interpretation of the results, critical evaluation of models, and their implementation in the numerical codes.

Adopting the format of the reports from the two previous benchmark exercises in this series, the synthesis given here includes a ranking of the contributions. In this case, a weighting has been applied to the separate comparisons, the largest weight being assigned to the time progression of the erosion process of the helium-rich layer — the most important characteristic from a containment safety point of view. Due to the time-scale of this process in this test (7200s), a few participants were not able to complete their simulations of the entire transient by the deadline date. The incomplete submissions have been accepted, but a system of penalties has been applied to the ranking process to ensure fair comparison of all the contributions received.

4.2 Summary of submissions

Nineteen sets of numerical data files were submitted to the PSI ftp site by the deadline date. These are summarised in Table 4.1. The entries only list the main features of the physical models, mesh and simulation times. The few details on the numerical methods used that were asked for are not included.

Table 4.1: Summary of the submissions (grey shaded: Group 1 submissions, using variants of the k- ϵ model and a sufficiently detailed mesh; non-shaded: Group 2 submissions, using other turbulence models, or a very coarse mesh).

User	Code	Turbulence model	Nr. Cells $\times 10^3$	Gas-to-wall heat transfer	Sc_t	D_{AB} (m^2/s) $\times 10^{-5}$	Inlet pipe		Simulation time (s)	Equivalent CPU time (hours)
							Modelled (Wall/Fluid)	Tu Outlet (%)		
1* ^o	Trio_U 1.6.8	k- ϵ	2900	NO	0.7	7	NO	7	2100	105800
6 [#]	P ² REMIC S	k- ϵ	1383	NO	1	7	NO	10	7535	3024
8	CFX 14.5	SST	717		1	N/A			6981	13444
11	CFX 15	k- ω SST	2200	YES	0.9	7.2	YES	8	5272	4960
12 [#]	FLUENT 14	RSM	2077	NO	0.7	7.13	NO	5	7200	1800
17	FLUENT 14.5	k- ω SST	2200	YES	0.7	7	N/Y	5	7200	576
19	STAR-CD 4.20	Low-Reynolds k- ϵ	2064	NO	0.9	6.7	YES	8	7200	68608
20 ^{^o}	CFX-14.5.7	k- ω SST	1612	YES	0.9	Correlation	YES	5 ⁺	4437	20164
32	FLUENT 12.1.2	k- ϵ (realizable)	474	YES	0.7	8	N/Y	13	7200	6960
33	CFX 14.5	SAS-SST	1263	YES	1	=bulk viscosity		7.3	8000	11680
34	CABARET 2.5	ILES	4331	NO	N/A	1.83/1.86	NO		7200	49152
37	OpenFOAM 2.1.1	Modified k- ϵ	2035	NO	1	Correlation	NO	1.56	10500	258048
38* *	Logos 4.0.7	Laminar	300		N/A	N/A		N/A	~ 3000	N/A
39	CFX 14.5	SAS-SST	1203	NO	0.9	7.2	Y/N	5	7200	7392
41	FLUENT 15	k- ϵ	448	NO	0.7	2.88	Y/N	11.8	7200	6600
42	FLUENT 15	LES (dyn. Smagorinsky)	790		0.7	Kin. Theory	YES	N/A	7200	118440
43* o	FLUENT 14	ZLES/WALE	1626	YES	0.7	Kin. Theory	YES	20	2000	145152

45	GOTHIC 8.0(QA)	k- ϵ	4	NO	0.7	2.88		0	7000	3
47	GOTHIC 8.0(QA)	k- ϵ in jet, mixing length elsewhere	8	NO	(1)	0	NO	0	7200	48

*simulation not complete

** very few results submitted

Results for the times at which helium concentration fell below $\chi = 0.2$ are incomplete (helium concentration did not drop below 0.2 within simulation time)

^ simulation stopped shortly after the time of the helium concentration drop at position B_18; results at other elevations incomplete.

+At the pipe inlet (2 m).

^o rms values of velocities not provided

In general, nearly all simulations used second-order space differencing, this now being the accepted standard for CFD simulations. Some of the users, however, used first-order differencing in time, and these submissions are among the “worst”, as measured by the ranking process described in Section 5. Without a sensitivity analysis being undertaken on this issue — and this was not requested in the context of this exercise — it is not possible to correlate these poor predictions with the selected time differencing method, and this issue will not be further addressed here.

It is noted that:

- The majority of submissions derived from the three front-line commercial codes (CFX, FLUENT, STAR-CD). A few submissions used “in-house” CFD codes, and two used an established containment code (GOTHIC), with declared CFD capabilities. Finally, one participant used an open source code (OpenFOAM).
- Without an accompanying sensitivity study, it is not possible to judge whether the nodalisations are sufficiently refined to fully represent the physical processes taking place. Of necessity, since the fluid domain is large, and a transient simulation has to be performed, the grid spacing is much coarser than those considered acceptable in the previous two benchmarks in this series [16,22,23]. It is left to the individual participants to further clarify this important point. Especially for simulations using the LES (Large Eddy Simulation) model to represent turbulence, the use of large cells should be very critically scrutinized.
- Around one half of the participants utilized standard URANS turbulence modelling approaches; i.e. variants of the well-established k- ϵ model, in connection with a mesh that aims to resolve the prevailing flow structures (between 400'000 and 2.2 million cells). The other half used more advanced turbulence modelling approaches (LES, SAS, RSM), or standard modelling on a coarse mesh. For clarity of presentation, the contributions in these two classes of submissions — i.e. those using standard turbulence models, and “others” — are grouped together in the subsequent discussion of the main results in Section 5.
- Nearly all the 19 participants were able to complete the transient simulation (to the requested time of 7200 s), although at considerable computational overhead: the right column of Table 4.1 shows the equivalent CPU time (referred to a single processor). Measured on this scale, the LES simulations would require several years of computation to complete. These data, together with the fact that some users were not able to complete the simulation within the stipulated period (just over nine months), gives testament to how demanding CFD containment simulations still remain, despite the simplifications in the physical modelling deliberately chosen for this benchmark exercise. The computational costs associated with a typical containment simulation using CFD, with a mesh refined enough to capture the important physical processes spatially, and over long enough

simulation times to be regarded as relevant, gives credence to the debate of whether evaluating the scenario using alternative methods, employing much coarser grids, is still viable.

- The modelling of the injection pipe and the flow outlet conditions, though defined exactly in the benchmark specifications, was quite “liberally” interpreted between the individual simulations. For some, the flow development inside the pipe is considered specifically (the YES entry in Table 4.1), and the measured velocity profile and turbulence intensity at the outlet is reproduced by appropriate choice of the pipe inlet conditions. Nevertheless, for most of the simulations, the prescribed velocity profile was used as the inlet boundary condition (at the level of the injection line exit rather than at the 7.3 mm above this where the measurements were taken). In some cases, the obstruction of the pipe below its exit is taken into consideration or not (Y/N or NOT in Table 4.1). With regard to the average turbulence intensity at the pipe outlet adopted by the different participants, this varied over a surprisingly broad range: between 0% and 20%. Considering the spread of the results for some variables describing the subsequent spatial evolution of the flow above the injection, it is suggested that the representation of the pipe, and the exact description of the flow exit conditions, should be carefully examined in any further studies.
- The values assumed for the turbulent Schmidt number Sc ranged from 0.7 to 1.0. Since the best value for the kind of flow addressed here is still disputed, it can be suggested here that any future sensitivity studies should include this parameter.
- Nearly all participants used values for the molecular diffusivity close to $\nu = 7 \times 10^{-5} \text{ m}^2/\text{s}^2$, which is the value most quoted in the technical literature. Four users, however, used smaller values, or zero. For these submissions, the role played by the use of unwarranted values should be evaluated.
- Many users did not consider heat transfer between the gas mixture and the vessel walls. Since the temperature differences within the fluid domain are very small (less than 10 K), it is reasonable to assume that the modelling of the fluid-to-wall heat transfer would not seriously affect the evolution of the helium concentration, or the velocities. Nonetheless, the results submitted for the temperatures would then be invalid, because of the slow warming of the gases in the containment volume, and the gradual warming of the containment vessel which, though insulated on the outside, has a large heat capacity.
- Nearly all submissions using variants of the k- ϵ model included the rms of the vertical velocity as calculated from the turbulent kinetic energy, assuming isotropic flow. One submission (U20) did not include these derived variables.

Table 4.1 does not include an entry related to the use of full buoyancy treatment in the turbulence equations, which is known to affect the mixing of a stratified layer. Since all participants who responded to a specific enquiry confirmed that buoyancy terms were fully considered in their equation set, it is assumed that this is also true for all other simulations (apart obviously for U38, for which laminar flow conditions had been assumed), even though not specifically declared, and any differences occurring in the numerical predictions did not arise from the neglect of an appropriate treatment of the buoyancy forces in the turbulence equations.

4.3 Available data for comparison

The main interest of this exercise was to evaluate the capability of the codes to simulate:

- (a) The rate of progression of the erosion of the helium-rich layer in a containment volume; and
- (b) To reproduce the timescale for the global mixing in the vessel.

The process of erosion is measured by the progressive decrease in helium concentration below a specified value (called here the “quench” value) at increasing elevation above the injection line: for evaluation purposes only, this value was chosen as $\chi_{qu} = 0.2$. Ten sampling line locations were selected to characterise the history of the mixing above the point of injection. These positions are shown in Fig. 4.1a, the corresponding time histories of the measured helium concentrations at these locations being displayed in

Fig. 4.1b, where the “quench” times are also indicated. As the scanning time was 226 s, the uncertainty of the “quench” times is negative (-226 s), as the reduction below the $\chi_{qu} = 0.2$ level can only occur earlier than the time specified.

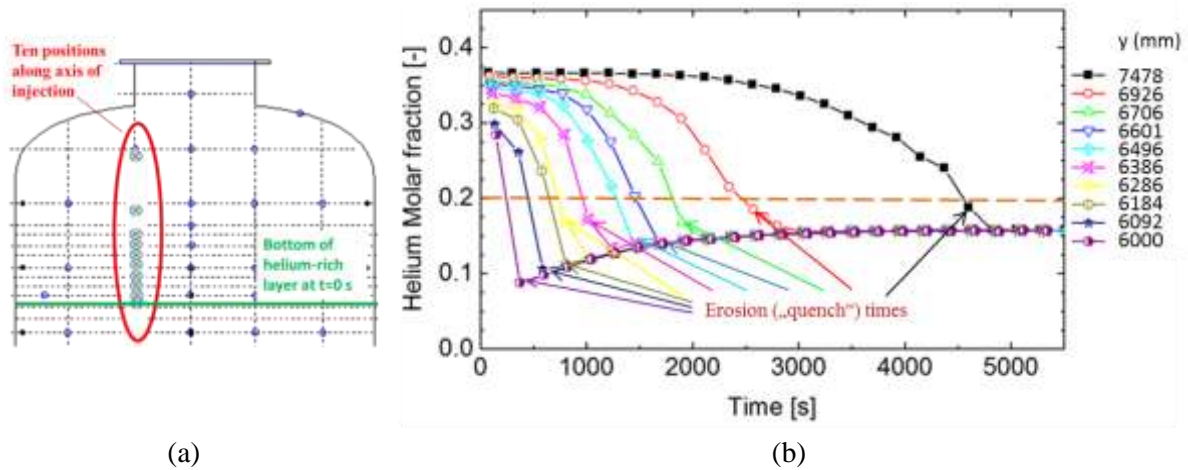


Fig. 4.1 Concentration measurements: (a) positions used for evaluating the erosion of the stratification; (b) the time histories at these positions.

The global mixing can be estimated effectively by considering the time histories of the helium concentrations at the various measurement positions, distributed throughout the vessel, including some along the injection line. Figure 4.1a shows the positions of the measurements used in the present benchmark test. Among the many temperature measurements available, only five have been selected for the benchmark synthesis (Fig. 4.1b). Four of these were used to characterise the temperature decay along the axis of the jet, and one (slightly off-axis) to characterise the transverse temperature distribution a short distance from the pipe exit. The comparison of the calculated results with the data was expected to show the capability of the models to properly represent the transverse heat diffusion, and thereby the broadening, of the jet.

The global mixing can be evaluated considering the time histories of the helium concentrations at the measurement positions in the vessel, including some along the injection line. Figure 4.2a shows the positions of the measurements used in the present benchmark test. Among the many temperature measurements available, just five have been selected (Fig. 4.2b). Four were used to characterise the temperature decay along the axis of the jet, and one (slightly off-axis) to characterise the transverse distribution a short distance above the pipe exit. The comparison of the calculated results with the data was expected to show the capability of the models to properly represent the transverse diffusion and thus the broadening of the jet.

Additionally, seven vertical and horizontal profiles of the mean vertical velocity and the rms (root-mean-square) values of the vertical velocity fluctuations were requested at three specified times during the transient, these to be compared with the values measured by the PIV equipment in the three FOVs (Fig. 4.3). The vertical distributions of turbulent kinetic energy (TKE) along the axis of the injection line at three specified times were also requested, although these variables were considered for consistency purposes only, and were not intended to be used in the ranking process described in Section 5. Nevertheless, it will be shown that the comparison of the TKE vertical distributions is a very useful indicator for a first tentative interpretation of the differences between the various simulations results.

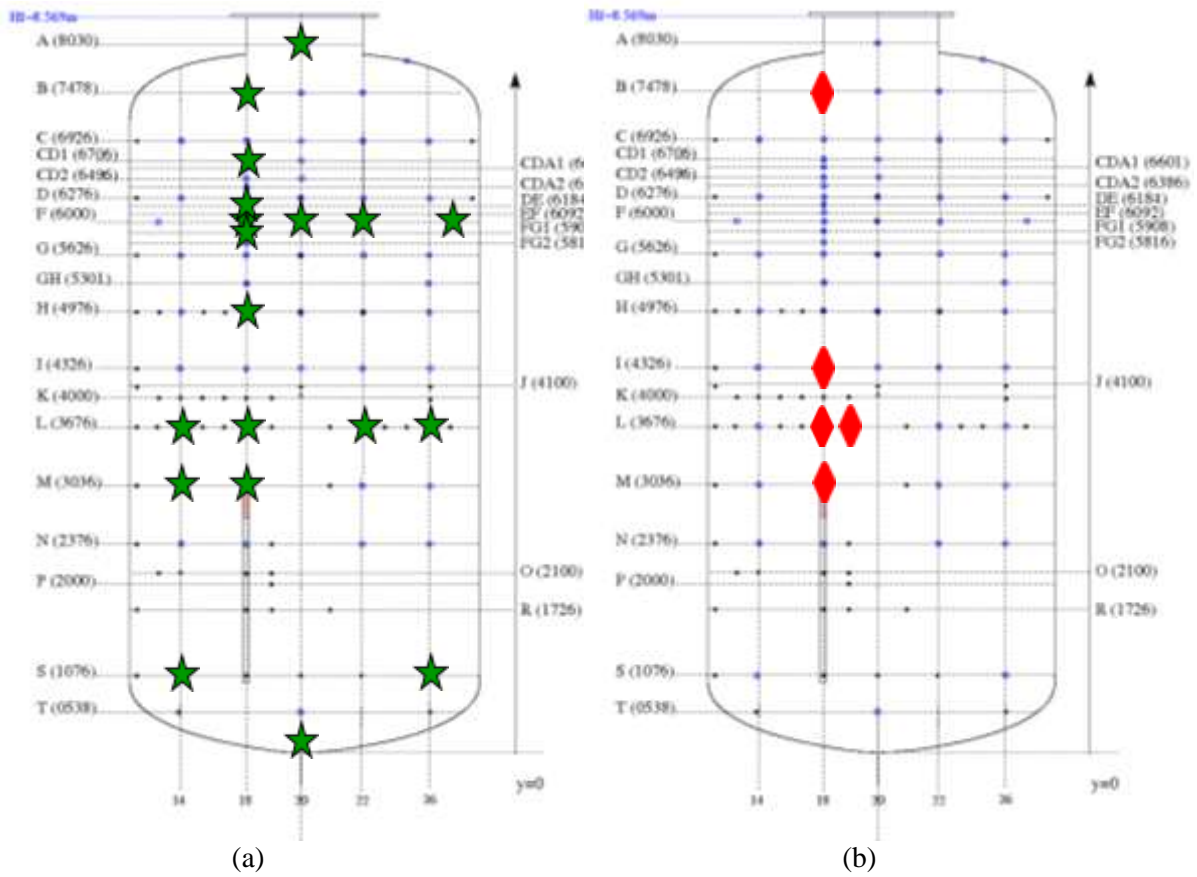


Fig. 4.2 Evaluation of global mixing:
 (a) concentration measurement locations;
 (b) temperature measurement locations.

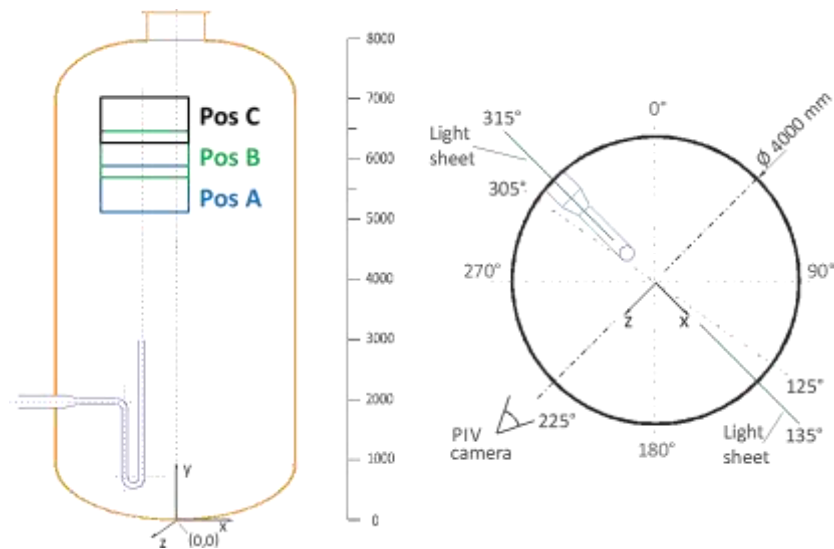


Fig. 4.3: Positions of the fields-of-view (FOVs) of the PIV equipment.

5. SYNTHESIS OF RESULTS

5.1 Main results and comparisons

In this Section, the main results for all 19 submissions are compared against each other, and with the experimental data. For clarity of presentation, results are subdivided into two groups: namely those using variants of the $k-\epsilon$ turbulence model (and employing “typical” CFD-type meshes), and “others”. The simulations are labelled according to user number, turbulence model used, and number of cells (in millions).

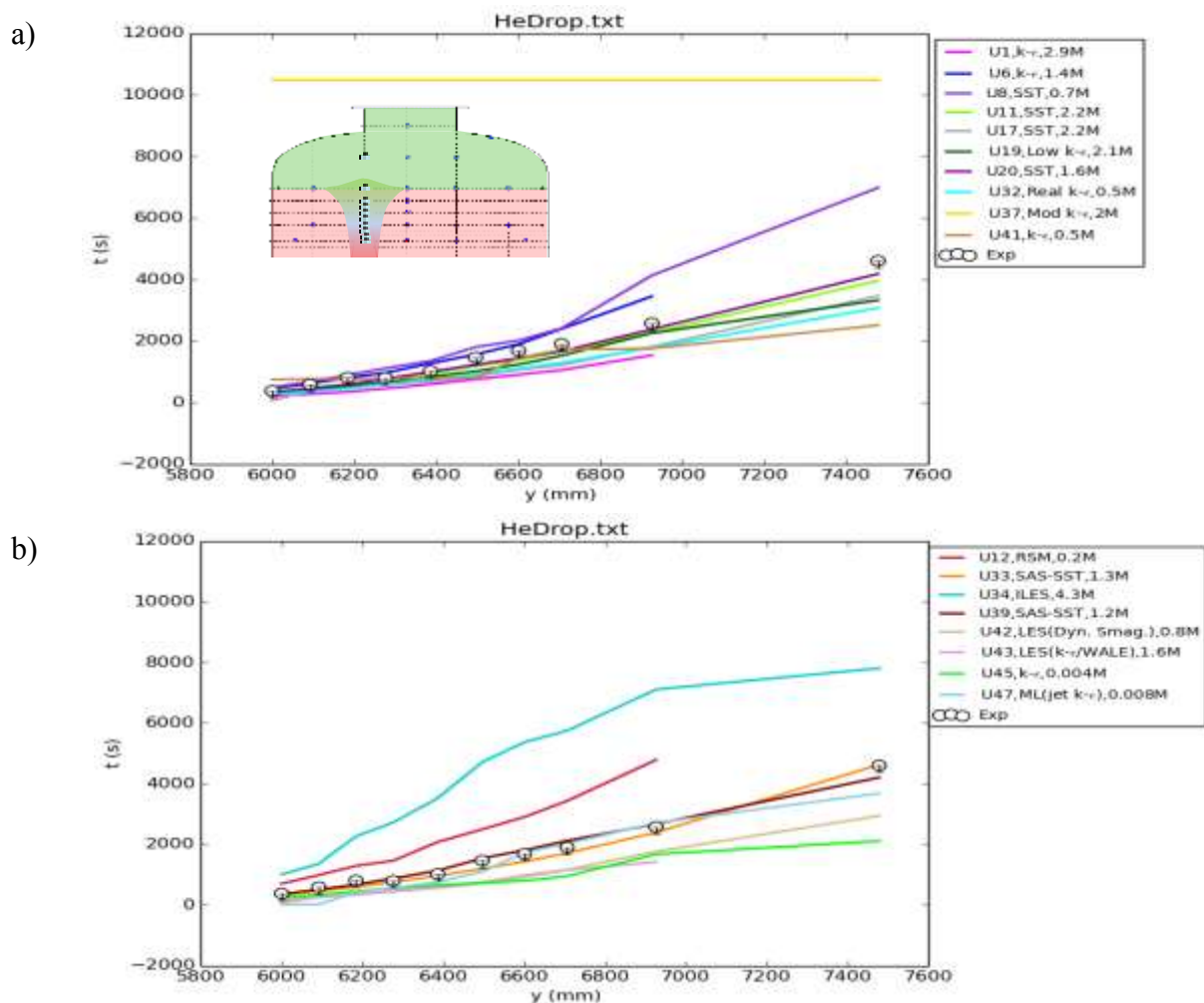


Fig. 5.1 Times for helium concentration to drop to below $\chi = 0.2$ at various elevations along injection line: (a) simulations using variants of the $k-\epsilon$ model; (b) other simulations.

Figure 5.1 shows the times at which the helium concentration drops below the nominated “quench” level of $\chi = 0.2$ at the ten selected elevations along the line of the injection axis. For both groups of calculations, the spread of the results is astonishingly large. It is worth noting that:

- One simulation (U33) accurately predicts the erosion process. Three simulations (U6, U37, U12) do not calculate the drop at the highest elevation within the simulation time, and two (U8, U34) greatly overpredict the time for this occurrence (which the two participants extrapolated from the respective time histories of the concentration, so the discrepancy could be even larger than that depicted in the figure). For these cases, the upwards penetration of the jet is far too slow. All others overpredict the mixing to various extents.
- The variety of results obtained with variants of the k- ϵ model (Fig. 5.1a) is quite large, and even simulations (U11, U17, U20) using the same model (SST), and meshes of similar detail (from 1.6 to 2.2 million cells), produce very different results. It should be noted that the two best results were obtained using the CFX code. It would be interesting if a user would re-run the simulation with the same model choices and mesh, but using two different codes (e.g. CFX and FLUENT), to check whether certain results were dependent on the solver used (and the way the “control volumes” are defined in the two codes) and/or the numerical parameters chosen. Actually, the FLUENT calculation (U17) used default convergence criteria, and some “ragged” curves for other variables (see below) could indicate convergence problems in this case. It is possible that the short simulation time reported by U17 (Table 4.1) was achieved at the penalty of reduced accuracy.
- Although the most accurate simulations were obtained using the SST and SAS turbulence models, it is not obvious that they should be considered superior to the standard k- ϵ model, because this latter model was either used in association base with a coarser mesh or in the framework of in-house codes, for which the validation is certainly not as extensive as for the commercial codes. Moreover, the participants who submitted successful results using the SST model were all familiar with previous tests performed in the PANDA facility. The experience gained could certainly have compensated somewhat for the lack of strict application of Best Practice Guidelines (BPGs) being followed, for which there was no time within the context of this exercise.
- All LES simulations produced either poor, or very poor, results. The use of LES with coarse meshes is anyway rather questionable. These results suggest that accurate simulations for the long transients of interest for containment analysis using this particular advanced turbulence modelling approach are not yet affordable.
- The best predictions seem to have been obtained using the SAS-SST turbulence model (though, as will be seen later, visual impressions will only be partly confirmed by the rankings). It will be shown below that this is true for U33, but that the good results of U39 in Fig. 5.1b could be misleading.
- Surprisingly, very good results (U47) were also obtained with the use of the GOTHIC containment code and very coarse meshing (just 8000 cells). The much worse results obtained by the second GOTHIC user (U45) indicate a strong dependence on success of these coarse-mesh approaches on user experience.

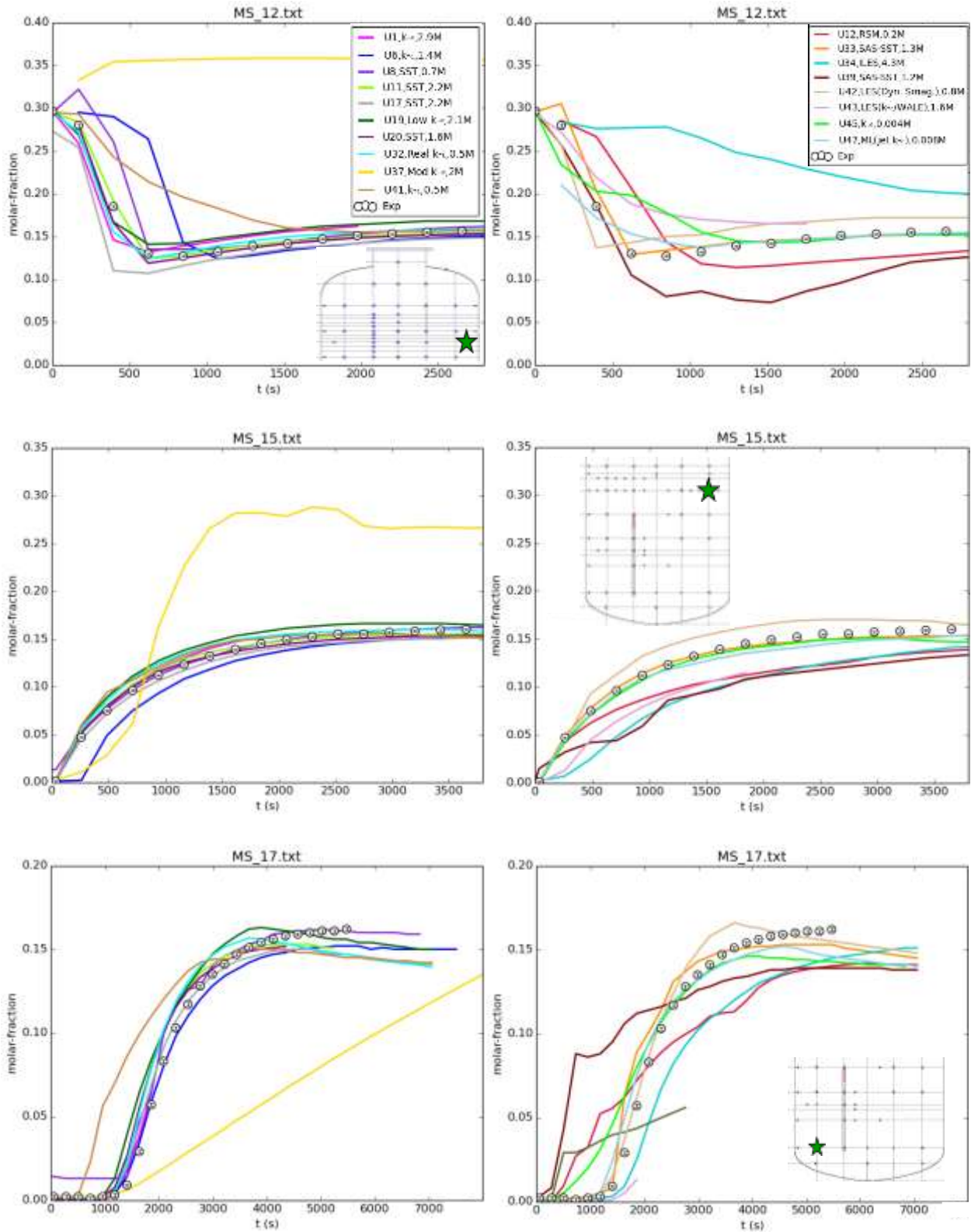


Fig. 5.2: Helium concentration time histories at two positions outside the jet (top: $z = 6$ m; middle: $z = 3.676$ m) and close to the entrance to the vent (bottom).

As regards the issue of global mixing in the vessel, the time histories at two positions away from the jet axis, and one close to the vent at the base of the vessel, are considered for illustrating qualitatively the global performance of the various codes/models. Figure 5.2 shows the calculated and experimental results for the two groups of simulations. Most simulations using variants of the k - ϵ model predict reasonably well the mixing away from the axis of the jet, and the time of propagation of helium down to the vent. On the basis of the MS_17 measurement, only one submission (U37) gives completely wrong results. Another simulation (U41) displays large discrepancies compared with the test data at some positions, but good agreement at others; this must also be regarded as suspicious.

It is interesting to note that the constant value of the vent concentration in the lattermost phase of the transient was captured correctly only by one simulation (U8), whereas all others showed a maximum followed by slow decrease; such behaviour is difficult to explain.

The simulations of the second group (non- k - ϵ turbulence model) also display some interesting characteristics:

- The LES simulations again give very different results, with reasonable agreement only obtained by one user (U42), although this submission consistently overpredicts the equilibrium helium concentrations at all positions.
- One of the two simulations using the SAS model (U33) shows excellent agreement with the test data, although the trend at the vent is less monotonic than that recorded. In particular, a sudden delayed increase is observed just at the time when helium arrives at the location of the vent. U33 is also the only submission, among those correctly reproducing the general trend, that captures also the constant value of the helium concentration at the vent at the end of the transient
- The other simulation using SAS (U39), which did predict the upper layer erosion process quite well, shows a completely unphysical helium concentration evolution at all three positions. Considering the small differences between the mesh and physical parameters adopted by U39 and those of U33, it is difficult to pinpoint what differences in simulation set-up could have resulted in so large a disparity between the results. From the information provided, it appears that both participants used second-order methods, but U33 employed stricter convergence criteria than User U39, and ran the simulation on a 64-bit machine rather than on one with 32-bit precision. To determine whether convergence criteria and arithmetic precision could be responsible for the dramatically different results will be an interesting aspect of any follow-up analyses. These, however, fall outside the scope of this particular benchmark exercise, and are left to the individual participants to pursue.
- Coarse-mesh simulations seem to be capable of capturing the global mixing, with results comparable with those obtained with meshes composed of a number of cells between two and three order of magnitude greater.

The differences in the calculated erosion rates can be partly explained by the different space evolution of the vertical velocity at the requested times. Since the jet is not perfectly centred with respect to the injection axis in the experiment, and the deviations from this ideal condition in the simulations are not known, any comparison has to be accepted with some caution, also because the experimental data are velocities averaged over an interval of about 205s. Moreover, since in the long term the rate of erosion and the associated re-distribution of helium also affects the composition of the ambient in which the jet flows before reaching the density interface, the only meaningful comparison is at the early stage of the transient, when the gas distribution in the ambient is still close to the initial one.

Figure 5.3 shows the vertical distribution of the y -component of velocity along the injection axis at $t = 111$ s in the region of the PIV window PosA (i.e. between heights 5009 mm and 5615 mm). At this time, bearing in mind that the helium concentration distribution did not yet have time to change significantly from that at the jet inlet, the PIV window can be assumed to be fully immersed in the transition region, where the helium concentration increases from values close to zero to about 20% (see Fig. 3.7). It is thus reasonable to assume that, at this early stage in the transient, the velocity at the bottom of the PIV region should be close to that

for a free, round jet. Indeed, considering that the centreline velocity U_c of a round jet decays according to [29,30]:

$$U_c/U_j = K_u d/(y-y_0),$$

where U_j is the average exit velocity, y_0 is the virtual origin, and K_u is a constant (between 5.4 and 6.5 for long pipes, according to the works cited here). Application of this equation results in a value of U_c for a free jet at 2000 mm from the exit of the inlet pipe of between 0.95 m/s and 1.26 m/s. The measured value of around 1.0 m/s at the lower level of the transition region, thus seems to confirm that initially the jet behaves as a free, round jet.

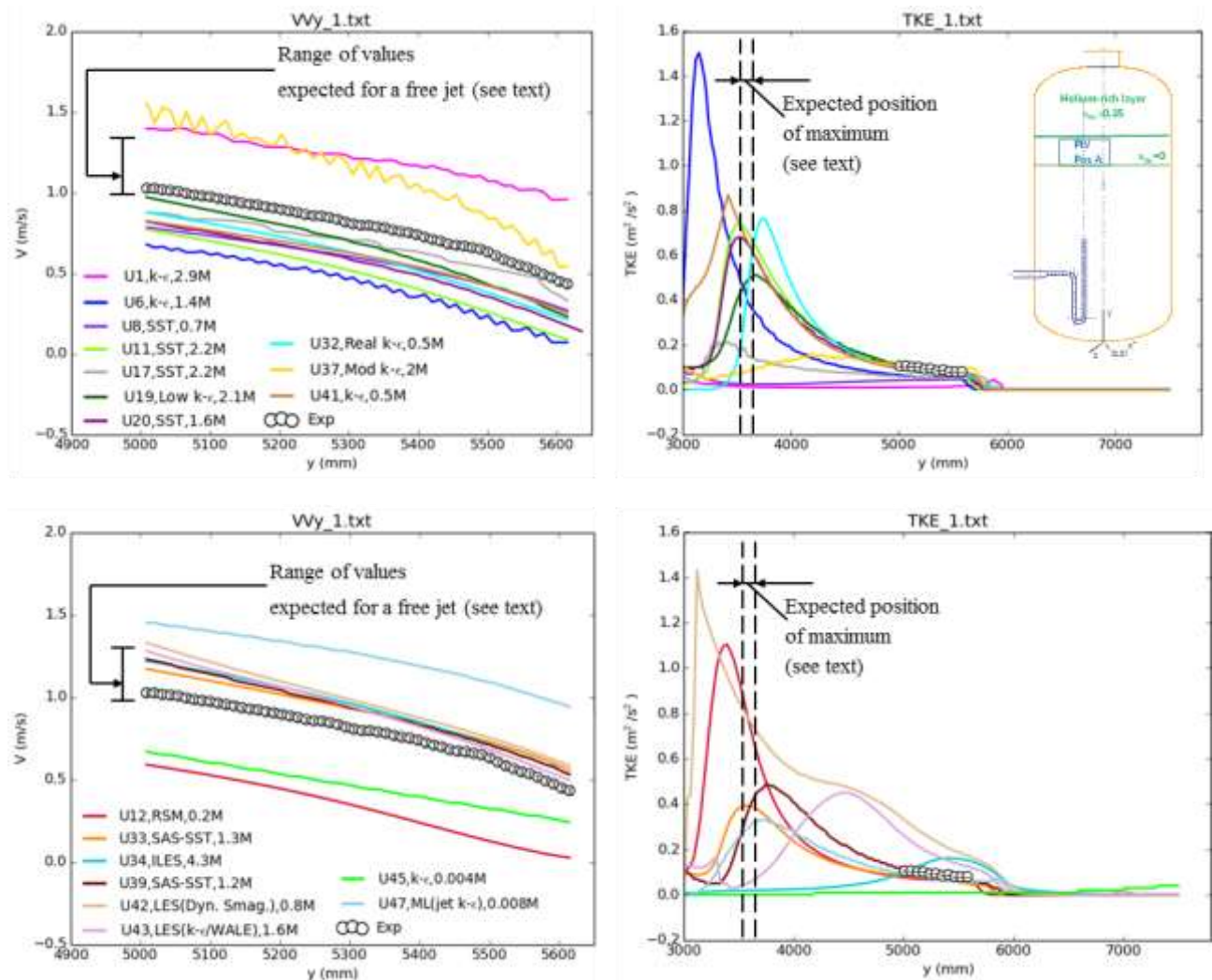


Fig. 5.3 Vertical distribution of the y-component of the velocity along the injection axis at $t = 111$ s (left); and the vertical distribution of TKE along the same vertical line (right).

Top: variants of k- ϵ models; Bottom: other submissions.

Therefore, it is quite surprising that only one submission of the first group (U19) was able to accurately predict the vertical velocity at the bottom of the PIV window at this time, whereas

most of the other simulations were successful in predicting the erosion rate (Fig. 5.1). It is also to be noted that the largest discrepancy amounts to about 40%, which for CFD simulations of a free jet is an unexpected, and an unacceptable result. For this group (with the exception of U11, for which the discrepancy for the

velocity is quite large), a correlation exists between the fidelity in predicting the velocity decay, and the success in predicting the erosion rate.

The simulations of the second group showed a similar dispersion of results, with the two submissions using the SAS model and the two using LES with a subgrid model reproducing the correct trend, and predicting the velocity at the top of the PIV window quite well. One of the coarse-mesh simulations (U47) also produced comparably good results, whereas the simulation with ILES, RSM and the other coarse-mesh simulations fail abjectly to predict the correct velocities. Also, in this case a correlation exists between the success in the prediction of the erosion rate and the prediction of the jet velocity for all calculations, except for the two using LES, which underpredicted the upward penetration of the jet in the helium-rich layer, despite the fact that the approach velocity was slightly overpredicted in both cases.

Valuable insight into the unexpectedly large variation in the numerical predictions, and partly in the ultimate cause of the contradictory results, is offered by the axial evolution of the turbulent kinetic energy (TKE). Figure 5.3 shows that, with the exception of U12, good correspondence of the numerical and measured values seems to be correlated to an underlying good prediction of the TKE in the PIV region, where it was measured in the test. It can be noted that all LES simulations overpredict the TKE, presumably due to the coarseness of the meshes employed contributing excessive numerical diffusion. These results could indicate that the turbulent diffusivity is too large, and the excessive mixing of the incoming jet with the helium-rich layer weakens the jet and thereby delays the erosion process. The disparity of the results, also for simulations featuring the same turbulence model, and meshes of similar resolution, is again quite disturbing, especially when considering the near-field region, where, together with well-behaved evolutions, unphysical trends can easily be identified, with the position of the maximum outside the expected range (i.e. between 7.5 and 8.5 hydraulic diameters, according to [31]).

The variation in the results in the vicinity of the injection pipe exit suggests that the modelling of the pipe, and the implementation of the measured boundary conditions (profiles of velocity and turbulence intensity), may play an important role in determining the capability of the jet to erode the upper layer, and should be considered more carefully in any post-test analyses. Due to the similarity of the initial flow with that of a free, round jet, it is suggested that, before any follow-up simulation is attempted, the model and all parameters (including the numerical ones) should be checked in stand-alone simulations of the basic flow (i.e. of a free jet). Finally, the rather “ragged” shape of the profiles calculated by some participants could indicate convergence problems and/or the presence of numerical instabilities.

A final remark concerning the TKE distribution relates to the trend above the density interface, which was exactly the motivation for requesting this variable from all participants, although there were no direct measurements against which to compare their numerical predictions. Consistency prescribes that the TKE decays quickly above the leading edge of the jet, where it first interacts with the less dense layer above, and where the prevalent negative buoyancy effectively arrests the upward momentum of the jet. In fact, all but one of the submissions was able to reproduce the correct trend, the one exception being U45, for which the completely unphysical trend of the TKE increasing with height well above the density interface was reported; this is one of the two coarse-mesh simulations submitted, and the reason for this totally unphysical behaviour should be investigated.

Some additional general considerations to the fidelity of the various simulations can be gained from a comparison of the calculated results with the two measured temperatures at height $y = 3676$ mm, which were included in the results to be submitted by the participants to the organisers. Figure 5.4 shows the temperatures at the two positions at this elevation, which is less than ten diameters above injection, the first being on the axis of the injection pipe, and the second at a distance 325 mm transverse from this, on a line through the axis of the vessel.

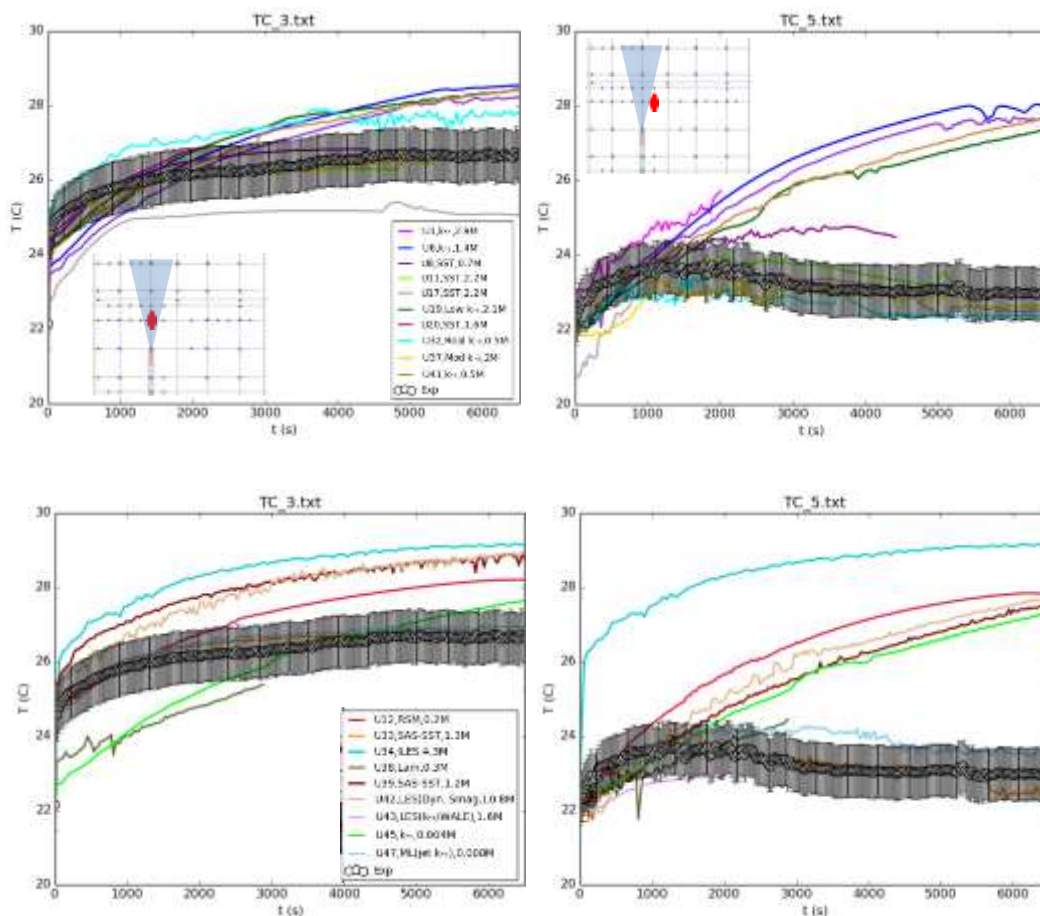


Fig. 5.4: Temperatures at two lateral positions at height $y = 3676$ mm.

Firstly, it can be seen that only the simulations which included modelling of the heat transfer to the wall (Table 4.1) were capable of reproducing the axial decrease of temperature from the pipe exit ($y = 3000$ mm) to Level L ($y = 3676$ mm) during the transient. The largest discrepancy, however, concerns the temperature away from the axis (TC5 in Fig. 5.4). The simulations that did not include the heat transfer from the (slightly heated) gas to the vessel wall exhibit small temperature differences between the inside and outside of the jet, and in some cases even constant temperature conditions, which indicates that the entire temperature field inside the vessel would be poorly predicted. It is also to be noted that most of the simulations that correctly predicted the temperatures, and temperature differences, were also among those that were successful in predicting the erosion rate (i.e. U11, U17, U20, U33, U47). The exception is the U19 simulation, which did not consider heat transfer, but which did predict the erosion rate adequately. From the information available, it is not obvious whether the deviations of the calculated erosion rate from that recorded experimentally during the latter phase of the transient is related to the neglect of this heat transfer mechanism. In general, although it is unlikely that heat transfer played an important role in this test, it could be argued that the choice some users made not to model the gas-to-wall heat transfer was unwarranted, and reflects the general issue for any modelling approach (including CFD): that is, to be able to identify the processes of interest for the particular transients being analysed, and to model them appropriately.

The above comparisons provide a comprehensive picture of the merits and defects of the various modelling approaches, because detailed comparison of the PIV results (distributions of mean velocities and rms values at the requested times) may only be considered meaningful for those simulations that (approximately at least) capture the progression of the upwards displacement of the bottom of the helium-rich layer. These results will be shown in section 5.6 only for the “good” submissions, labelled according to the quantitative ranking procedure detailed below.

5.2 Ranking of the submissions

Following procedures established in the previous two benchmark exercises in this series, a ranking of the submissions has been attempted. As a consequence of the large number of variables considered here, a ranking based on summary scores [32] was preferred to multiple rankings based on individual scores [23]. The ranking process was made difficult by the circumstance that many of the submissions received were not in compliance with the requested format, the simulation time was not always the same, and in some cases the helium concentration at the highest elevations did not drop below the $\chi = 0.2$ level within the simulation time. In some cases also, some points, or entire data files, were not provided. Additionally, by the very nature of a transient calculation, certain comparisons may not be meaningful (e.g. horizontal velocity distributions at prescribed times), because some variables at later times suffer from the errors in the prediction of the progression of the leading edge of the jet accumulated during the transient. Finally, the “global ranking”, and the penalisation adopted, are somewhat arbitrary. However, it will be shown below that a quantitative assessment of the results is still possible, and one that accurately reflects with what one would have intuitively derived on the basis of the visual inspection of the few results displayed in the previous Section. In accordance with the practice established in the two previous benchmark exercises, the ranking is based on simple, linear metrics, with different corrections applied to some variables.

5.2.1 Ranking based on comparisons of stratification layer erosion time

For the ranking of the times when at which the helium concentration drops below the $\chi = 0.2$ level, the following formula has been used to obtain the score:

$$M_{HD} = \frac{1}{N_p} \left(\sum_{i=1}^{N_i} |C_i - D_i| + \max(|C_i - D_i|) \times (N_p - N_i) \right) \times \frac{\Delta y_{exp}}{\Delta y_{calc}}, \quad (11)$$

where C_i and D_i are the calculated and experimental values, respectively. The number of points N_p is the total number of experimental points, and N_i is the number of calculated points provided. The length Δy_{exp} is the elevation difference between the first and last point, whereas Δy_{calc} is the range of y for which results were provided. Interpolation and/or extrapolation of the participants' results was not carried out. Instead, two penalisation procedures, for incomplete submissions, were introduced: the first was applied to incomplete files (i.e. for which $N_i < N_p$), and the second to those simulations that terminated before the helium concentration dropped below the $\chi = 0.2$ level at the highest location. For one submission (U6) the final missing point was replaced by an extrapolated time considering the provided time-history at the uppermost elevation, which indicated that the helium concentration drop at that elevation did not occur before the end of the simulation.

Table 5.1 gives the results of the ranking procedure resulting from the application of Eq. (11). The penalisation affected only four submissions. The quantitative ranking confirms the visual impression obtained before that the two simulations based on the SAS turbulence model are the best. It was stated in the previous Section that for U39 this result is misleading. The Table also shows that the SST model, used within CFX, and which incorporated a detailed mesh, was also very successful. The same model used within FLUENT appears to have produced less accurate results. Surprisingly, the coarse-mesh simulation of U47 ranks fourth according to this criterion.

Table 5.1: Ranking by comparison with times of helium concentration drop below $\chi = 0.2$ on the axis of the injection line.

Ranking	User	Score	Code	Turbulence model	Number of cells (thousands)
1	39	132.13	CFX 14.5	SAS-SST	1203
2	33	142.37	CFX 14.5	SAS-SST	1263
3	11	222.19	CFX 15	k- ω SST	2200
4	47	343.71	GOTHIC 8.0(QA)	k- ϵ in jet region Mixing Length elsewhere	8
5	20*	345.54	CFX-14.5.7	k- ω SST	1612
6	19	377.95	STAR-CD 4.20	Low-Reynolds k- ϵ	2064
7	41	483.03	FLUENT 15	k- ϵ	448
8	17	524.45	FLUENT 14.5	k- ω SST	2200
9	32	524.45	FLUENT 12.1.2	k- ϵ (realizable)	474
10	6	559.69	P ² REMICS	k- ϵ	1383
11	8	603.45	CFX 14.5	SST	717
12	42	638.48	FLUENT 15	LES (dyn. Smagorinsky)	790
13	45	732.85	GOTHIC 8.0	k- ϵ	4
14	1*	979.55	Trio_U 1.6.8	k- ϵ	2900
15	43*	1040.2	FLUENT 14	ZLES/WALE	1626
16	12	1259.63	FLUENT 14	RSM	2077
17	34	2576.65	CABARET 2.5	ILES	4331
18	37	8921.55	OpenFOAM 2.1.1	Modified k- ϵ	2035
19	38*	N/A**	Logos 4.0.7	laminar	300

* penalisation factors applied

**results not submitted

5.2.2 Ranking by comparison with all helium concentration time histories

Also, for the comparison of concentration time histories, some corrections to the simple metrics were necessary, because the simulation times were different, and there was no reason to penalise simulations at times after the helium concentration equilibrium value of $\chi = 0.2$ had been attained. Therefore, for all the submitted results that did not reach the end time of the experimental data, the average discrepancy for the last 4 points was added to the cumulative error for the points that had been supplied.

Table 5.2: Ranking by comparison with helium concentration time histories at all positions.

Ranking	User	Score	Code	Turbulence model	Number of cells (thousands)
1	20*	0.006368	CFX-14.5.7	k- ω SST	1612
2	11*	0.00689	CFX 15	k- ω SST	2200
3	33	0.007225	CFX 14.5	SAS-SST	1263
4	8	0.009779	CFX 14.5	SST	717
5	17	0.010701	FLUENT 14.5	k- ω SST	2200
6	32	0.01243	FLUENT 12.1.2	k- ϵ (realizable)	474
7	1*	0.012504	Trio_U 1.6.8	k- ϵ	2900
8	47	0.013217	GOTHIC 8.0(QA)	k- ϵ in jet region Mixing Length elsewhere	8

9	19	0.013342	STAR-CD 4.20	Low-Reynolds k-ε	2064
10	42	0.016932	FLUENT 15	LES (dyn. Smagorinsky)	790
11	43*	0.02055	FLUENT 14	ZLES/WALE	1626
12	41	0.022966	FLUENT 15	k-ε	448
13	6	0.024746	P ² REMICS	k-ε	1383
14	45	0.024923	GOTHIC 8.0	k-ε	4
15	39	0.025868	CFX 14.5	SAS-SST	1203
16	12	0.026616	FLUENT 14	RSM	2077
17	34	0.038284	CABARET 2.5	ILES	4331
18	38*	0.082866	Logos 4.0.7	laminar	300
19	37	0.115459	OpenFOAM 2.1.1	Modified k-ε	2035

* average of errors for the last four points applied to missing points between end of simulation and end of experimental data recording.

For each individual curve, the following formula was used:

$$M_{C,k} = \frac{1}{N_{P,k}} \left(\sum_{i=1}^{N_{I,k}} |C_{i,k} - D_{i,k}| + \text{avg} \left(|C_{j,k} - D_{j,k}| \right)_{j=N_{I,k}-3N_{I,k}} \times (N_{P,k} - N_{I,k}) \right); \quad k = 1, N_k \quad (12)$$

The global ranking for concentrations was produced considering the sum of the scores:

$$M_C = \frac{1}{N_k} \sum_{k=1}^{N_k} M_{C,k} \quad (13)$$

The ranking resulting from the use of Eqs. (12) and (13) is shown in Table 5.2. The results for the global mixing are quite different from those obtained for the helium layer erosion. The two submissions using CFX and the SST model are the most accurate, followed by the simulation U33 using the SAS model. The other SAS simulation (U39) drops down the list, which is in accordance with the very poor predictions shown in Fig. 5.2. Indeed, also the predictions of most of the concentration time histories show unphysical trends, including those for the positions along the injection line, where, by coincidence, the wrong slopes for the molar fraction decrease curves cross the $\chi = 0.2$ threshold at approximately the right times. It is also noted that the SST model occupies all first five positions in the ranking. The coarse-mesh simulation U47 drops in the ranking to eighth position, but the global results are still acceptable.

5.2.3 Ranking by comparison with PIV data

The ranking relating to the PIV data is affected by the incomplete submissions of some participants. In some cases, the rms curves were not supplied, and in the case of some short simulations, the profiles at the last requested time ($t = 2550$ s) are also missing. However, no penalisation was applied to the score of these participants, since the general conclusions were not affected.

$$M_{V,kk} = \frac{1}{N_{P,kk}} \left(\sum_{i=1}^{N_{I,kk}} |C_{i,kk} - D_{i,kk}| + \max \left(|C_{i,kk} - D_{i,kk}| \right) \times (N_{P,kk} - N_{I,kk}) \right); \quad kk = 1, N_{kk} \quad (14)$$

$$M_V = \frac{1}{N_{kk}} \sum_{kk=1}^{N_{kk}} M_{V,kk}, \quad (15)$$

where $N_{kk} = 20$.

Table 5.3: Ranking by comparison with all distributions of velocity and rms of velocity.

Ranking	User	Score	Code	Turbulence model	Number of cells (in thousands)
1	19	0.030864	STAR-CD 4.20	Low-Reynolds k- ϵ	2064
2	33	0.042677	CFX 14.5	SAS-SST	1263
3	17	0.053371	FLUENT 14.5	k- ω SST	2200
4	11	0.056253	CFX 15	k- ω SST	2200
5	43*	0.069902	FLUENT 14	ZLES/WALE	1626
6	20**	0.085929	CFX-14.5.7	k- ω SST	1612
7	42	0.08851	FLUENT 15	LES (dyn. Smagorinsky)	790
8	41	0.10737	FLUENT 15	k- ϵ	448
9	6	0.112356	P ² REMICS	k- ϵ	1383
10	32	0.112795	FLUENT 12.1.2	k- ϵ (realizable)	474
11	39	0.117372	CFX 14.5	SAS-SST	1203
12	8	0.134797	CFX 14.5	SST	717
13	45	0.136508	GOTHIC 8.0	k- ϵ	4
14	34	0.157637	CABARET 2.5	ILES	4331
15	38*	0.168391	Logos 4.0.7	laminar	300
16	47	0.19163	GOTHIC 8.0(QA)	k- ϵ in jet region Mixing Length elsewhere	8
17	37	0.196789	OpenFOAM 2.1.1	Modified k- ϵ	2035
18	12	0.200418	FLUENT 14	RSM	2077
19	1*	0.238273	Trio_U 1.6.8	k- ϵ	2900

* score based on the reduced number of curves submitted

** rms of velocities not calculated

The ranking resulting from the use of Eqs. (14) and (15) is shown in Table 5.3. Surprisingly, the simulation using the low-Reynolds k- ϵ model is now at the top of the ranking list. The SAS and the SST simulations are also quite accurate, in accordance with the good predictions for the gas concentrations, as already noted. The second unexpected result is the good performance of the LES simulations, incorporating subgrid models. The good results of U43 are somewhat misleading, because they are based only on results at earlier times, but the results of U42 show unambiguously that the mean velocities and rms values calculated by LES are by far calculated better than the concentrations. On the other hand, the coarse-mesh simulation of U47 (where the results at all requested points were obtained by linear interpolation) is quite low in the ranking, as expected.

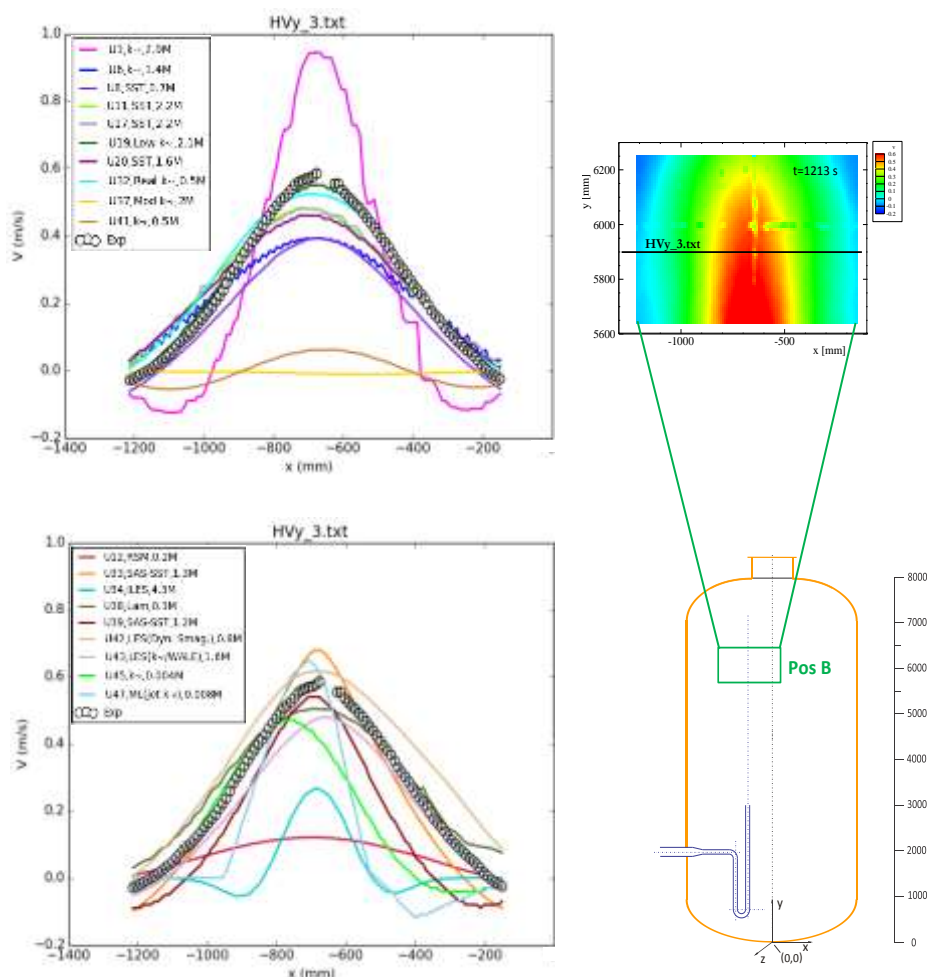


Fig. 5.5: Horizontal velocity profile in the PIV window position PosB at $t = 1213$ s.

As an example, Fig. 5.5 illustrates the quality of the various predictions at window position PosB at $t = 1213$ s. It will be noted that simulation U19 (low-Reynolds $k-\epsilon$ model) predicts the velocity profile very well, including the small region of negative values. The velocity distribution is slightly narrower than those predicted by the most successful SST simulations, and therefore closer to the experimental results. This is true for all profiles of vertical velocity and rms of the velocity. The predictions of U19 are on average better than those of U33 (ranked second), which perfectly reproduce the outer region of the velocity profiles, but overpredict the peak of the horizontal distribution. Figure 5.5 is also a good example of the profiles predicted by U42 and U43 using LES, which are completely different, with opposite deviations from the experimental values. The velocities obtained from the coarse-mesh simulation (U47) exhibit an unphysically narrow profile; at higher elevations, and at later times, the velocities are generally underpredicted.

5.2.4 Ranking by comparison with temperatures

As remarked before, the comparison of temperatures is only meaningful for those simulations that included the modelling of heat transfer between the gas and the vessel walls. Without considering this, the temperature of the entire fluid domain increases, because the long duration of the transient (two hours) makes the small addition of heat due to the warm air injected sufficient to produce a measurable global heat-up. The procedure to calculate the score for this ranking is similar to that used for the concentrations (Section 5.2.2):

$$M_{T,s} = \frac{1}{N_{P,s}} \left(\sum_{i=1}^{N_{I,s}} |C_{i,s} - D_{i,s}| + \text{avg} \left(|C_{j,s} - D_{j,s}| \right)_{j=N_{I,s}-3N_{I,s}} \times (N_{P,s} - N_{I,s}) \right); \quad s = I, N_s \quad (16)$$

$$M_T = \frac{1}{N_s} \sum_{s=1}^{N_s} M_{T,s}, \text{ where } N_s = 5N_s = 5 \quad (17)$$

Table 5.4: Ranking by comparison with temperature time histories at all positions.

Ranking	User	Score	Code	Gas-to-wall heat transfer?	Turbulence model	Number of cells (1000s)
1	11*	0.334318	CFX 15	YES	k- ω SST	2200
2	33	0.353955	CFX 14.5	YES	SAS-SST	1263
3	37	0.48333	OpenFOAM 2.1.1	NO	Modified k- ϵ	2035
4	32	0.537777	FLUENT 12.1.2	YES	k- ϵ (realizable)	474
5	17	0.568504	FLUENT 14.5	YES	k- ω SST	2200
6	43*	0.600564	FLUENT 14	YES	ZLES/WALE	1626
7	47	0.668245	GOTHIC 8.0(QA)	NO	k- ϵ in jet region; mixing length elsewhere	8
8	20*	0.680073	CFX-14.5.7	YES	k- ω SST	1612
9	38**	0.686345	Logos 4.0.7		laminar	300
10	1*	0.912318	Trio_U 1.6.8	NO	k- ϵ	2900
11	41	1.562964	FLUENT 15	NO	k- ϵ	448
12	19	1.564045	STAR-CD 4.20	NO	Low-Reynolds k- ϵ	2064
13	8	1.651109	CFX 14.5		SST	717
14	6	1.672927	P ² REMICS	NO	k- ϵ	1383
15	39	1.680409	CFX 14.5	NO	SAS-SST	1203
16	12	1.820764	FLUENT 14	NO	RSM	2077
17	45	1.908055	GOTHIC 8.0	NO	k- ϵ	4
18	42	1.912491	FLUENT 15		LES (dyn. Smagorinsky)	790
19	34	2.737936	CABARET 2.5	NO	ILES	4331

* average of errors for the last four points applied to missing points between end of simulation and end of experimental data recording.

** score calculated using the reduced number of curves submitted.

The ranking is shown in Table 5.4, where the top positions are still taken by the SAS and SST simulations, with the only exception of position 3, which is occupied by simulation U37 using OpenFOAM and including a modified version of the standard k- ϵ model. Actually, Fig. 5.4 shows that, in regard to temperatures, the predictions of U37 are quite successful. This must be pure coincidence, since all other variables were poorly predicted.

5.3 Global ranking

Finally, to give a global ranking requires a number of somewhat arbitrary choices to be made. Firstly, the four partial scores are dimensional, and therefore they should first be normalised. It was chosen to normalise them using the ranges of the particular variables. For the helium concentration drop times, the range R_{HD} is the time span between the experimental occurrences at the first and last position. For the helium concentration time histories, the range R_C is the maximum concentration at $t = 0$. For the velocities, the

range R_V is the maximum measured velocity. Finally, for temperatures, the range R_T is the difference between the maximum and minimum temperatures at the five positions considered for the benchmark. This reasoning results in the following normalising values:

$$R_{HD} = (4597-373) = 4224 \text{ s}; \quad R_C = 0.367; \quad R_V = 1.026 \text{ m/s}; \quad R_T = (29.25-23) = 6.25 \text{ K}$$

Table 5.5: Global ranking.

Ranking	User	Score	Code	Gas-to-wall heat transfer?	Turbulence model	Number of cells (1000s)	Equiv. CPU time (days)
1	33	0.03239	CFX 14.5	YES	SAS-SST	1263	487
2	11	0.039742	CFX 15	YES	k- ω SST	2200	207
3	20	0.059263	CFX-14.5.7	YES	k- ω SST	1612	840
4	17	0.064848	FLUENT 14.5	YES	k- ω SST	2200	24
5	19	0.069577	STAR-CD 4.20	NO	Low-Reynolds k- ϵ	2064	2859
6	32	0.080718	FLUENT 12.1.2	YES	k- ϵ (realizable)	474	290
7	39	0.091630	CFX 14.5	NO	SAS-SST	1203	308
8	47	0.092185	GOTHIC 8.0(QA)	NO	k- ϵ in jet region mixing length elsewhere	8	2
9	41	0.104910	FLUENT 15	NO	k- ϵ	448	275
10	8	0.105764	CFX 14.5		SST	717	560
11	42	0.108558	FLUENT 15		LES (dyn. Smagorinsky)	790	4935
12	43	0.110651	FLUENT 14	NO	ZLES/WALE	1626	6048
13	6	0.11437	P ² REMICS	NO	k- ϵ	1383	126
14	45	0.134477	GOTHIC 8.0	NO	k- ϵ	4	0.15
15	1	0.144330	Trio_U 1.6.8	NO	k- ϵ	2900	4408
16	12	0.181669	FLUENT 14	NO	RSM	2077	75
17	34	0.276656	CABARET 2.5	NO	ILES	4331	2048
18	37	0.709589	OpenFOAM 2.1.1	NO	Modified k- ϵ	2035	10752
19	38	N/A*	Logos 4.0.7	NO	laminar	300	N/A

* only a few results submitted

The second choice concerns the weighting factors to be applied in producing a global ranking. Since the rate of progress of the stratified layer erosion process and the helium concentrations are the most important parameters here, the following weighting factors have been chosen:

$$W_{HD} = 0.25; \quad W_C = 0.4; \quad W_V = 0.25; \quad W_T = 0.1 \quad (18)$$

The global score for each user was then calculated from the following formula:

$$M = \frac{M_{HD}}{R_{HD}} \times W_{HD} + \frac{M_C}{R_C} \times W_C + \frac{M_V}{R_V} \times W_V + \frac{M_T}{R_T} \times W_T \quad (19)$$

This procedure results in the ranking shown in Table 5.5. The first position is still occupied by one of the SAS simulations (U33), followed by three submissions employing the SST model, with the best two from the use of the CFX code. Good ranking positions have also been achieved by the simulations employing the low Reynolds number $k-\epsilon$ and the realizable $k-\epsilon$ models. The 7th place ranking of the second SAS simulation should be tempered with the unphysical results for some concentrations, which have been already discussed. It is interesting to observe that the best results using the standard $k-\epsilon$ model (in conjunction with the mixing length model in the jet region) have been obtained with a very coarse mesh.

The global ranking confirms that the LES simulations were quite unsuccessful in this application, no doubt because of the need to employ much too coarse a mesh, this being the only option that could be afforded in terms of computer time within the time frame available for delivering the blind numerical data.

Another important consideration concerns the associated computational costs of the simulations. These are also compared in the last column of Table 5.3 in terms of days of equivalent CPU time for a single processor. As can be seen, the accuracy of the simulations does not correlate directly with the cost: quite reasonable results (Rank 4 for U17) were obtained at low computational cost. The much larger computation times necessary for the most successful simulation are not due to the use of any one turbulence model (the SAS simulation of U33 costs less than the SST simulation of U20), but seems to be linked to the use of a particular solver (FLUENT) against another (CFX). Since the results on similar meshes obtained with CFX are better than those obtained with FLUENT, it would be interesting to understand if a smaller gain in accuracy (possibly due to the choice of different numerical parameters) is only possible at the cost of much larger computation times.

5.4 Comparison between selected variables for the highest-ranking simulations

In this Section, only the results of the top five submissions will be compared against the measured data, addressing in more detail the stratification erosion process. The formal rankings (as well as comparisons derived from visual inspection of the main results) provide evidence that the most accurate simulations have predicted all the requested variables reasonably well. The only exception is the submission U19, for which the temperature predictions were poor due to neglect of the heat transfer between the gas and vessel walls. Consequently, in the following discussion, no consideration will be given to the temperature predictions.

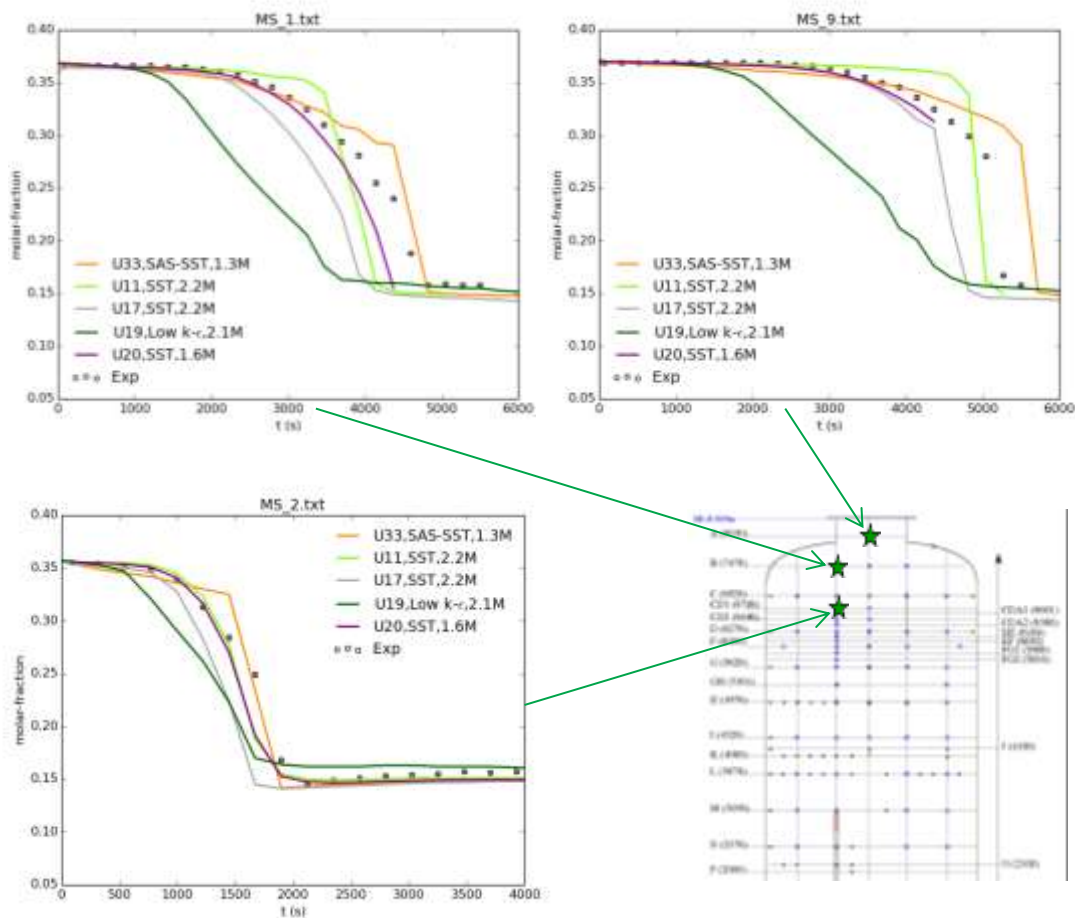


Fig. 5.6: Time-histories of helium concentration at the three uppermost locations:
 A_20 ($y = 8030$ mm); B_18 ($y = 7478$ mm); CD1_18 ($y = 6706$ mm).

Figure 5.6 shows the helium concentrations at the top three locations for which numerical predictions were requested. The uppermost location is just below the man-hole at the top of the vessel (see Fig. 4.1), and is not aligned with the injection axis. The first remark to make is that, from the time-histories, a major qualitative discrepancy in regard to submission U19 becomes immediately apparent. The helium concentration in the dome, and immediately below, starts to decrease much earlier than observed in the test, and is much more gradual. A second consideration can be made regarding the differences between the shapes of the curves predicted in the other simulations. Due to the particular geometry of the dome, the experimental curve at position A_20 exhibits a sudden drop in helium concentration. This behaviour is reproduced by three of the simulations — although at different times — whereas simulation U20 terminates too early.

At the lower position B_18, simulations U33 and U11 predict a sudden drop in helium concentration, whereas the other simulations exhibit a much more gradual decrease. It is interesting to note that the two submissions U11 and U20, so similar in other respects, seem to exhibit different mechanisms for the erosion of the helium-rich layer at this elevation. At the height of CD1_18, however, both simulations exhibit a gradual decrease in helium concentration, qualitatively similar to that predicted by U17. The simulation with the SAS model, instead, always predicts sudden drops, at all elevations. In an attempt to correlate the

different erosion mechanisms seen in the calculations with velocity and turbulence related quantities, horizontal distributions of each at that particular location are considered further.

Figure 5.7 shows the horizontal distribution of the mean vertical velocity and its rms value 260 mm (approximately) below the position CD1_18 (at which the concentration was continuously monitored) at the time $t = 1795$ s, when the helium concentration had just dropped below the threshold value of $\chi = 0.2$. As can be seen, the velocity distribution calculated using SAS is more peaked than the others, and the turbulent fluctuations are smaller than those for U11, especially in the centre, where the distribution exhibits a depression.

These results seem to indicate that in simulation U33 the erosion process is more strongly driven by the penetration of the jet, and less by turbulent diffusion, than for simulations U11 and U17 (which show smaller rms values, but also smaller mean velocities). For simulation U20, the rms values of the velocity components were not provided, and so no comparison can be made in this case.

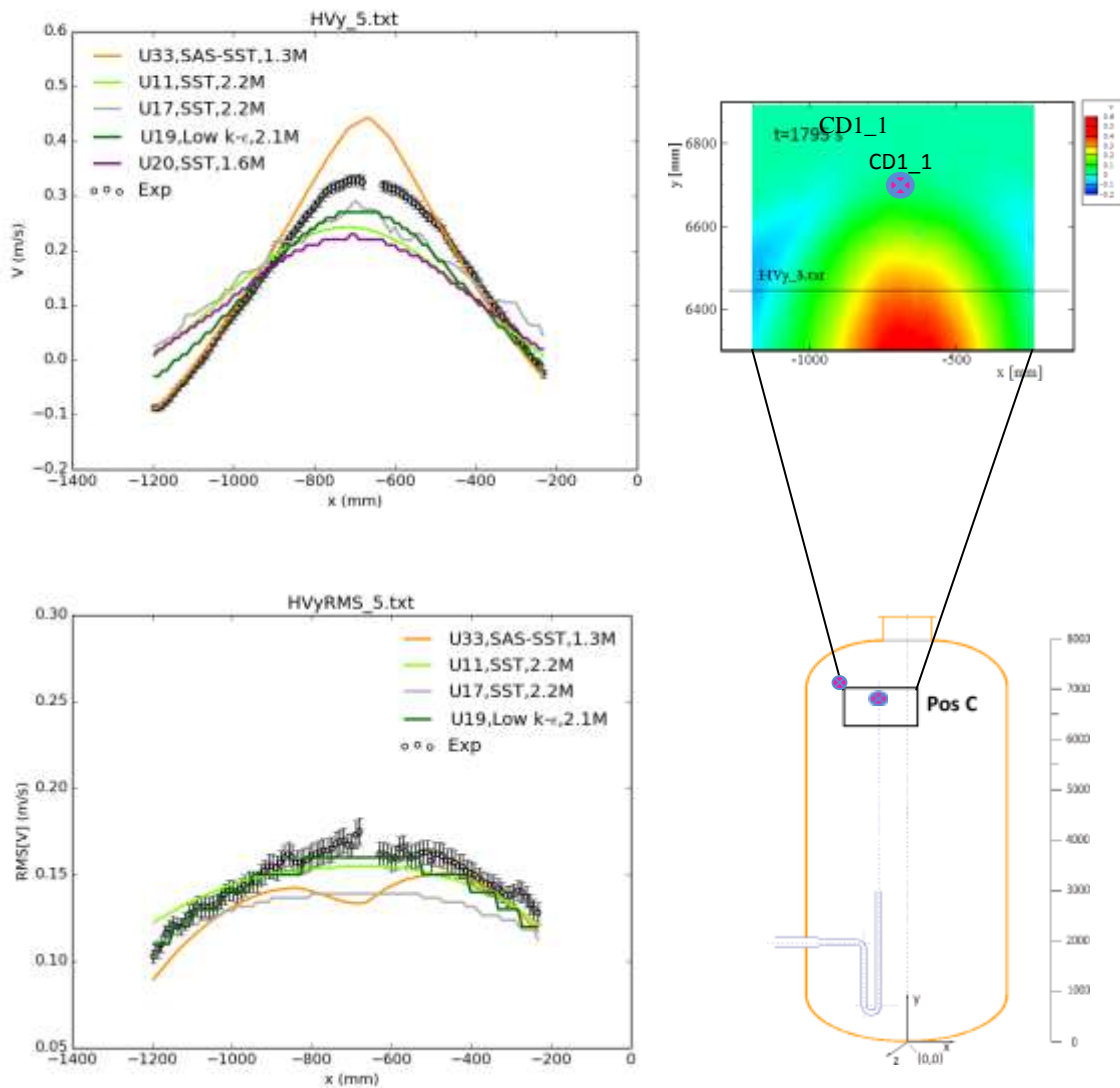


Fig. 5.7: Mean velocity and rms distributions at $t = 1795$ s at $y = 6447.2$ mm, about 260 mm below the position of the concentration measurement CD1_18.

In summary, closer inspection of the turbulence quantities has brought some better understanding of the differences between the modelling of the stratification erosion process, as calculated by the top-ranking simulations. In particular, the too sharp helium concentration drop predicted by the SAS simulation may be correlated to the smaller predicted values of the turbulence level in the centre of the jet, which resulted in a higher peak in the velocity profile.

The origin of the peculiar shape of the distribution in this simulation, and the question whether it is physically reasonable, should be further investigated. Differences between the two SST simulations using CFX and that using FLUENT seem to be related to the smaller turbulence levels predicted in the latter case. Differences between the two CFX predictions, which are noticeable only at some elevations, can only be revealed by a more comprehensive analysis, and this exercise is left to the respective individual participants.

5.5 Summary of the synthesis of results

The first general conclusion to be drawn is that even for such a simple, basic flow situation as the one set up in this exercise, with no complex physical processes taking place, a large spread of numerical predictions has been obtained. The key parameter — the rate of erosion of the stratified, helium-rich layer — was strongly overpredicted in some simulations, while other simulations predicted the persistence of the stratification to the end of the simulation time, itself an overestimate of the time for complete mixing observed in the experiment. This large spread in results, which became more obvious with elapse time into the transient, indicates the need of some learning process is still required in the use of CFD in applications of this type. Hopefully, post-test analyses will identify the reasons for the failure of some simulations to predict the observed events, and the limited correspondence of most of the submitted data to that measured in the test.

No information on the application of the Best Practice Guidelines (BPGs), and studies on the effect of selecting different convergence criteria — the participants were asked to submit what they considered their “best” calculation — it is not obvious at this stage whether strict application of BPGs could have reduced the spread of the results. However, it is clear that an established methodology for performing CFD simulations of the long transients of interest for containment safety analyses needs to be defined. It is recommended that a further update of the CSNI document dedicated to this task [3,10] should be considered.

The characteristics of the meshes adopted by the different participants varied over a broad range, and, in the absence of any accompanying report, it is not clear what criteria were used to arrive the mesh selected for the simulation, and whether this can be deemed adequate given the modelling assumptions. Obviously, in regard to turbulence modelling, a variety of choices were available, and the prevailing use of the most popular variants of the k- ϵ model had been anticipated. However, other modelling options and parameters were quite different for the various submissions, including prescribing the jet injection, and the turbulent Schmidt number. Moreover, the molecular diffusivity was not treated in the same way in all cases, and the heat transfer between the gas and the vessel wall was considered only by a few users. The cumulative effect of all these choices on the accuracy of the predictions is difficult to estimate.

Some simulations predicted fairly well the overall transient, though the success of the calculation (as judged by the ranking procedure) was not obviously correlated with the use of a particular turbulence model. In fact, although the most accurate simulations had employed the SST and the SAS models, it is not obvious that they should be considered superior to the standard k- ϵ model in this context, since this latter model was either used in association with a coarser mesh description, or with in-house or open-source CFD codes, for which the validation is certainly not as extensive as for the major commercial codes.

Disturbingly, the two predictions using the SAS model produced very different results, one of them totally underestimating the overall mixing time, predicting migration of helium to the bottom of the vessel

thousands of seconds earlier than observed in the test. Also the fidelity of the predictions with the SST model was quite different for the three submissions incorporating this model, although mesh, parameters, and other modelling choices, all looked similar. It is worth mentioning also that participants who had adopted this particular model all had previous experience in simulating similar tests in PANDA. One interesting question, which again has to be left to any follow-up studies, is whether the better accuracy of the two simulations using CFX rather than that using FLUENT is due to the differences in the solver, or the reason could be the more stringent convergence criteria applied.

6. FINAL REMARKS

This benchmark exercise, conducted using a similar format to the previous two in the series, proved to be very popular and topical. The initial number of those showing interest by formally registering (49) was much the same as that seen with the previous two benchmarks, but the final number of numerical predictions submitted (19) was less than previously seen (29 for the T-junction benchmark and 25 for the MATiS-H benchmark). Nonetheless, this is a very respectable final number given that the present benchmark involves simulating a two-hour transient in a large vessel.

The PANDA test on which this exercise is based was performed with great professionalism by experts in the field. The benchmark test was run three times to ensure repeatability of conditions. There were multiple checks on the reliability and of the data measurements, some instruments were replaced, recalibrated, sometimes using external agencies. Careful attention was paid to estimating error bounds on the measurements, since this has a direct effect on the subsequent ranking procedure carried out. The result was a first-class set of valuable test data, delivered on time, to serve as the basis for the code comparison exercise. Upon common agreement of protection of proprietary rights, these test data were then made available to all active participants in the benchmark exercise.

A careful synthesis was carried out, also by an expert (M. Andreani) in the field, and one with previous experience in performing this duty in the context of previous OECD-sponsored benchmark exercises involving the PANDA facility. During this process, different ranking procedures were applied for each of the type of measurement performed in the test: velocities, helium concentrations and temperature. Attention was paid to both mean and fluctuating quantities of each. Then, collecting the individual rankings, a global ranking was assigned.

Overall it was concluded that:

- Containment modelling still remains a significant challenge for CFD codes, and those who use them, even in the absence of complex physical phenomena such as phase exchange; e.g. steam condensation. The reason for this is a direct consequence of the large spatial volumes involved, requiring a large number of meshes, and the long simulation times in a typical containment transient.
- As a consequence of the computational overhead, strict application of Best Practice Guidelines (BPGs) is unworkable at the present time for this type of application.
- As a consequence of this shortfall, a good measure of experience is needed on the part of the numerical analyst. Not surprisingly, therefore, best comparisons were obtained from those with previous experience in containment modelling. Another consequence is the large spread in results, taken together.
- The present state-of-the-art in turbulence modelling in terms of RANS (Reynolds Averaged Navier Stokes) formulations appears to be adequate for simulations of this type.
- The employment of advanced turbulence models, such as LES (Large Eddy Simulation) or RSM (Reynolds Stress Modelling) appears not to be justified here, and is anyway unnecessarily time consuming.

- Of the 19 blind simulations received only U33, employing the SAS turbulence model produced acceptable, self-consistent results in terms of velocity and concentration.
- It appears that very few of the modellers had taken the trouble to properly demonstrate that they can accurately reproduce the spreading and subsequent decay of a free jet in undisturbed surroundings, as featured in this application. There is a wealth of experimental data on this to test the adequacy of the numerical approaches. Unless the jet spreading process is adequately captured, the timing of all other events will suffer. Was this simple pre-requisite of accurate modelling properly investigated?

It is recommended that further simulations are carried out now that the test data are open, to reduce the spread in the predictions. Unfortunately, the organising committee of this benchmark exercise do not have the resources to oversee this follow-up endeavour. Nonetheless, it is considered a necessary step to increase the trustworthiness of CFD predictions in containment transients. It is hoped the individual participants have the capacity to do this.

As with the previous two CFD benchmarks in this series, dedicated papers were presented at the CFD4NRS-5 Workshop, which was held at ETH Zurich in September 2014: one described the experimental work in detail, and the other (invited lecture) the results of the synthesis, in which numerical predictions were compared against the test data, and ranked accordingly. Material from these two papers, appropriately paraphrased, makes up the bulk of Sections 3, 4 and 5 of this document. A special open forum Q&A session was also convened at the Workshop.

Readers of this document, and the WGAMA committee in particular, may be interested in the views of the actual participants on how the benchmark exercise was conducted, and how the numerical predictions were assessed, views that have not been taken into account in producing this report. For this reason, each of the 19 participants who submitted blind simulation data have been asked to write their comments, which are reproduced verbatim in Annex 4. The comments and opinions could guide how future benchmark exercises are conducted.

ACKNOWLEDGMENTS

The authors gratefully respect the cooperation they received from their colleagues at PSI, whose names do not appear on the author list of this document. These include J. Dreier, who, from the outset, actively encouraged the promotion of a PANDA test to be used as a basis for this benchmark exercise, D. Paladino, for marshalling the resources of the PANDA experimental team in setting up and carrying through this important containment test to the high standards demanded by the organising committee, and to M. Fehlmann, for producing the CAD files of the PANDA vessel and injection line, and generally providing expert assistance to ensure the accuracy of the Benchmark Specifications.

Also, thanks are due to H.-M. Prasser, as head of the Thermal Hydraulics Laboratory at PSI, for sponsoring this activity, and for hosting the CFD4NRS-5 Workshop at ETH Zurich in September, 2014, to provide a forum by which the individual participants in the benchmark could exchange their experiences, and for arranging the fieldtrip whereby interested parties could visit the PANDA facility.

Last, but certainly not least, thanks are due to the participants themselves, who had the courage to perform the blind simulations, and submit them by the deadline date, to provide the material for the synthesis undertaken, and reported in this document. Sadly, since we, the authors, have strictly maintained our promise of complete anonymity to the contributors, we are not now at liberty to name them directly, and individually. However, we take this opportunity of gratefully acknowledging the efforts you have made in simulating this benchmark test using the numerical tools at your disposal, and sincerely hope you have gained some valuable experience in modelling containment transients of the type here represented, though admittedly in idealistic form. We wish you well on your future endeavours in this application area.

REFERENCES

- [1] “Exploratory meeting of experts to define an action plan on the application of Computational Fluid Dynamics (CFD) to nuclear reactor safety problems”, Aix en Provence, 15-16 May 2002, CSNI Report NEA/CSNI/R(2002)16.
- [2] “Use of Computational Fluid Dynamics (CFD) Codes for Safety Analysis of Reactor Systems including Containment”, Pisa, Italy, 11-14 Nov., 2002.
- [3] Mahaffy, J. (ed.) “Best Practice Guidelines for the Use of CFD in Nuclear Reactor Safety Applications”, OECD, Nuclear Energy Agency, Technical Report, CSNI/R(2007)5, April 2007
- [4] Smith, B.L. (ed.) “Assessment of Computational Fluid Dynamics (CFD) for Nuclear Reactor Safety Problems”, OECD Nuclear Energy Agency, Technical Report, NEA/CSNI/R(2007)13, Jan. 2008.
- [5] Bestion, D. (ed.) “Extension of CFD Codes to Two-Phase Flow Safety Problems”, OECD, Nuclear Energy Agency, Technical Report, NEA/CSNI/R(2010)2, March 2010.
- [6] CFD4NRS: Benchmarking of CFD Codes for Application to Nuclear Reactor Safety, Garching, Munich, Germany, 5-7 Sept. 2006 (CD-ROM).
- [7] Smith, B. L., Hassan, Y. (eds.) “CFD4NRS: Benchmarking of CFD Codes for Application to Nuclear Reactor Safety”, *Special Issue, Nucl. Eng. Des.*, **238**(3), 443-785 (2008).
- [8] Smith, B.L., Bestion, D., Hassan, Y. (eds.) “Experiments and CFD Code Applications to Nuclear Reactor Safety (XCFD4NRS)”, *Special Issue, Nucl. Eng. Des.*, **240**(9), 2075-2382 (2010).
- [9] <http://meta.wikimedia.org/wiki/Help:Introduction>
- [10] Mahaffy, J. (ed.) “Best Practice Guidelines for the use of CFD in Nuclear Reactor Safety Applications – revised”, OECD, Nuclear Energy Agency, Technical Report, CSNI/R(2014)11, Feb. 2015.
- [11] Smith, B.L. (ed.) “Assessment of Computational Fluid Dynamics (CFD) for Nuclear Reactor Safety Problems – revised”, OECD Nuclear Energy Agency, Technical Report, NEA/CSNI/R(2014)12, Feb. 2015.
- [12] Bestion, D. (ed.) “Extension of CFD Codes to Two-Phase Flow Safety Problems – revision”, OECD, Nuclear Energy Agency, Technical Report, NEA/CSNI/R(2014)13, Feb. 2015.
- [13] <http://www.oecd-nea.org/nsd/csni/cfd/>
- [14] Smith, B.L., Mahaffy, J.H, Angele, K, Westin, J. “Report of the OECD/NEA—Vattenfall T-Junction Benchmark Exercise”, OECD, Nuclear Energy Agency, Technical Report, NEA/CSNI/R(2011)5, May 2011.

- [15] Smith, B.L., Mahaffy, J.H., Angele K., “A CFD Benchmarking Exercise based on Flow Mixing in a T-Junction”, Paper 145, 14th Int. Topical Mtg. on Nuclear Thermal Hydraulics (NURETH-14), 25-30 Sept. 2011, Toronto, Canada, CD-ROM, 2011.
- [16] Smith, B.L., Mahaffy, J.H., Angele K., “A CFD benchmarking exercise based on flow mixing in a T-junction”, *Nucl. Eng. Des.*, **264**, 80-88 (2013).
- [17] Rheme, K., Tripe, G. “Pressure Drop and Velocity Distribution in Rod Bundles with Spacer Grids”, *Nucl. Eng. Des.*, **62**, 349 (1980).
- [18] Yao, S.C., Hochreiter, L.E., Leech, W.J. “Heat-Transfer Augmentation in Rod Bundles near Grid-Spacers”, *J. Heat Transfer*, **104**, 76 (1982).
- [19] Shen, Y.F., Cao, Z.D., Yu, Q.G. “An Investigation of Cross-Flow Mixing Effect caused by a Grid Spacer with Mixing Blades in a Rod Bundle”, *Nucl. Eng. Des.*, **125**, 111 (1991).
- [20] McClusky, H.L., Holloway, M.V., *et al.*, “Mapping of the Internal Flow Field in Typical Subchannels of a Support Grid with Vanes”, *J. Fluids Eng.*, **125**, 987 (2003).
- [21] Smith, B.L., Song, C.-H., Chang, S.-K., Lee, J.R., Kim, J.W. “Report of the OECD/NEA-KAERI Rod Bundle CFD Benchmark Exercise”, OECD, Nuclear Energy Agency, Technical Report, NEA/CSNI/R(2013)5, July 2013.
- [22] Smith, B.L., Song, C.-H., Chang, S.-K., Lee, J.R., Amri, A. “The OECD-KAERI CFD Benchmarking Exercise Based on Flow Mixing in a Square Channel”, Paper 166, 15th Int. Topical Mtg. on Nuclear Thermal Hydraulics (NURETH-15), 12-17 May, 2013, Pisa, Italy, CD-ROM, 2013.
- [23] Lee, J. R., Kim, J., Song, C.-H. “A Synthesis of the OECD-KAERI Rod Bundle CFD Benchmark Exercise”, Paper 487, 15th Int. Topical Mtg. on Nuclear Thermal Hydraulics (NURETH-15), 12-17 May, 2013, Pisa, Italy, CD-ROM, 2013.
- [24] www.python.org
- [24a] Andreani, M. “Synthesis of the OECD/NEA–PSI CFD Benchmark Exercise”, Proc., *Application of CFD/CMFD Codes to Nuclear Reactor Safety and Design and their Experimental Validation (CFD4NRS-5)*, OECD/NEA & IAEA Workshop, Swiss Federal Institute of Technology Zurich (ETHZ), Zurich, Switzerland, September 9-11, 2014.
- [24b] Andreani, M., Badillo, A., Kapulla, R., Smith, B. L. “Synthesis of the OECD/NEA-PSI CFD Benchmark Exercise”, Paper 13585, Proc. 16th Int. Topical Mtg. on Nuclear Reactor Thermal Hydraulics (NURETH-16), 30 Aug.– 4 Sept., 2015, Chicago, USA.
- [25] Kapulla, R., Mignot, G., Paranjape, S., Paladino, D. “Stably Stratified Helium Layer Erosion by a Vertical Buoyant Helium-Air Jet”, CFD4NRS-5, Application of CFD/CMFD Codes to Nuclear Reactor Safety and Design and their Experimental Validation, OECD/NEA & IAEA Workshop, Zurich, Switzerland, Sept. 9-11, 2014.
- [26] Kapulla, R., Mignot, G., Paladino, D. “Dynamics of helium stratifications eroded by vertical air jets with different momenta”, Paper 192, 15th Int. Topical Mtg. on Nuclear Thermal Hydraulics (NURETH-15), 12-17 May, 2013, Pisa, Italy, CD-ROM.
- [27] Bloomfield, L.J., Kerr, R.C., “Turbulent fountains in a stratified fluid”, *J. Fluid Mech.*, **358**, 335-356 (1998).

- [28] Paladino, D., Mignot, G., Kapulla, R., Zboray, R., Andreani, M., Tkatschenko, I., Studer, E., Brinster, J. “OECD/SETH-2 Project: PANDA and MISTRA Experiments addressing Key Safety Issues for Water Reactor Containment”, Paper 106, Proc. 15th Int. Topical Mtg. on Nuclear Reactor Thermal Hydraulics (NURETH-15), 12-17 May, 2013, Pisa, Italy. CD-ROM.
- [29] N. Rajaratnam, Turbulent Jets, Elsevier Scientific Publishing Company, New York, 1976.
- [30] Mi, J., Nobes, D.S., Nathan, G.J. Nathan “Influence of jet exit conditions on the passive scalar field of an axisymmetric free jet”, *J. Fluid Mech.*, **432**, 91-125 (2001).
- [31] Boguslawski, L., Popiel, Cz.O. “Flow structure of the free round turbulent jet in the initial region”, *J. Fluid Mech.*, **90**(3), 531-539 (1979).
- [32] Mahaffy, J.H. “Synthesis of Results of the T-Junction Benchmark”, Proc. CFD4NRS-3 Workshop, Washington DC, USA, Sept. 12-14, 2010.

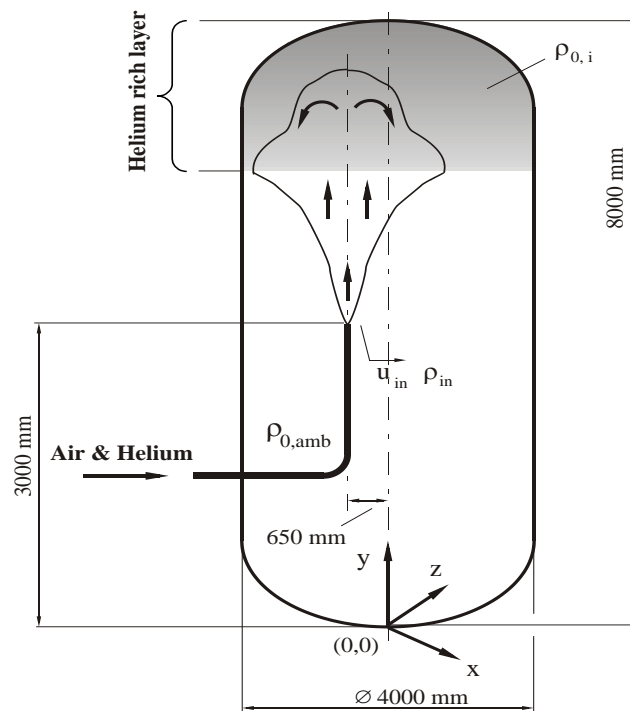
**ANNEX 1: ANNOUNCEMENT
OECD/NEA SPONSORED CFD BENCHMARK EXERCISE:
EROSION OF A STRATIFIED LAYER BY A BUOYANT JET IN A LARGE VOLUME**

Invitation to Participate in and Attend Kick-Off Meeting

NEA Headquarters, 12 boulevard des Iles,
Issy-les-Moulineaux, Paris, FRANCE
25 April, 2013

Background

Hydrogen generated during a severe accident with core degradation remains a major safety issue because explosive mixtures could form in the containment. The recent accident at the Fukushima complex in Japan in March 2011 has refocused attention on this issue. The use of CFD in nuclear engineering is becoming widespread in those modelling situations in which there is a strong multi-dimensional component. Such is the case concerning the build-up of a combustible hydrogen layer in a containment atmosphere following a severe accident, and its subsequent penetration and erosion induced by buoyant jets arising from beneath the layer. The 3-D nature of the gaseous flow generated in such situations invites the use of CFD (or CFD-type) approaches, but such applications are often hampered by the lack of adequate validation data of the basic physical phenomena at the appropriate scales. The current benchmark activity will provide invaluable data in the quest to improve the reliability of numerical simulation of such situations



The PANDA Stratification Experiment

In March/April 2013, a test will be performed in the PANDA facility at PSI. One of the drywell tanks has been isolated from the rest of the facility for the purposes of this test to create a single-vessel configuration. Initially, the drywell vessel is filled with air up to a level above a vertical injection nozzle, placed off-centre, with a stratified layer of helium above. A mixture of air and helium is then injected via the nozzle.

Prior to the test, the PANDA vessel (volume approximately 90 m³) is filled with air and helium at rest in a stably-stratified configuration at a uniform temperature of around 20°C and at about 1.0 bar pressure. At the start of the transient, a helium/air mixture at a mildly elevated temperature (30°C) is injected into the volume via a vertical pipe mid-way between the central axis of the vessel and its outer cylindrical wall. The air/helium concentration, temperature and mean velocity profiles just above the nozzle exit will be provided. Subsequent events are monitored using a number of instruments, including PIV, mass spectrometers and thermocouples, placed at strategic locations. The vessel is vented at the bottom to prevent pressurization. Participants will be requested to supply transient data at selected measuring locations.

A Blind CFD Benchmark Exercise

As a first step in the validation process, this numerical benchmark will examine the turbulent mixing of a two-component gas mixture (air and helium). Notwithstanding the absence of the complications associated with condensation phenomena, the current exercise still constitutes a considerable challenge to numerical analysts working in the field. The data from the experiment will be closed, thus creating conditions for a ‘blind’ benchmark exercise. Subsequently, the data will be opened, but only to those participants who submit blind calculations by the stated deadline.

TRANSIENT CFD SIMULATIONS ARE INVITED

Participants in the exercise will be given details of the test geometry (both in the form of drawings and CAD files in different formats), and operating conditions (i.e. boundary conditions at the injection inlet and initial conditions in the vessel). Using CFD or similar codes, participants are requested to supply to the organizers time-dependent data in the form of temperatures, velocities and gas concentrations at specified locations.

A synthesis of the results, including comparisons against measured data, will be carried out at PSI and reported in the form of a Keynote Lecture at the forthcoming OECD/NEA–IAEA Workshop CFD4NRS-5, which will take place in Switzerland in the autumn of 2014. Participants will have the opportunity to present their work at a special Poster Session at this Workshop, and will have the opportunity to visit the PANDA facility. An accompanying paper will NOT be required.

Registration

Those wishing to participate in the benchmark exercise are requested to register their interest as described below. Registered participants will receive:

1. A copy of the draft Benchmark Specifications for comment as soon as these become available;
2. Further information and updates of the organization and progress of the benchmark activity.

The test details will be presented for the first time at a **Kick-Off Meeting**, to be held at the NEA Headquarters in Paris, France on **Thursday, April 25, 2013**. Those interested in attending this meeting should **register in advance (latest registration April 18, 2013)** with the NEA Secretariat: Abdallah.AMRI@oecd.org, with a copy to Brian.Smith@psi.ch, so that proper arrangements can be made for the attendees at the meeting. An agenda of the meeting is being prepared, and will be circulated beforehand. Those unable to attend, but who nonetheless wish to participate in the exercise, should also register in the same way. This will guarantee their receipt of the Benchmark Specifications in due course.

Preliminary Agenda of the Kick-Off Meeting

A detailed agenda is being compiled, but items to be included are:

- | | |
|--------------------------------------|-------------------------------------|
| • Schedule of the Benchmark Activity | Brian L. Smith, PSI, Switzerland |
| • OECD/NEA Requirements | Abdallah Amri, NEA, France |
| • Test Facility and Instrumentation | Domenico Paladino, PSI, Switzerland |
| • Benchmark Specifications | Brian L. Smith |
| • Synthesis and Reporting Procedure | Michele Andreani, PSI, Switzerland |
| • Open Forum Discussion | |

Organising Committee

Brian L. Smith, Paul Scherrer Institute (PSI),	Switzerland
Domenico Paladino, Paul Scherrer Institute (PSI),	Switzerland
Dominique Bestion, Commissariat à l’Energie Atomique (CEA),	France
Ghani Zigh, US Nuclear Regulatory Commission,	USA
Michele Andreani, Paul Scherrer Institute (PSI),	Switzerland
Abdallah Amri, OECD Nuclear Energy Agency	France (Secretariat)

Dates & Deadlines

April 18, 2013	Registration
April 18, 2013	Notice of Attendance at Kick-Off Meeting
April 25, 2013	Kick-Off Meeting of OECD/NEA–PSI CFD Benchmark
May 24, 2013	Distribution of Initial Benchmark Specifications (for Comment)
June 21, 2013	Distribution of Final Benchmark Specifications
April 30, 2014	Deadline for Receipt of Simulation Results
May 31, 2014	Latest Date for Open Benchmark Meeting & Opening of Test Data
Sept. 30, 2014	Latest Date for Presentation of Synthesis at CFD4NRS-5 Workshop

ANNEX 2: SPECIFICATIONS
OECD/NEA–PSI CFD BENCHMARK SPECIFICATIONS
FINAL VERSION

A0. PRELIMINARY REMARKS

This document contains the final geometrical and flow specifications of the PANDA test forming the basis of this benchmark exercise, and supersedes any previous versions. The figures included here are principally for orientation purposes. Actual design drawings (except for the specially constructed gas injection line used in this test) on which dimensions are to be read are supplied in the five attachments (At1–At5). Note that all dimensions given on these drawings are *as-design*, and manufacturing tolerances will apply to the *as-built* information supplied in the subsequent Tables. Estimates of the tolerances are 30 mm in the vertical direction and 16 mm in the horizontal direction.

To aid mesh generation, a CAD file of the test geometry (PANDA Drywell vessel plus inlet pipe) is being made available on the PSI ftp site. Registered participants to this benchmark are invited to contact the site manager (michele.andreani@psi.ch) to receive a username and password to gain access to the information contained on this site. The CAD file is also subject to manufacturing tolerances, though every precaution has been made to ensure the information is as accurate as possible. The CAD file has been created using *Autodesk Inventor* software. The file extension is .stp and is in ASCII format; this should be easily read by most CFD grid generation packages. However, if participants wish to have an .igs version, this is also available upon request, though is less accurate. Images of the PANDA vessel produced from the CAD file are shown in Fig. A1. Note the manhole arrangement at the top of the vessel, the various penetrations (most of them not utilised for this test), and the U-tube gas injection line.

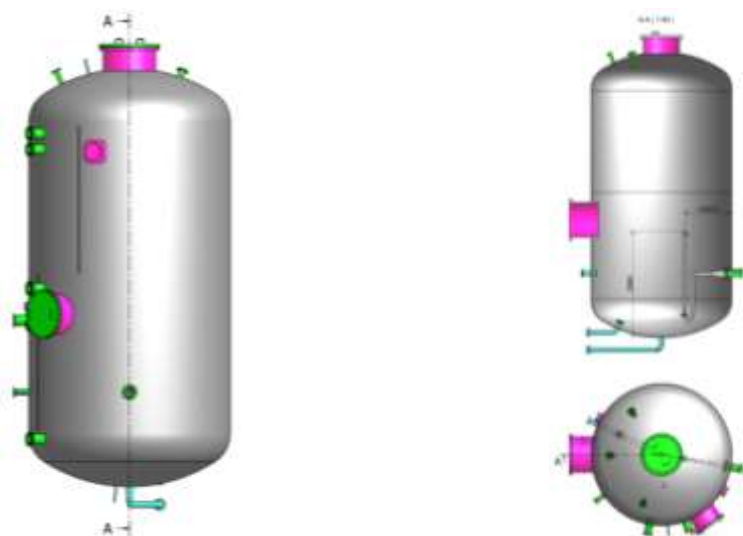


Figure A1: Images of the PANDA vessel obtained using the *Autodesk Inventor* software.

WARNING: Some spurious (horizontal) plane surfaces have been noticed on the images created from the .stp file when read using a popular CFD grid-generation software package. These surfaces do not appear if the file is read using the original CAD software (Fig. A1), and so must arise as a result of interfacing errors between the CAD file and the CFD software. The organisers cannot accept responsibility for data conversion errors in the use of particular CFD software packages. Participants are therefore requested to refer back to the supplied PANDA design drawings in cases of doubt, and/or to contact their software suppliers for advice. Also, use of the .igs file has resulted in some PANDA components not being properly represented in the CFD model. All participants are therefore requested to use the supplied CAD file with caution, and always to refer back to the design drawings in case of doubt.

A1. GEOMETRICAL INFORMATION

A1.1 Experimental Test Section

The PANDA facility is a multi-compartment, large-scale thermal-hydraulics test rig located at the Paul Scherrer Institute, Switzerland. One vessel, which has been isolated from the other large vessels specifically for this test, constitutes the test section for this CFD benchmark; see Figs. A2, A3.

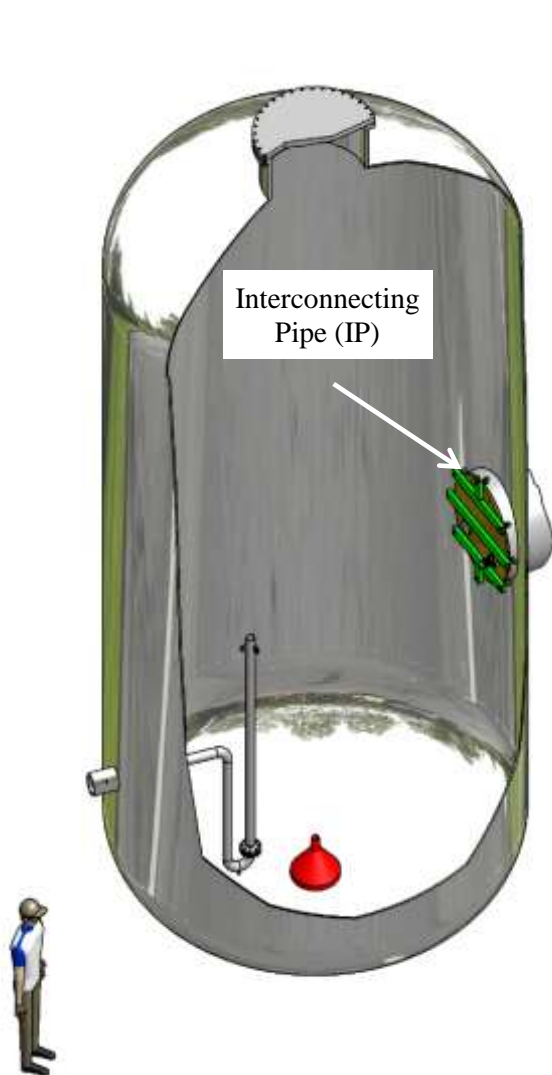


Figure A2: 3-D schematic of the PANDA test vessel and inlet jet arrangement.

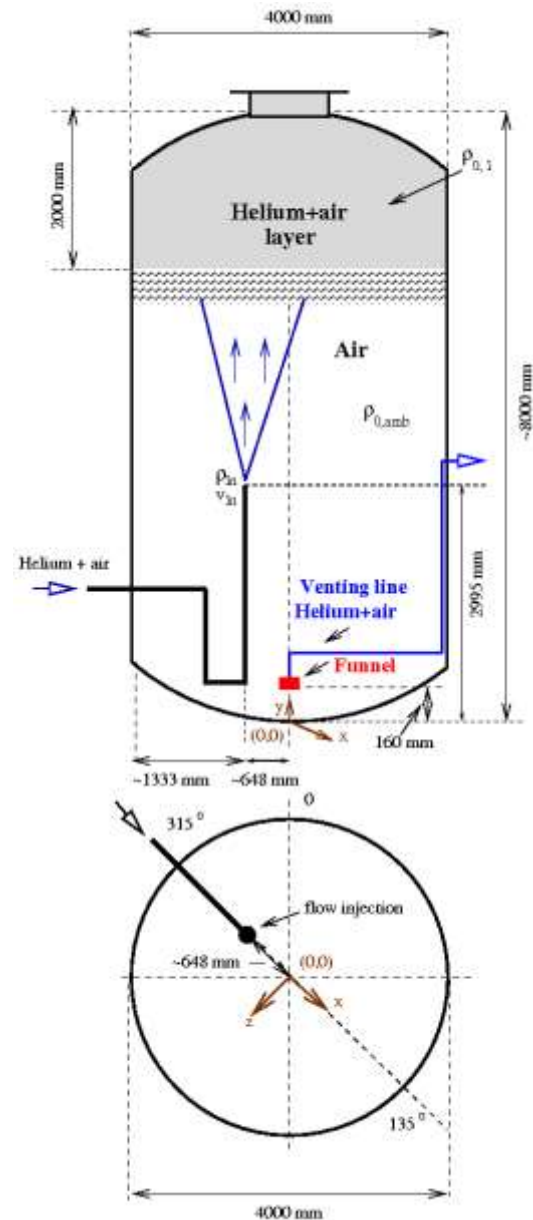


Figure A3: Side and plan views of the test configuration showing the coordinate frame.

N.B. dimensions are approximate only – see text and supplied PANDA design drawings for precise values.

The test vessel is composed of four sections, each of 4 m outer diameter but with varying inner diameters, depending on the local wall thickness. Two cylindrical sections make up the central part, with curved top

and bottom caps welded on. The principal *as-built* dimensions of the four sections are summarised in Table A1.

Table A1: Vessel *as-built* geometrical data.

	Height [mm]	Inner Diam. [mm]	Wall Thickness [mm]	Inner Volume [m ³]	Inner Area [m ²]
Bottom Cap	1069	3957	21.5	8.91	17.85
Section 1 (lower)	3000	3961	19.5	36.96	37.33
Section 2 (upper)	2850	3964	18	35.17	35.49
Top Cap	1065	3960	20	8.85*	17.04*
Manhole	464 [±]	980	35	0.35	2.18
Total Vessel	8409 [#]	-	-	90.24	109.89

* The area and volume of the top cap have been calculated considering the geometrical modification produced by the presence of the manhole.

[±] The height of the manhole is measured from the horizontal plane through the rim of the manhole orifice to the underside of the lid (see attachment At5). The lid (stainless steel DIN 1.4571) is of thickness 50 mm and insulated with rock wool.

[#] The total height is measured from the lowest internal point of the vessel to the underside of the manhole lid along the axis of the vessel.

Details of the geometry of the curved bottom and top sections of the vessel (caps) are shown schematically in Fig. A4, with the actual values corresponding to the symbols given in Table A2.

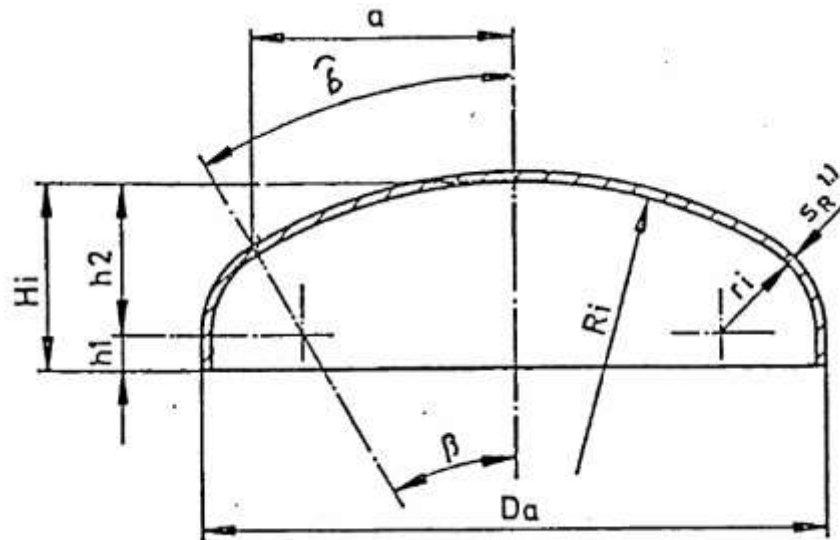


Figure A4: Drawing representing the main parameters of the top and bottom end caps of the test vessel.

Table A2: Explanation of symbols in Figure A4.

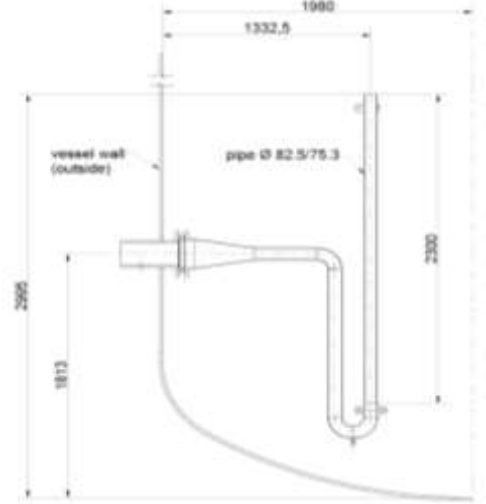

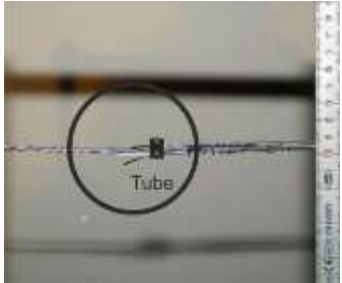
Description	Symbol	Units	Bottom Cap	Top Cap
Outer diameter	Da	mm	4000	4000
Wall thickness	S _R	mm	21.5	20.0
Large curvature radius	Ri	mm	3200	3200
Opening angle large curvature	β	deg.	31.82	31.86
Small curvature radius	ri	mm	616	616
Height cylindrical part	h1	mm	64.5	60
Height curved part	h2	mm	1004.5	1005
Inner height	Hi	mm	1069	1065

It should be noted that the cylindrical sections are not identical, nor are the top and bottom caps. Moreover, a 980 mm diameter manhole exists at the top of the test vessel (used for access purposes); its presence adds an extra 464 mm to the vessel internal height. The exact *as-designed* geometry is presented in the attached drawings At2 and At5. All the sections are made from stainless steel (DIN 1.4571); see Section A2 for information on the material properties. The total enclosed volume within the vessel (including the manhole space) is 90.24 m³, and the total internal surface area (including the top and side manhole surfaces) is 108.49 m².

A1.2 Details of the Gas Injection and Vent Line Arrangements

Main Components

A vertical injection line of internal diameter 75.3 mm and wall thickness 3.6 mm is placed at a horizontal distance of 647.5 mm (nominally 650 mm) from the axis of the test vessel on the 315° azimuthal angle according to the coordinate system defined in Fig. A3. The outlet from the injection line is located 2995 mm (nominally 3000 mm) above the lowest point on the axis of the vessel – at an absolute height of 14695 mm (nominally 14700 mm) above the reference level, which is the concrete base mat of the PANDA building), and is positioned vertically to produce a gas jet directed upwards. The pipe is connected to the flange/penetration 433 (Table A3; reference drawing At2). Figure A5 is a schematic showing the main geometrical specifications of the injection pipe. Figure A6 is a photo of the vessel internal arrangement. The straight section of the inlet pipe upstream from the outlet orifice is more than 30 diameters in length. The inlet pipe has been constructed specifically for this PANDA benchmark test. The flow injection temperature and concentration have been measured during the test at a distance of 36 mm above the pipe outlet in the core of the emerging jet; a top-view photo showing the support wire and instrumentation is given in Fig. A7.

		
<p>Figure A5: Drawing and geometrical specifications of the injection line.</p>	<p>Figure A6: View inside the PANDA vessel showing injection and vent lines.</p>	<p>Figure A7: Photo of the measuring devices 36 mm above the injection line outlet.</p>

The venting of the air/helium mixture from the vessel is made via a funnel oriented downwards (red component in Fig. A6) located just above (maximum gap ~ 160 mm) the base of the vessel. Figures A3 and A6 show the funnel arrangement in schematic and photographic forms, respectively. The blue pipe (Fig. A6) shows the flexible tube used for venting the vessel to maintain the ambient pressure. For convenience, the venting is made via the large interconnecting pipe (IP in Fig. A2), which has been blocked off specifically for this test. Note that the end of the interconnecting pipe is not flush with the inner surface of the PANDA vessel, but protrudes into it a distance 190 mm; details of the geometry are given in Table A3, which contains references to the relevant design drawings.

The velocity conditions at the outlet of the injection line were measured 7.3 mm above the end of the injection pipe in a separate, ex-vessel test; details are given in Section A3. It was not possible to measure conditions exactly at the pipe outlet, so some jet expansion is to be expected as the gas exits the injection pipe. At the measurement location, it is considered (Froude number of jet ~ 17) that there is negligible influence from the surrounding conditions in the vessel for the core flow. Practitioners may wish to examine this issue for themselves, depending on where they choose to place the vessel inlet boundary. It should be mentioned also that the blockage effect of the mass spectroscopy and thermocouple instruments, supported by the wire traversing the flow (Fig. A7), was not present when the velocity profiles were measured during the ex-vessel test (Section A3).

Other Components

In addition to the internal injection pipe, there are a number of penetrations and flanges projecting into the vessel. These are not used in the present test, but their descriptions are included in the attached drawings in case participants might want to take into account the blockage effect they represent. The main flanges are listed in Table A3. Note that the elevations are given with respect to the concrete floor of the PANDA building (zero reference level). On this scale, the lowest internal point within the test vessel (at the geometric centre of the bottom cap, on the axis of the vessel) is at a nominal elevation of 11700 mm.

Table A3: Characteristics of the major penetrations/flanges in the PANDA test vessel.

No.	Ref. Drawing	Nominal Diameter [mm]	Design Elevation [mm]	As-Built Elevation [mm]	Azimuthal Orientation α [°]	Vertical Orientation β [°]	Outer Diameter [mm]	Inner Diameter [mm]
400	At2	1000	15000	15014	125	-	1000	928
401	At5	1000	-	-	-	Top: 0	1050	980
410	At4	700	15000	15014	0	-	784	700
433	At2	150	13500	13513	315	-	203	156

Flange 400: Large dry-well connection pipe

Flange 401: Top manhole

Flange 410: Mid-height manhole

Flange 433: Main injection line

For this test, the entrance to the large dry-well connection pipe has been sealed by an aluminium plate of thickness 25 mm. The back of this plate is insulated with a 19 mm thick Aeroflex® sheet. Material properties of both the plate and the insulation material are given in Table A4.

A2. MATERIAL PROPERTIES

The experiment is conducted under ambient conditions: i.e. at nominal atmospheric pressure, measured internally in the vessel at 0.994 bar (standard deviation 0.003 bar). The gases in the vessel (helium/air mixture at the top, and air below) are nominally at room temperature (20°C), but reference should be made to Fig. A9 for precise details. The temperature of the injected air/helium mixture is slightly elevated (23.0°C, rising to 29.3°C during the course of the test). Full details are given in Section A3 (Fig. A10) below.

The PANDA vessel and the major internal penetrations/flanges are made from stainless steel (DIN 1.4571). All external surfaces have been insulated using two layers of Rock-Wool 133®, each 100 mm thick. The heat losses from all the PANDA vessels have been experimentally determined over a range of temperatures much higher than those encountered in the present test. This was done by internally heating up the vessel with steam to a pressure of about 4 bar and a temperature of 145°C, and measuring the cool-down over a period of about 2½ days. The present test is carried out at ambient temperature (nominally 20°C), except for the slightly elevated temperature (23.0°C to 29.3°C) of the incoming air/helium mixture at the injection pipe outlet. Consequently, the heat losses in this test are considered to be small over its duration (2 hrs.). However, for those participants who wish to examine this issue, properties of the relevant wall and insulation materials are provided in Table A4.

The 2300 mm long straight section of the injection pipe (Fig. A5) is made of the same grade of stainless steel as used for the PANDA vessel (DIN 1.4571). The rest of the injection line, including flanges, is made from stainless steel DIN 1.4404, the material properties of which are also included in Table A4.

The humidity given in Table A5 has been calculated from the nominal pressure (top row of Table A4) according to the National Institute of Standards and Technology (NIST) property database, to be found on the following website: <http://webbook.nist.gov/chemistry/>.

Table A4: Material properties.

Air	Nominal pressure (at altitude 348m): 0.994 bar (standard dev. 0.003 bar); humidity depends on atmospheric conditions (see Table A5)	
Helium 4.6	Purity: > 99.996 %	
Steel (DIN 1.4571)	Major constituent is Fe; others are listed here	C≤0.08%; Si≤1.0%; Mn≤2%; P≤0.045%; S≤0.03%; Cr~16.5-18.5% ; Mo~2.0-2.5%; Ni~10.5-13.5%; 5xC<Ti≤ 0.7%
	Density (20°C)	8000.0 [kg/m ³]
	Thermal conductivity (20°C)	15.0 [W/mK]
	Specific heat (20°C)	500 [J/kg.K]
	Thermal expansion coefficient (20-100°C)	16.5×10 ⁻⁶ [/K]
Steel (DIN 1.4404)	Major constituent is Fe; others are listed here	C≤0.03%; Si≤1.0%; Mn≤2%; P≤0.045%; S≤0.03%; Cr~16.5-18.5% ; Mo~2.0-2.5%; Ni~10.0-13.0%; N≤0.11%.
	Density (20°C)	8000 [kg/m ³]
	Thermal conductivity (20°C)	15.0 [W/mK]
	Specific heat (20°C)	500 [J/kg.K]
	Thermal expansion coefficient (20-100°C)	16.0×10 ⁻⁶ [/K]
Rock-Wool 133 [®]	Density	40.0 [kg/m ³]
	Specific heat	3040 [J/kg.K]
	Thermal conductivity	0.038 (20°C); 0.041 (30°C) [W/m.K]
Aluminium IP cover plate	Density	2700 [kg/m ³]
	Specific heat	910 [J/kg.K]
	Thermal conductivity	237.0 [W/m.K]
Aeroflex [®]	Density	60.0 [kg/m ³]
	Specific heat	2500 [J/kg.K]
	Thermal conductivity	0.0356 (24°C) [W/m.K]

A3. INITIAL AND BOUNDARY CONDITIONS

The conditions appropriate to this test are described below. These data are precise, and supersede the approximate data ranges supplied previously.

INITIAL HELIUM, AIR AND WATER VAPOUR MOLAR FRACTIONS IN THE VESSEL

Prior to the test, stratified air/helium conditions have been created in the test vessel. A helium-rich layer occupies the region $h > 5000$ mm (measured from the lowest point on the inside of the vessel, this being 11700 mm above the concrete base mat of the PANDA building), while air fills the region below this layer. The measured helium, air and water vapour molar fractions at time $t = 0$ as a function of elevation are displayed in Fig. A8. This Figure has been compiled from mass spectroscopy measurements taken

principally along the axis of the vessel. However, a number of off-axis measurements have also been included to demonstrate the degree of initial horizontal stratification. The exact locations of the data measuring points used to produce Fig. A8 are listed in Table A5. Note the near-zero concentration level of helium for $h < 5000$ mm, and the non-linear increase with height to around 0.37 helium molar fraction at elevation $h = 8000$ mm (the virtual height of the vessel in the absence of the manhole), and above into the manhole space itself (first entry in Table A5).

Care was taken to ensure that there were no residual motion of the gases in the vessel resulting from the helium injection, so at the start of the transient zero-velocity conditions prevail everywhere.

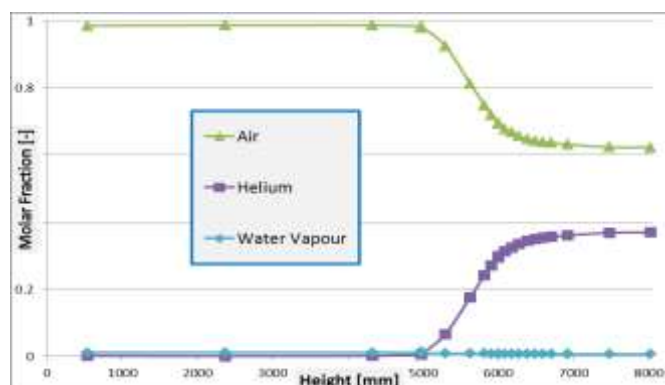


Figure A8: Initial air, helium and water vapour molar fractions as functions of height in the vessel.

Table A5: Initial air, helium and water vapour molar fractions in the vessel (as used to plot Fig. A8).

Sensor ID	x [mm]	y [mm]	z [mm]	Air [-]	Helium [-]	Water Vapour [-]
MCG_D1A_20	0	8030	0	0.623	0.37	0.007
MCG_D1B_20	0	7478	0	0.624	0.369	0.007
MCG_D1C_14	-1430	6926	0	0.632	0.361	0.007
MCG_D1C_26	1430	6926	0	0.632	0.361	0.007
MCG_D1C_20	0	6926	0	0.632	0.36	0.007
MCG_D1CD1_20	0	6706	0	0.637	0.357	0.007
MCG_D1CDA1_18	-650	6601	0	0.639	0.354	0.007
MCG_D1CD2_20	0	6496	0	0.643	0.35	0.007
MCG_D1CDA2_18	-650	6386	0	0.648	0.344	0.007
MCG_D1D_20	0	6276	0	0.657	0.335	0.007
MCG_D1DE_18	-650	6184	0	0.669	0.324	0.008
MCG_D1EF_18	-650	6092	0	0.678	0.314	0.008
MCG_D1F_20	0	6000	0	0.694	0.298	0.008
MCG_D1F_27	1690	6000	0	0.696	0.296	0.008
MCG_D1F_13	-1690	6000	0	0.696	0.295	0.008
MCG_D1FG1_18	-650	5908	0	0.72	0.272	0.008
MCG_D1FG2_18	-650	5816	0	0.75	0.241	0.009
MCG_D1G_20	0	5626	0	0.814	0.176	0.009

MCG_D1GH_18 [#]	-650	5301	0	0.925	0.067	0.009
MCG_D1H_20	0	4976	0	0.983	0.006	0.011
MCG_D1H_26	1430	4976	0	0.979	0.006	0.015
MCG_D1H_14	-1430	4976	0	0.984	0.005	0.011
MCG_D1I_20	0	4326	0	0.987	0.002	0.012
MCG_D1N_26	1430	2376	0	0.987	1.00E-03	0.012
MCG_D1N_14	-1430	2376	0	0.987	1.00E-03	0.012
MCG_D1T_20	0	538	0	0.986	0.002	0.012

[#] This entry in the Table has been obtained from one of the repetition tests under identical initialisation procedures.

For PSI reference purposes only, the designations of the sensors have also been included in Table A5. All measurements are subject to total combined uncertainties of < 0.5%.

INTERNAL GAS TEMPERATURES IN THE VESSEL

At the start of the test, stratified conditions in terms of helium/air concentration have been established in the PANDA vessel, as depicted in Fig. A8. The prevailing temperature conditions in the vessel have also been measured at the heights designated A-T (Table A6). Horizontally averaged temperatures are displayed in Fig. A9; the details in tabular form are given in the accompanying Table A6. The helium-rich layer pertains to the region $h > 5000$ mm, and is generally cooler than elsewhere in the vessel as a consequence of the helium injection process. The exception is the one temperature reading in the manhole region ($h = 8030$ mm), which is slightly warmer. The two temperature readings in Fig. A9 for $h \leq 1000$ mm (bottom of the vessel) are slightly cooler than in the bulk of the air space region. The initial temperature of the injection pipe was not measured explicitly, but was estimated to be 23°C from a nearby TC reading at $h = 1000$ mm and the injection line exit temperature at $t = 0$ given in Table 10 below.

It should be emphasised that all thermocouple measurements are subject to an error bound of ± 0.7 K.

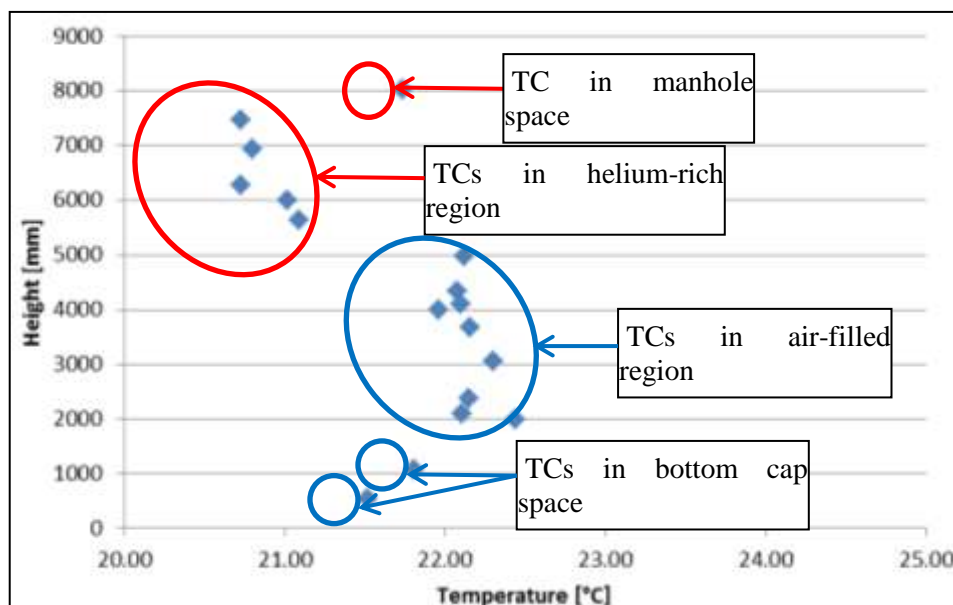


Figure A9: Measured gas temperatures in the vessel at the start of the test.

Table A6: Horizontally-averaged temperatures as a function of height in the vessel (as used to plot Fig. A9).

Level ID	Height [mm]	Temperature [°C]		Level ID	Height [mm]	Temperature [°C]
A	8030	21.74		K	4000	21.96
B	7478	20.73		L	3676	22.16
C	6926	20.80		M	3060	22.30
D	6267	20.73		N	2376	22.15
F	6000	21.02		O	2100	22.11
G	5626	21.09		R	2000	22.44
H	4976	22.12		S	1076	21.81
I	4326	22.08		T	538	21.52
J	4100	22.10				

INJECTION LINE PROPERTIES

The total mass flow rates of helium and air through the injection line have been monitored continuously during the test, and remained constant for its duration (2 hrs.); details are given in Table A7.

Table A7: Measured mass flow rates through injection line.

Gas Component	Mass Flow Rate (g/s)	Standard Dev. (g/s)	99% Confidence Level (g/s)
Helium	0.42	–	± 0.0225
Air	21.53	0.23	–

The air was drawn from that available at the pump inlet, was not dried before injection into the vessel, and consequently reflects the humidity of the atmosphere in the PANDA building at the time of the test. No measurement of the water vapour mass flow rate is available, though the molar fraction was measured just above the exit of the injection line, as indicated in Table A8.

Table A8: Molar gas fractions measured 36 mm above the injection line outlet.

Gas Component	Molar fraction [-]	Standard Dev. [-]
Helium	0.134	0.0027
Air	0.862	0.0027
Water Vapour	0.004	–

According to the experimenters, the inlet conditions indicate an average gas exit velocity of about 4.67 m/s, and a densimetric jet Froude number of about 17, confirming that the jet velocities measured just above (i.e. at the distance 7.3 mm) the outlet of the injection pipe, as described below, adequately reflect conditions at the inlet pipe exit in the core region of the jet, though care should be taken in applying these values at the level of the pipe exit, due to the jet expansion in the boundary layer region. In any case, all participants are urged to recalculate the jet parameters from the specified data summarised in Tables A7-A9.

Inlet flow temperatures have been monitored continuously during the test in the core of the inlet jet 36 mm above the inlet pipe exit (Figs. A5, A7). A plot of the measured temperatures during the test is displayed in Fig. A10, and a listing of the data points used to make the plot is given in the accompanying Table A9. The

incoming helium/air mixture was heated continuously during the test (the heater being external to the vessel), which accounts for the increase in inlet flow temperature over time.

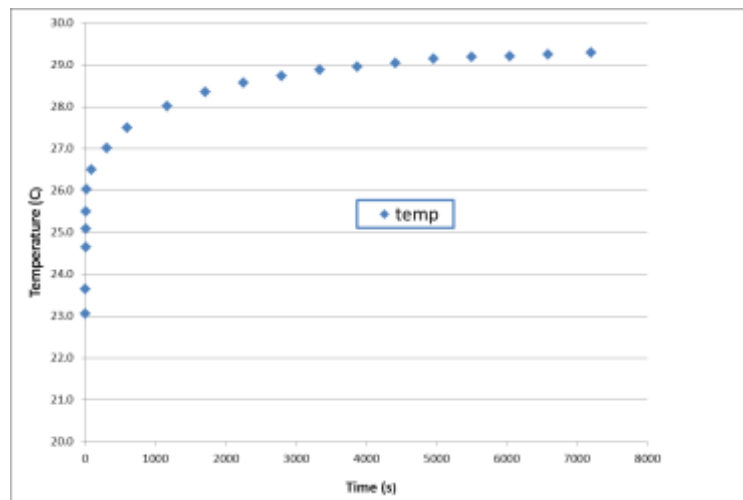


Figure A10: Measured temperature of the injected gas mixture as a function of time.

Table A9: Measured temperatures at the injection line outlet (as used to plot Fig. A10).

Time (s)	Temperature (°C)	Time (s)	Temperature (°C)	Time (s)	Temperature (°C)
0.15	23.06	306.15	27.01	3874.15	28.95
2.15	23.64	598.15	27.50	4416.15	29.04
4.15	24.64	1164.15	28.01	4958.15	29.14
6.15	25.08	1706.15	28.35	5500.15	29.18
10.15	25.50	2248.15	28.56	6042.15	29.21
16.15	26.02	2790.15	28.73	6584.15	29.25
88.15	26.50	3332.15	28.87	7200.00	29.29

The helium, air and water vapour molar fractions were likewise measured at the same distance (36 mm) above the pipe exit, as already given in Table A8, and remained constant during the test (within the specified measurement uncertainties).

WALL TEMPERATURES

From time $t = -60$ s to time $t = 0$, inner wall temperatures of the PANDA vessel, and of the inlet pipe, were measured at various locations, and an averaged value adopted to provide the start condition at $t = 0$. The temperature as a function of height is displayed in Fig. A11. Actual values are listed in Table A10, the locations of the thermocouples being given with respect to the coordinate system shown in Fig. A3.

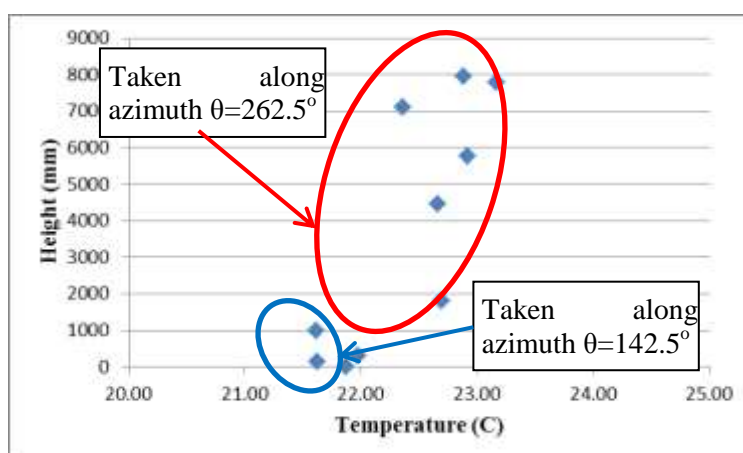


Figure A11: Measured vessel wall temperatures as a function of height.

Note that these temperatures do not always reflect conditions in the adjacent gas region (Fig. A9, Table A6), which may be a consequence of the thermal inertia of the vessel wall material. Most readings were taken along the azimuth $\theta = 262.5^\circ$, though those supplied for $h < 1000$ mm on the curved bottom cap were taken along the azimuth $\theta = 142.5^\circ$.

Again, all temperature measurements are subject to an uncertainty of ± 0.7 K.

Table A10: Measured inner wall temperatures at the start of the test (as used to plot Fig. A11).

Sensor ID	Height [mm]	Radius [mm]	Azimuth [$^\circ$]	Temperature	
				Mean [$^\circ$ C]	STD [K]
MTI.D1.18	7959	525	262.5	22.88	0.06
MTI.D1.15	7800	1361	262.5	23.17	0.05
MTI.D1.2	7100	1980	262.5	22.36	0.04
MTI.D1.12	5775	1980	262.5	22.92	0.05
MTI.D1.5	4450	1980	262.5	22.66	0.03
MTI.D1.8	1800	1980	262.5	22.70	0.04
MTI.D1.22	1000	1980	142.5	21.61	0.03
MTI.D1.23	312	1377	142.5	22.00	0.02
MTI.D1.24	153	978	142.5	21.62	0.04
MTI.D1.25	0	120	142.5	21.87	0.02

Though wall temperatures were taken along different meridians, those included here, i.e. along the meridian lines $\theta = 262.5^\circ$ and $\theta = 142.5^\circ$ (Fig. A3), are those considered most free from the distortions created by electronic noise.

VELOCITY PROFILES AT EXIT TO INJECTION LINE

PIV measurements of the instantaneous values of the Cartesian velocity components (u , v) of the gas mixture emerging from the injection pipe outlet (see Fig. A3 for coordinate frame) have been made. The PIV fields-of-view (FOVs) were taken over the pipe's internal cross-section in five horizontal planes, beginning 6 mm above the injection pipe outlet. Velocity data were assessed according to a specified

confidence level, and then combined to produce profiles in the horizontal plane 7.3 mm above the outlet; a position corresponding the closest approach to $y/D = 0.1$. A schematic of the arrangement is shown in Fig. A12.

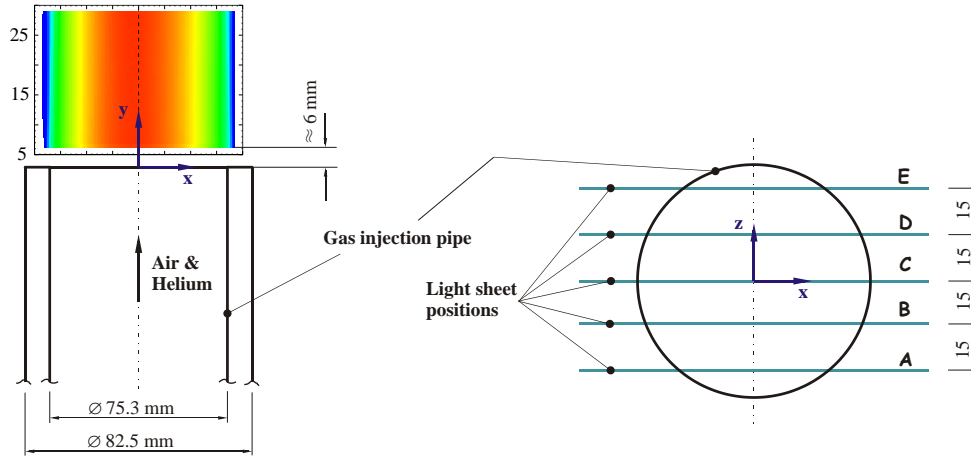


Figure A12: Relative positions of the FOVs of the PIV velocity measurements at the exit of the injection line;

note the local coordinate system used for the measurement positions A – E (Figs. A13-A17).

To gain better access, these measurements were taken with the injection line removed from the PANDA vessel, though still connected to the same helium and air supply lines used in the actual test. The laser sheet was positioned at the five (5) lines A-E, at 15 mm spacing, over the cross-section of the injection pipe outlet, as indicated in Fig. A12. The gas mixture in this case was not pre-heated; the ambient temperature was estimated at 15°C.

The profiles shown in Figs. A13-A17 show the vertical v -component (upwards in the y direction) and horizontal u -component (horizontally in the x direction). As a consequence of technical restrictions, and time constraints, it was not possible to measure the third velocity component (w -component, horizontally in the z direction). However, the assumption of axi-symmetric outlet conditions is expected to prevail in this test, though participants are free to examine this point for themselves, and precise details of the given injection line geometry have been provided for this purpose.

From the measured instantaneous velocity components u_{in} and v_{in} , mean and time averaged rms values of the pipe exit velocity data have been calculated. The procedure used was as follows:

$$\text{mean} \quad u = \frac{1}{n} \sum_{i=1}^n u_{in} \quad (1)$$

$$\text{rms} \quad u_{\text{rms}} = \sqrt{\frac{1}{n} \sum_{i=1}^n \{u_{in} - u\}^2} \quad (2)$$

Here, n is the number of instantaneous velocity recordings used in forming the average: these were taken from 4096 statistically independent samples, obtained at a sampling frequency of 7.5 Hz, which corresponds to an overall averaging time of 546 s (9.1 min.). Analogous definitions apply for the other velocity components.

A water/polyethylene-glycol mixture (10:1), dispersed into small droplets by an atomizer, was used for the seeding particles for the PIV measurements. The particles were injected into the air stream approximately 5000 mm ($\sim 60 D_H$) upstream of the injection pipe exit. The PIV camera used has a resolution of 1600×1200

pixels. For the final analysis pass, an interrogation window size of 12×12 with 50% overlap was used. This resulted in an effective spatial resolution of 6×6 pixels. After calibration of the images, a resolution of 0.088×0.088 mm²/pixel was achieved; this corresponds to an effective spatial resolution of 0.53×0.53 mm² for the velocity field.

The velocity profiles at $y = 7.3$ mm above the injection tube orifice, for each of the five (5) measurement planes A, B, C, D and E (Fig. A12), are presented in the following graphs: Figs. A13-A17. It should be noted that in the core region of the jet ($-10 \text{ mm} < x < 10 \text{ mm}$) a non-zero value for the mean lateral velocity component u has been measured for all the measurement planes. This is considered a consequence of the slightly rotated camera angle with respect to the jet axis, resulting in a ‘virtual redistribution’ of the vertical velocity in the lateral velocity direction, which should be zero in the core of the jet. If the central measurement plane C is regarded as representative ($u = 0.013$ m/s, $v = 5.35$ m/s), this would indicate a camera inclination of 0.14° . Removing this bias, the ‘true’ axial velocity would then be 5.35001 m/s. Consequently, the bias can be neglected.

Statistical error

For the statistical error estimate, reference should be made to Fig. A14. Neglecting the near-wall boundary layers, an average value for the mean axial velocity would typically be of magnitude $\bar{v} = 4.7$ m/s, with a standard deviation across the profile of around $\bar{v}_{rms} \sim 0.4$ m/s. Thus, the two-sided uncertainty, with 95% confidence level, is estimated at $\varepsilon(v) = \pm 0.0122$ m/s for the mean vertical velocity. Analogous estimates apply also for the lateral velocities, and result in $\varepsilon(u) = \varepsilon(w) = \pm 0.0092$ m/s. Since the error for the standard deviations ($v_{rms} \sim 0.4$ m/s and $u_{rms} \sim 0.3$ m/s) is non-symmetric, the two-sided uncertainty levels can be estimated as:

$$v_{rms} = 0.4^{+0.0088}_{-0.0084} \text{ m/s and } u_{rms} = 0.3^{+0.0066}_{-0.0063} \text{ m/s,}$$

Again with a confidence level of 95%.

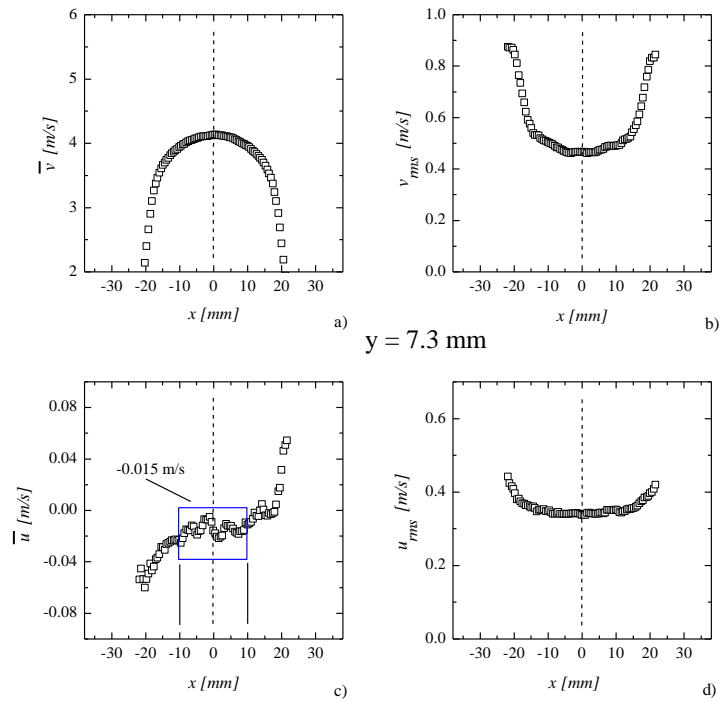


Figure A13: Mean axial v and lateral u velocity profiles (plots a and c) and the corresponding v_{rms} and u_{rms} (plots b and d) for the measurement plane A (Fig. A12) at $y = 7.3$ mm above the injection line outlet.

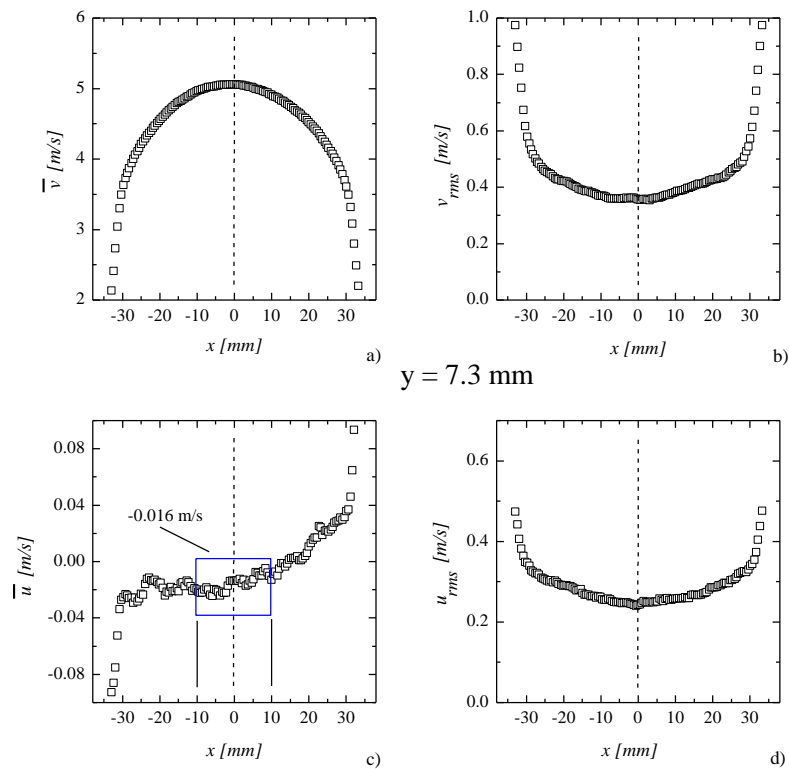


Figure A14: Mean axial v and lateral u velocity profiles (plots a and c) and the corresponding v_{rms} and u_{rms} (plots b and d) for the measurement plane B at $y = 7.3$ mm (Fig. A12) above the injection line outlet.

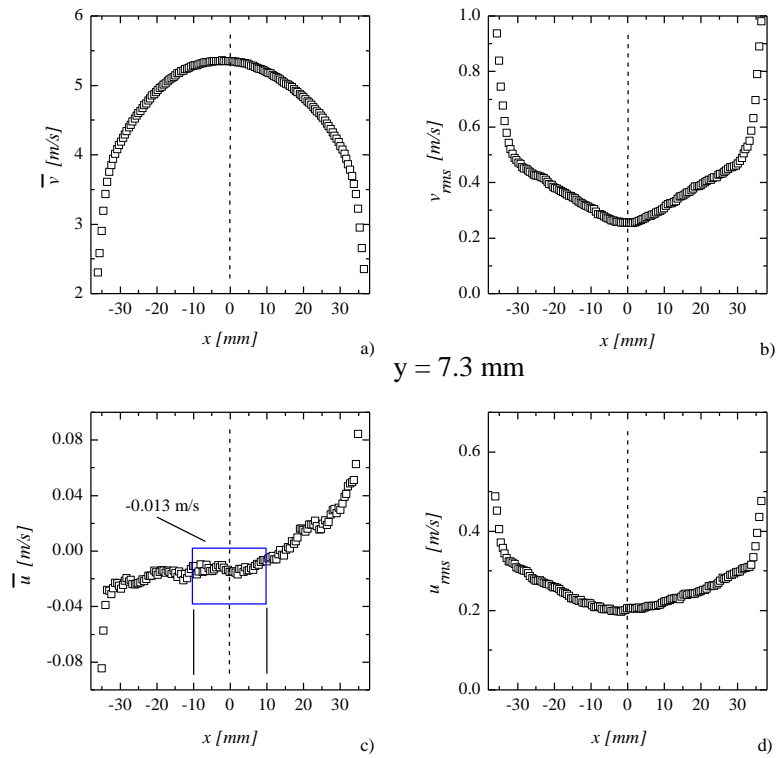


Figure A15: Mean axial v and lateral u velocity profiles (plots a and c) and the corresponding v_{rms} and u_{rms} (plots b and d) for the measurement plane C at $y = 7.3$ mm (Fig. A12) above the injection line outlet.

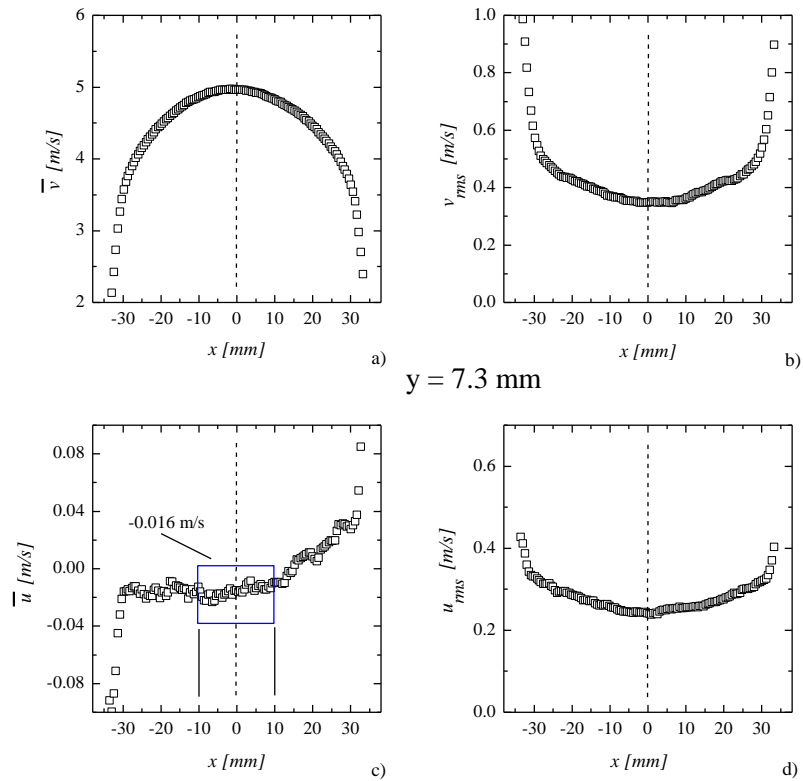


Figure A16: Mean axial v and lateral u velocity profiles (plots a and c) and the corresponding v_{rms} and u_{rms} (plots b and d) for the measurement plane D at $y = 7.3$ mm (Fig. A12) above the injection line outlet.

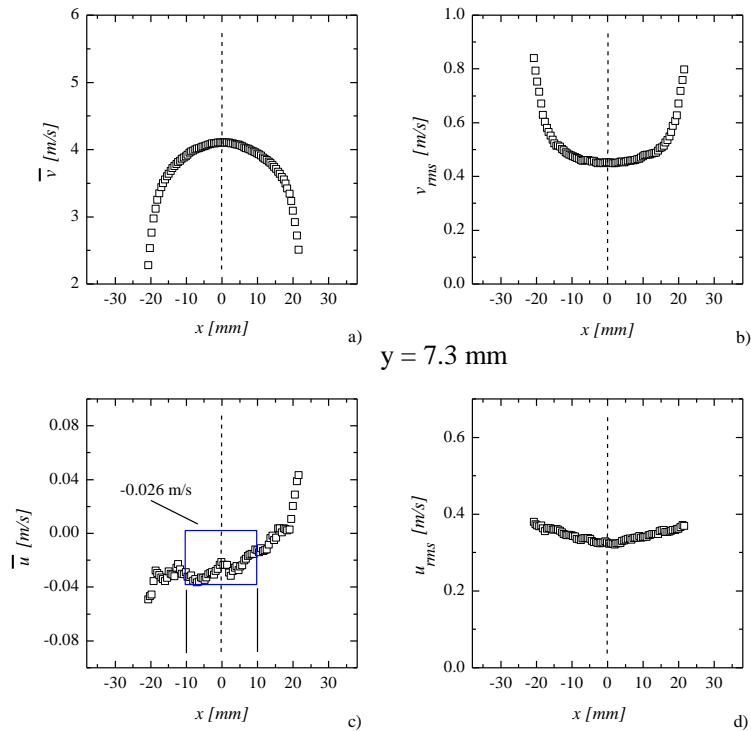


Figure A17: Mean axial v and lateral u velocity profiles (plots a and c) and the corresponding v_{rms} and u_{rms} profiles (plots b and d) for the measurement plane E at $y = 7.3$ mm (Fig. A12) above the injection line outlet.

All the data presented in Figs. A13-A17 are also available in tabular form, and are given in the Tables in the Appendix. For convenience, electronic versions are also being provided to registered participants in the form of text files to download from the PSI ftp site (N05D8posA.txt; etc.). Here, the file name depicts the measurement plane according to the local coordinate system given in Fig. A12. As mentioned above, each of these profiles has been extracted from the PIV measurements, and transposed to the horizontal plane $y = 7.3$ mm above the injection pipe orifice.

The files consist of five (5) columns: the first column contains the x coordinate (Fig. A12), the second column the mean (horizontal) x -component of velocity u , the third column the mean (vertical) y -component of velocity v , the fourth column, u_{rms} , and the fifth column v_{rms} .

A4. NUMERICAL DATA REQUESTED

A4.1 Introduction

Very basic quantities are requested from this benchmark, to permit flexibility in the choice of summary results, and uniform processing to obtain these results. Of necessity, all participants will need to pursue a transient modelling approach, and simulations are expected to produce datasets of two types: (i) time-dependent data at a fixed point location, and (ii) mean and time-averaged rms profiles along a horizontal or vertical line at specified times during the transient.

The time-dependent data are to be supplied at the specified positions (usually corresponding to the exact locations at which data have been extracted from the measurement devices), and at the time intervals specified. If the data available from the numerical simulation do not precisely coincide with the times and

spatial locations specified, the algorithms used to transfer the information to the specified times and locations are to be described (Item 12 in the list shown in Section A4.5).

In addition to the basic data, we request characterization of the CFD methodology and mesh in an accompanying document. This is to be supplied in the file Userxx_Information.doc, a template for which is provided in Section A4.5 The information requested includes: the order(s) of the numerical scheme(s); the total number of volumes used in the calculation; minimum cell edge length; maximum cell edge length; details of the turbulence model used; computer resources and calculation time; together with other quantities of interest.

A4.2 Coordinate System Used for Reporting

The Cartesian coordinate system shown in Fig. A3 is to be used throughout. The origin is at the lowest internal point of the PANDA vessel on the axis of the vessel; i.e. at an absolute height of (nominally) 11700 mm above the reference level, which is the concrete floor of the PANDA building. The positive y-axis is upwards from this point along the axis of the vessel. The x-axis is horizontal in the plane through the axis of the vessel and the centreline of the injection pipe outlet, with the positive x-direction pointing away from it (azimuthal angle 135° in Fig. A3). The z-axis is horizontal, with the positive z-direction along the azimuth $\theta = 225^\circ$ to make a right-handed (x,y,z) frame. In the following descriptions, use is made of the standard notation of (u,v,w) for the (x,y,z) components of velocity.

A4.3 Location of Instrumentation

In this benchmark, selected time-dependent measurements for temperature and molar fraction are to be made available for comparison. Additionally, the vertical component of velocity, and the rms value of this component, will also be used for the comparison between measurement and calculation at specific times along specified horizontal and vertical lines. The K-type thermocouples (TCs), each of 1.0 mm diameter (frequency response 0.5 Hz), have been placed at strategic locations in the PANDA vessel relevant to this test, many in the jet plume issuing from the injection pipe. Temperature measurements have been taken at 218 locations, though only selected temperature data are requested here. The estimated uncertainty in the location coordinates for each TC is ± 5.0 mm in each coordinate direction, and that for the temperature measurement is ± 0.7 K.

TEMPERATURE DATA

Transient temperatures (in $^\circ\text{C}$) shall be reported at the five (5) specified thermocouple locations listed in Table A11. The format for submitting these data are described Section A4.4.

Table A11. Locations at which transient temperature data are requested.

TC Number	x (mm)	y (mm)	z (mm)	TC ID
TC_1	-650.0	7478.0	0.0	B_18
TC_2	-650.0	4326.0	0.0	I_18
TC_3	-650.0	3676.0	0.0	L_18
TC_4	-650.0	3036.0	0.0	M_18
TC_5	-325.0	3676.0	0.0	L_19

MASS SPECTROMETRY DATA

In this test, two mass spectrometry (MS) instruments have been utilized. The first (MS1) measures the helium, air and water vapour molar fractions at the inlet (MCG_D1X), as already given in Table A8, and the same quantities at the outlet to the PANDA vessel (MCG_D2V0_1). The sampling period for these two lines is 30 s. The second instrument (MS2) monitors these same quantities at 30 other locations in the vessel. The sampling period for these lines is 226 s. Each of the sampling lines is of 0.8 mm internal diameter and 1.0 mm external diameter. Data at nineteen (19) sampling lines, designated MS_1 to MS_19, are requested for this benchmark, as itemized in Table A12. The estimated uncertainty in the location coordinates for each sampling point is ± 5 mm in each coordinate direction, and, as stated earlier, that for the He molar fraction is at most 0.5% absolute.

The method of data acquisition is outlined below, and reflects the times at which the data are being requested. The first eight (8) sampling locations (Table A12) lie along the axis of the incoming jet ($x = -650$ mm; $z = 0$). Others are located along the axis of the vessel ($x = 0$, $z = 0$), while the remainder are at other positions of interest.

The start time for each data item directly reflects the measurement procedure. For the mass spectrometer MS2, each of the 30 sampling lines is traversed in turn. Generally, the scanning time is 7 s, of which data for the final 5 s (for which stable conditions have been established) are averaged to produce the gas concentration measurement at the designated time: i.e. $2 + 2.5 = 4.5$ s from the start of the scan. This is the reason for the sub-second entries in Column 6 of Table A12. The procedure is repeated for the remaining 29 sample lines attached to this instrument (for two of the lines the scanning time is 15 s rather than 7 s). It takes 226 s to traverse all of the 30 sampling lines, at which time the measurements are repeated, consecutively, from the first sampling line onwards. This measurement period is reflected in Column 7 of Table A12 for lines MS_1 to MS_18. The last entry in Table A12 (MS_19) refers to one of the two sampling lines attached to the other mass spectrometer, for which the scanning time is 15 s, and the period of the measurements is consequently 30s instead.

Table A12. Details of the transient He molar fractions to be supplied.

MS Number	x (mm)	y (mm)	z (mm)	ID	Start time (s)	Period (s)
MS_1	-650	7478	0.0	B_18	77.1	226
MS_2	-650	6706	0.0	CD1_18	90.8	226
MS_3	-650	6184	0.0	DE_18	125.6	226
MS_4	-650	6000	0.0	F_18	146.6	226
MS_5	-650	5908	0.0	FG1_18	175.2	226
MS_6	-650	4976	0.0	H_18	202.5	226
MS_7	-650	3676	0.0	L_18	20.4	226
MS_8	-650	3036	0.0	M_18	215.6	226
MS_9	0.0	8030	0.0	A_20	70	226
MS_10	0.0	6000	0.0	F_20	153.9	226
MS_11	650	6000	0.0	F_22	161	226
MS_12	1690	6000	0.0	F_27	167.8	226
MS_13	-1430	3676	0.0	L_14	13.3	226
MS_14	650	3676	0.0	L_22	27.3	226
MS_15	1430	3676	0.0	L_26	34.2	226

MS_16	-1430	3036	0.0	M_14	42.1	226
MS_17	-1430	1076	0.0	S_14	49	226
MS_18	1430	1076	0.0	S_26	55.8	226
MS_19 [#]	0.0	160	0.0	D2V0_1	8.5	30

[#] For convenience, the data for MS_19 are to be given at the coordinates shown (the entrance to the flexible blue hose, Fig. A6), at the times specified. In fact, the sensor was physically located at the other end of the hose, and the organisers will be applying the appropriate time delay factor when comparing with the experimental data.

The molar fractions are to be presented according to the following definitions. The molar fraction x_A of component gas A of a mixture of gases of component parts A, B, C in a given volume (i.e. a discrete control volume) is:

$$x_A = \frac{m_A / \mu_A}{m_A / \mu_A + m_B / \mu_B + m_C / \mu_C} \quad (3)$$

in which m_A is the mass of component A , molecular weight μ_A , in the given volume; likewise for the other components. For helium, air and water vapour, the following molecular weights may be used for guidance purposes:

$$\mu_{\text{He}} = 4.0; \quad \mu_{\text{air}} = 29.0; \quad \mu_{\text{H}_2\text{O}} = 18.0; \quad (\text{g/mol})$$

though more precise values are available from the NIST database <http://webbook.nist.gov/chemistry/>, if desired.

The number of requested time-histories has been limited for purely practical reasons. However, the progression of the global de-stratification process is the most important phenomenon addressed in this benchmark, and all information generated for the time evolution of the erosion process along the axis of the injection pipe will be used for evaluating the capabilities of the calculations to follow this process. It is therefore requested to provide the times at which, at each elevation, the helium molar fraction drops below a threshold value, which is arbitrarily fixed at 0.2 (20%).

Table A13 lists the elevations along the axis of the injection for which the times the helium concentration drops below this value (0.2) should be provided. Note that this variable has to be carefully evaluated, because it will have a high impact on the subsequent ranking process for this benchmark.

Table A13: Heights along the injection pipe exit line ($x = -650$ mm; $z = 0$) for which the time the helium molar fraction drops below the threshold value of 0.2 (file *HeDrop.txt*, Section A4.4).

y (mm)	Sensor ID
6000	F_18
6092	EF_18
6184	DE_18
6276	D_18
6386	CDA2_18
6496	CD2_18
6601	CDA1_18
6706	CD1_18
6926	C_18
7478	B_18

VELOCITY DATA

Velocities and velocity fluctuations have been measured using PIV in three regions of the flow, all above and around the axis of the injection pipe. These measurements have been processed to produce averaged values over a time period of 204.6 s. The measured data that will be compared against the CFD predictions will refer to the time in the middle of this data averaging period; i.e. ± 102.3 s around each specified data item.

Table A14: Location of horizontal lines for which the mean vertical velocity component \bar{v} and the averaged rms of this component \bar{v}' are requested (file *HVy_1.txt*, etc., Section A4.4).

Horizontal profile	Time (s)	y (mm)	$x1 < x < x2$ (mm)		Δx (mm)	Number of points
HVy_1	111	5100.3	-1271.5	-127.2	11.44	101
HVy_2	715	5904.1	-1213.5	-149.8	10.33	104
HVy_3	1213	5904.1	-1213.5	-149.8	10.33	104
HVy_4	715	6110.6	-1213.5	-149.8	10.33	104
HVy_5	1795	6447.2	-1196.1	-233	9.93	98
HVy_6	2550	6447.2	-1196.1	-233	9.93	98
HVy_7	2550	6606.1	-1196.1	-233	9.93	98
HVyRMS_1	111	5100.3	-1271.5	-127.2	11.44	101
HVyRMS_2	715	5904.1	-1213.5	-149.8	10.33	104
HVyRMS_3	1213	5904.1	-1213.5	-149.8	10.33	104
HVyRMS_4	715	6110.6	-1213.5	-149.8	10.33	104
HVyRMS_5	1795	6447.2	-1196.1	-233	9.93	98
HVyRMS_6	2550	6447.2	-1196.1	-233	9.93	98
HVyRMS_7	2550	6606.1	-1196.1	-233	9.93	98

The distributions of the mean vertical velocity component \bar{v} at the specified times, and the averaged rms value of this component \bar{v}'_{rms} at the same time, are requested at the given times along horizontal lines spanning the spatial distance $x1$ to $x2$, as defined in Table A14. The number of the points requested for each profile has been determined from the available PIV data obtained during the test, and these will be used in the ranking process. If numerical data are not available at the precise times and positions specified in Table A14, the method of interpolation is to be described (see Section A4.5).

In addition to the horizontal profiles, the vertical distribution of the same variables (mean vertical component of velocity \bar{v} , and the averaged rms of this component \bar{v}'_{rms}), as well as the turbulent kinetic energy \bar{k}_{TKE} , are requested along the axis of the injection pipe ($x = -650$ mm; $z = 0$; $y1 < y < y2$), as specified in Tables A15, A16. The vertical distribution will be compared with the experimental values within the elevations $y1$ to $y2$ specified in Table A15, for which also the spacing of the measurement points, Δy , is given. If the mesh description does not provide data at these exact points, interpolated values are to be provided, and the interpolation algorithm by which they were obtained is to be described (see Section 4.5).

Table A15: Times for which the mean vertical velocity component, \bar{v} , and the averaged rms of this component, \bar{v}' , along the injection axis ($x = -650$ mm; $z = 0$; $y1 < y < y2$) are requested.

Vertical profile	Time (s)	$y1 < y < y2$ (mm)		Δy (mm)	Number of points
VVy_1	111	5008.7	5615.2	11.44	54
VVy_2	1213	5635.6	6255.2	10.33	61
VVy_3	250	6268.5	6894	9.93	64
VVyRMS_1	111	5008.7	5615.2	11.44	54
VVyRMS_2	1213	5635.6	6255.2	10.33	61
VVyRMS_3	250 [±]	6268.5	6894	9.93	64

[±] N.B. This was a typing error, later corrected. The correct value is 2550.

The vertical distribution of turbulent kinetic energy, \bar{k}_{TKE} , will not be used as part of the formal ranking process, but will be evaluated during the synthesis with respect to overall consistency.

Table A16: Times for which the mean turbulent kinetic energy \bar{k}_{TKE} along the injection axis ($x = -650$ mm; $z = 0$; 3000 mm $< y < 7500$ mm) are requested.

Vertical profile	Time (s)	Δy (mm)	Number of points
TKE_1	111	30	151
TKE_2	1213	30	151
TKE_3	250	30	151

The mean axial velocity \bar{v} data referred to in Tables A14, A15 are to be given in physical units (m/s); the same also for the averaged axial rms value, \bar{v}' (m/s). In addition, the mean turbulent kinetic energy, \bar{k}_{TKE} , referred to in Table A16, shall be reported in units of m^2/s^2 .

A4.4 Data File Formats

All files shall be written in ASCII text format, with space-delimited fields. For the files describing the temperature data, the file name shall read *TC_1.txt* for the first thermocouple measurement TC_1 in Table A11, *TC_2.txt* for the second thermocouple measurement TC_2 in Table A11, and so on till *TC_5.txt* for the 5th thermocouple measurement. The first row of the file shall contain the user identification number, as supplied by michele.andreani@psi.ch, in ASCII format, followed by the total number of data lines that follow (max. 241). For the succeeding rows, the first column shall contain the time of the measurement in seconds to one decimal place, starting from time $t = 0$, in intervals of 30 s: i.e. 0.0, 30.0, 60.0, etc. The second column shall contain the temperature T written to 2 decimal places at these times; e.g. 20.75, 21.06, 21.59, etc. The number of rows of data shall equal the number in the second column of the first row.

A first temperature file could thus look like the following:

TC_1.txt

User01	241
0.0	20.75
30.0	21.06
60.0	21.59
.....
7200.0	23.84

and subsequent files *TC_2.txt* to *TC_5.txt* likewise.

An analogous procedure is to be followed for the helium molar fraction data. That is, all files shall be written in ASCII text format, with space-delimited fields. The file name shall read *MS_1.txt* for the first mass spectrometer measurement MS_1 in Table A12, *MS_2.txt* for the second mass spectrometer measurement MS_2 in Table A12, and so on till *MS_19.txt* for the 19th mass spectrometer measurement in Table A12. The first row of the file shall contain the user identification number, in ASCII format, followed by the total number of data lines that follow: e.g. for file *MS_1.txt*, the first line could read User01 32. For the succeeding rows, the first column shall contain the time of the measurement in seconds to one decimal place, beginning with 0.0, continuing with the start time shown in Table A12, and repeating at the specified interval of 226 s: i.e. 0.0, 77.1, 303.1, etc. The second column shall contain the helium molar fraction x_{He} (Eq. 4) written to 3 decimal places; e.g. 0.369, 0.344, 0.305, etc. The number of rows of data shall equal the number in the second column of the first row.

The first helium molar fraction file (*MS_1.txt*) might thus look like the following (ref. Tables A5, A12):

```

MS_1.txt
User01 32
0.0 0.369
77.1 0.344
303.1 0.305
...
7083.1 0.008

```

The second helium molar fraction file (*MS_2.txt*) might thus look like the following (ref. Tables A5, A12):

```

MS_2.txt
User01 32
0.0 0.357
90.8 0.334
316.8 0.319
...
7096.8 0.086

```

The subsequent files *MS_3.txt* to *MS_19.txt* are to be assembled likewise.

The helium concentration drop file will look like the following (elevation vs. time, 10 pairs of entries). For example:

```

HeDrop.txt
User01      10
6000        100
6092        150
6184        300
6276        1500
6386        5000
6496        6000
6601        6500
6706        6800
6926        7000
7478        7200

```

in which the first column is the height (mm) requested in Table A13, and the second column the time (s) at which the helium molar fraction (Eqn. 3) drops to the level of 0.2.

Following the same formatting style, a typical horizontal distribution of the vertical mean velocity component \bar{v} (Table A14) might look like the following:

```

HVy_1.txt
User01      101
-1271.5     2.95
-1260.0     3.12
...
-127.2      2.64

```

and a typical horizontal distribution of the mean rms of the vertical velocity component \bar{v}_{rms} (Table A14) might look like the following:

```

HVyRMS_2.txt
User01      104
-1213.5     0.23
-1063.7     0.28
...
-149.8      0.34

```

A typical vertical velocity distribution of the vertical mean velocity component \bar{v} (Table A15) might look like the following:

```

VVy_1.txt
User01      54
5008.7      4.67
5020.1      4.36
5031.6      4.14
...
5615.2      3.75

```

and a typical vertical distribution of the mean rms of the vertical velocity component \bar{v}_{rms} (Table A15) might look like the following:

```

VVyRMS_2.txt
User01      61
5635.6      0.27
5645.9      0.33
...
6255.2      0.23

```

The structure of the files containing the TKE values (Table A16) should be similarly constructed to those for the velocities. Thus, for the first profile, TKE_1, the file could be as follows:

```

TKE_1.txt
User01      151
3000.0      0.58

```

3030.0	0.73
...	...
7500.0	0.64

A4.5 Basic Information of Numerical Model and Method of Solution

We request the following information concerning the physical/numerical solution procedure:

1. Code used, including version number;
2. Total number of control volumes employed;
3. Minimum and maximum cell lengths (expressed in m) for non-wall cells (e.g. 0.01 0.05)
4. Time step (maximum, minimum, average);
5. Order of the spatial differencing scheme and type (e.g. 2nd-order upwind);
6. Order of the time differencing scheme and type (e.g. 1st-order implicit);
7. Convergence criterion within a time step (e.g. non-iterative, mass residual = x kg/s, other);
8. Air/helium molecular diffusivity coefficient
9. Turbulence model (e.g. none, standard k- ϵ , LES (Smagorinsky), etc.) ;
10. Wall treatment (e.g. wall-resolved, wall functions, van Driest damping, etc.);
11. Turbulent Schmidt number;
12. Interpolation algorithms used to move numerical time/space data to specified intervals/locations.
13. Computer type and model details (including clock speed);
14. Arithmetic precision (e.g. 64-bit);
15. Number of cores used;
16. Total simulation time in s (e.g. 7200);
17. Total CPU time required in hrs (e.g. 720);
18. Equivalent total CPU time for one core in hrs (e.g. 1440).

This information is to be supplied in the form of a Microsoft .doc file, named *Userxx_Information.doc* (or *Userxx_Information.docx*), in which *Userxx* is the username allocated to you by [Michele Andreani](#) on the PSI ftp site. The first line of the file shall contain a space-delimited list of the authors involved in the study. The second line shall contain the name of the parent organization. The third line shall contain your username. Subsequent lines shall contain the information requested above. An example is given here, which is to be used as a template for the information you provide.

B.Smith G.Zigh D.Bestion		
OECD/NEA Paris France		
Userxx		
Item #	Item description	Information supplied
1.	Code used, including version number	ANSYS Fluent, version 12.4
2.	Total number of control volumes employed	146302
3.	Minimum and maximum cell lengths (expressed in m) for non-wall cells	0.01 0.05
...
18.	Equivalent total CPU time for one core in hrs (e.g. 1440).	720

A6. CONCLUDING REMARKS

A6.1 Organizing Committee

Brian L. Smith, Paul Scherrer Institute,	Switzerland
Domenico Paladino*, Paul Scherrer Institute,	Switzerland
Dominique Bestion, Commissariat à l'Énergie Atomique,	France
Ghani Zigh, US Nuclear Regulatory Commission,	USA
Michele Andreani, Paul Scherrer Institute,	Switzerland
Abdallah Amri ^{&} , OECD Nuclear Energy Agency,	France (Secretariat)

* Withdrawn

[&] Replaced by M.P. Kissane

A6.2 Schedule

April 25, 2013	Kick-Off Meeting
May 31, 2013	Distribution of Benchmark Specifications (Geometry)
July 31, 2013	Distribution of Benchmark Specifications (Geometry + Flow Parameters)
Aug. 15, 2013	Deadline for receipt of comments/queries to Benchmark Specifications
Aug. 22, 2013	Issue of Final Benchmark Specifications
May 30, 2014	Deadline for Receipt of Simulation Results (WILL NOT BE EXTENDED)
June 15, 2014	Latest Date for Open Benchmark Meeting and Opening of Test Data
Sept. 30, 2014	Latest Date for Presentation of Benchmark Synthesis at CFD4NRS-5 Workshop

A preliminary version of the benchmark specifications is to be distributed on July 31, 2013. Participants are requested to communicate any queries/comments within 15 days. The inquiries made by participants are to be addressed by the benchmark organisers, and clarifications embodied into the final version of this document. The participants then have about 9½ months to perform the simulations and to submit their results to the organisers in the specified formats for evaluation.

This benchmark activity is an integral part of the CFD4NRS-5 Workshop, and the scheduling is part due to the timing of this event in the autumn of 2014. However, it is intended to release the data ahead of this time to enable participants to assess, and perhaps build on, their *blind* numerical predictions. Consequently, an Open Benchmark Meeting, to take place in Paris, will be organized in early June 2014, at which time the measured transient data will be opened for the first time.

The synthesis of the blind benchmark results will be undertaken by a PSI staff member, who will present his findings in the form of an Invited Lecture at the CFD4NRS-5 Workshop, to take place in Switzerland in September 2014. The Workshop will be under joint OECD/NEA and IAEA sponsorship. A paper will also be prepared to accompany the Benchmark Synthesis Lecture, and will be part of the official conference proceedings to be issued by the OECD/NEA during 2015.

It is hoped that many participants will take the opportunity to display their results at this Workshop, and a special Poster Session will be organised for this purpose. **It will not be necessary to produce an accompanying paper in support of this poster.** On the afternoon of the last day of the Workshop, a visit to the PANDA facility will be organised for those interested.

If considerably more numerical work than requested for the blind benchmark has been undertaken, for example a comparison of several turbulence modelling approaches, sensitivity studies, etc., a full paper can be submitted to the Workshop in the usual way for consideration for inclusion in the technical programme. The number of such papers will be restricted, however.

A6.3 Submittal Procedures

In order to be able to efficiently handle and compare calculated and measured data, all participants are requested to adhere STRICTLY to the formatting requested in Section A4 of this document. Datasets not conforming to the specified norms will be returned to participants for correction. As an aid to submission, a script (most likely written in Python, www.python.org) will be issued to all participants. It is a requirement of all participants that their data sets can be read by the script prior to their submission to the organisers in order to verify data compatibility. Failure to do this may result in the deletion of the submitted data from the set chosen for synthesis.

The deadline for submission of code predictions is set for May 30, 2014. Earlier submissions will be very welcome, and will considerably ease the burden on the organisers. Later submissions will be accepted or refused at the discretion of the organizing committee, but only up to the time the data are opened. **Only one submission per registered participant will be accepted.**

A special *Dropbox* will be created on the PSI ftp site to which participants will be able to upload their results. Details will be distributed once the webpage is functional. Individual usernames and passwords will be allocated by the site manager (michele.andreani@psi.ch), and all data sets will be regarded as confidential. Unrestricted access to the data will only be available to the benchmark organisers. After uploading, participants are advised to download their datasets and compare with the originals to ensure that perfect transmission has been accomplished. Each participant will have the opportunity to exchange the datasets submitted for newer versions, but only up to the time of the deadline (May 30, 2014) at which time no further access to the *Dropbox* will be possible. After the test data are opened at the Open Benchmark Meeting in June 2014 (actual date to be announced), no further submissions will be accepted. Additionally, participants will thereafter not be permitted to withdraw their submissions.

Participants are free to repeat their calculations once they have the test data, and display any new results at the special Poster Session at the CFD4NRS-5 Workshop, as desired. However, only the *blind* code predictions will be considered for the synthesis.

A7. LIST OF ATTACHMENTS REFERENCED IN THE TEXT AND AVAILABLE ON THE FTP SITE

- [At1] Overview of Vessel Arrangement, Giovanola Drawing No. 164A3526-1c
(Zusammenstellung: 1-290111c)
- [At2] Dry-Well Vessels, Giovanola Drawing No. 164A3526-2I
(DRY-WELL Behälter: 0-290112I)
- [At3] Vessel Internals, Giovanola Drawing No. 164A3526-10f
(Einbauten: 0-290120)
- [At4] Manhole DN 700, Giovanola Drawing No. 164A3526-7b
(Mannloch DN 700: 2-290117)
- [At5] Manhole DN 1000, Giovanola Drawing No. 164A3526-8b
(Mannloch DN 1000: 2-290118)

[N05D8posA.txt] Data points used to produce the profile along the measurement line A in Figure A12.

[N05D8posB.txt] Data points used to produce the profile along the measurement line B in Figure A12.

[N05D8posC.txt] Data points used to produce the profile along the measurement line C in Figure A12.

[N05D8posD.txt] Data points used to produce the profile along the measurement line D in Figure A12.

[N05D8posE.txt] Data points used to produce the profile along the measurement line E in Figure A12.

A8. TABLES OF MEASURED INJECTION LINE VELOCITY PROFILES

Data points used to produce the profiles in Figure A13, along the measurement line A in Figure A12. These data are also available on the PSI ftp site under the name *N05D8posA.txt*.

The columns signify, from left to right: x [mm]; u_{mean} [m/s]; v_{mean} [m/s]; u_{rms} [m/s]; v_{rms} [m/s]

-21.8	-0.05391.4900	0.4420	0.8750	-6.4	-0.01174.0500	0.3410	0.4780
-21.3	-0.04521.6800	0.4240	0.8710	-5.9	-0.01284.0600	0.3400	0.4740
-20.7	-0.05361.9000	0.4160	0.8710	-5.4	-0.01734.0700	0.3400	0.4700
-20.2	-0.06002.1400	0.4080	0.8620	-4.8	-0.01894.0800	0.3410	0.4670
-19.7	-0.05362.4000	0.3970	0.8450	-4.3	-0.01624.0900	0.3410	0.4630
-19.2	-0.04932.6600	0.3800	0.8110	-3.8	-0.01584.1000	0.3410	0.4620
-18.6	-0.04152.9000	0.3820	0.7650	-3.3	-0.01174.1000	0.3420	0.4610
-18.1	-0.04683.1000	0.3740	0.7340	-2.7	-0.00684.1100	0.3420	0.4660
-17.6	-0.04393.2600	0.3690	0.6930	-2.2	-0.00734.1100	0.3420	0.4650
-17.0	-0.03813.3700	0.3680	0.6580	-1.7	-0.00714.1100	0.3430	0.4650
-16.5	-0.03693.4600	0.3640	0.6220	-1.1	-0.00524.1200	0.3420	0.4670
-16.0	-0.03423.5400	0.3640	0.5910	-0.6	-0.00924.1200	0.3410	0.4670
-15.4	-0.02833.6100	0.3610	0.5760	-0.1	-0.01564.1300	0.3370	0.4660
-14.9	-0.02873.6600	0.3570	0.5590	0.4	-0.01774.1300	0.3370	0.4670
-14.4	-0.03093.7000	0.3610	0.5390	1.0	-0.02064.1300	0.3370	0.4630
-13.9	-0.02623.7400	0.3560	0.5320	1.5	-0.02194.1200	0.3430	0.4610
-13.3	-0.02543.7700	0.3470	0.5310	2.0	-0.02064.1200	0.3440	0.4650
-12.8	-0.02463.8100	0.3510	0.5300	2.6	-0.01964.1200	0.3420	0.4640
-12.3	-0.02323.8400	0.3520	0.5200	3.1	-0.01384.1100	0.3420	0.4650
-11.7	-0.02353.8700	0.3510	0.5150	3.6	-0.01054.1100	0.3400	0.4630
-11.2	-0.02283.8900	0.3530	0.5110	4.2	-0.01204.1000	0.3400	0.4650
-10.7	-0.02363.9100	0.3480	0.5090	4.7	-0.01214.0900	0.3400	0.4700
-10.1	-0.02293.9400	0.3470	0.5040	5.2	-0.01224.0900	0.3440	0.4750
-9.6	-0.02543.9600	0.3500	0.5010	5.7	-0.01434.0800	0.3440	0.4740
-9.1	-0.02193.9800	0.3450	0.4980	6.3	-0.01654.0600	0.3420	0.4780
-8.6	-0.01783.9900	0.3400	0.4950	6.8	-0.01754.0500	0.3440	0.4850
-8.0	-0.01484.0100	0.3410	0.4900	7.3	-0.01854.0300	0.3510	0.4870
-7.5	-0.01534.0300	0.3430	0.4830	7.9	-0.01624.0200	0.3510	0.4890
-7.0	-0.01574.0400	0.3460	0.4830	8.4	-0.01624.0000	0.3510	0.4910

8.9	-0.01543.9900	0.3510	0.4890
9.4	-0.00953.9700	0.3500	0.4890
10.0	-0.01133.9600	0.3520	0.4890
10.5	-0.01023.9400	0.3500	0.4920
11.0	-0.00903.9100	0.3450	0.4930
11.6	-0.00673.8800	0.3440	0.5000
12.1	-0.00193.8600	0.3470	0.5110
12.6	-0.00413.8300	0.3480	0.5150
13.2	-0.00453.8000	0.3520	0.5170
13.7	-2.7E-53.7700	0.3540	0.5210
14.2	0.0048 3.7400	0.3530	0.5260
14.7	5.12E-4 3.7000	0.3550	0.5420
15.3	-0.00403.6500	0.3560	0.5550
15.8	-0.00433.5900	0.3600	0.5700
16.3	-0.00203.5300	0.3630	0.5850
16.9	-0.00293.4600	0.3690	0.6120
17.4	-0.00223.3700	0.3740	0.6440
17.9	-0.00123.2400	0.3780	0.6760
18.4	0.0044 3.1000	0.3850	0.7180
19.0	0.0147 2.9100	0.3860	0.7580
19.5	0.0176 2.6900	0.3890	0.7850
20.0	0.0313 2.4400	0.3970	0.8180
20.6	0.0463 2.1900	0.4000	0.8320
21.1	0.0508 1.9400	0.4080	0.8330
21.6	0.0545 1.7300	0.4200	0.8440

Data points used to produce the profiles in Figure A14, along the measurement line B in Figure A12. These data are also available on the PSI ftp site under the name *N05D8posB.txt*.

The columns signify, from left to right: x [mm]; u_{mean} [m/s]; v_{mean} [m/s]; u_{rms} [m/s]; v_{rms} [m/s]

-32.90	-0.09282.1300	0.4740	0.9750	-14.40	-0.01574.8200	0.2670	0.3870
-32.40	-0.08622.4100	0.4420	0.8980	-13.90	-0.01484.8400	0.2680	0.3850
-31.90	-0.07522.7300	0.4060	0.8240	-13.30	-0.01744.8600	0.2670	0.3870
-31.30	-0.05273.0400	0.3820	0.7530	-12.80	-0.01354.8800	0.2630	0.3820
-30.80	-0.03373.3000	0.3640	0.6730	-12.30	-0.01474.8900	0.2640	0.3800
-30.30	-0.02723.4900	0.3490	0.6160	-11.70	-0.01744.9100	0.2640	0.3770
-29.70	-0.02543.6300	0.3470	0.5790	-11.20	-0.02084.9300	0.2600	0.3750
-29.20	-0.02333.7300	0.3390	0.5540	-10.70	-0.01914.9400	0.2630	0.3700
-28.70	-0.02423.8000	0.3280	0.5330	-10.10	-0.01994.9600	0.2620	0.3690
-28.20	-0.02603.8700	0.3250	0.5160	-9.62	-0.02134.9700	0.2560	0.3700
-27.60	-0.02583.9400	0.3200	0.5010	-9.09	-0.02244.9800	0.2550	0.3680
-27.10	-0.02934.0000	0.3210	0.4900	-8.56	-0.02214.9900	0.2550	0.3660
-26.60	-0.02574.0600	0.3170	0.4840	-8.03	-0.01985.0000	0.2580	0.3610
-26.00	-0.02844.1100	0.3100	0.4720	-7.50	-0.01855.0100	0.2560	0.3590
-25.50	-0.02634.1600	0.3080	0.4630	-6.97	-0.02005.0200	0.2520	0.3600
-25.00	-0.02304.2100	0.3060	0.4570	-6.44	-0.02375.0200	0.2500	0.3600
-24.40	-0.02374.2500	0.3020	0.4530	-5.91	-0.02465.0300	0.2490	0.3590
-23.90	-0.01594.2900	0.3000	0.4490	-5.38	-0.01975.0300	0.2500	0.3590
-23.40	-0.01254.3300	0.3030	0.4460	-4.85	-0.02015.0400	0.2490	0.3590
-22.90	-0.01164.3700	0.2980	0.4380	-4.32	-0.02155.0400	0.2460	0.3580
-22.30	-0.01324.4000	0.3020	0.4320	-3.80	-0.02425.0500	0.2470	0.3610
-21.80	-0.01394.4400	0.2980	0.4280	-3.27	-0.02155.0500	0.2480	0.3630
-21.30	-0.01314.4700	0.2940	0.4270	-2.74	-0.02255.0500	0.2470	0.3590
-20.70	-0.01444.5100	0.2920	0.4230	-2.21	-0.02215.0500	0.2450	0.3610
-20.20	-0.01634.5400	0.2900	0.4210	-1.68	-0.01715.0500	0.2440	0.3620
-19.70	-0.01524.5700	0.2910	0.4210	-1.15	-0.01405.0600	0.2420	0.3620
-19.20	-0.01874.6000	0.2910	0.4200	-0.62	-0.01375.0600	0.2400	0.3600
-18.60	-0.02434.6300	0.2890	0.4150	-0.09	-0.01395.0600	0.2420	0.3560
-18.10	-0.02154.6600	0.2890	0.4110	0.44	-0.01355.0600	0.2430	0.3550
-17.60	-0.02224.6900	0.2850	0.4070	0.97	-0.01355.0500	0.2470	0.3550
-17.00	-0.01814.7100	0.2820	0.4040	1.50	-0.01255.0500	0.2520	0.3580
-16.50	-0.02114.7400	0.2780	0.4010	2.03	-0.01555.0500	0.2490	0.3580
-16.00	-0.02084.7600	0.2790	0.3950	2.56	-0.01305.0400	0.2480	0.3550
-15.40	-0.01914.7900	0.2810	0.3910	3.09	-0.01725.0400	0.2480	0.3540
-14.90	-0.02104.8100	0.2720	0.3900	3.62	-0.01625.0300	0.2510	0.3590

4.15	-0.01355.0200	0.2480	0.3600	24.80	0.0221	4.2000	0.3030	0.4560
4.68	-0.01505.0200	0.2510	0.3630	25.30	0.0211	4.1600	0.3050	0.4630
5.21	-0.01275.0100	0.2510	0.3630	25.90	0.0226	4.1100	0.3070	0.4690
5.74	-0.00774.9900	0.2580	0.3630	26.40	0.0246	4.0700	0.3110	0.4720
6.27	-0.00824.9900	0.2550	0.3660	26.90	0.0276	4.0200	0.3190	0.4800
6.80	-0.00994.9800	0.2520	0.3680	27.40	0.0284	3.9700	0.3210	0.4870
7.33	-0.00994.9700	0.2570	0.3720	28.00	0.0290	3.9100	0.3250	0.4910
7.86	-0.00694.9600	0.2590	0.3730	28.50	0.0310	3.8500	0.3260	0.5080
8.38	-0.00494.9500	0.2550	0.3730	29.00	0.0297	3.7800	0.3240	0.5270
8.91	-0.00784.9400	0.2550	0.3770	29.60	0.0314	3.7000	0.3300	0.5440
9.44	-0.01024.9200	0.2570	0.3790	30.10	0.0357	3.6100	0.3390	0.5730
9.97	-0.01294.9100	0.2580	0.3820	30.60	0.0370	3.4900	0.3440	0.6140
10.50	-0.00894.8900	0.2580	0.3860	31.20	0.0460	3.3200	0.3540	0.6700
11.00	-0.00734.8800	0.2590	0.3870	31.70	0.0648	3.0800	0.3730	0.7410
11.60	-0.01004.8700	0.2580	0.3880	32.20	0.0934	2.8000	0.4040	0.8160
12.10	-0.00514.8500	0.2590	0.3900	32.70	0.1150	2.4900	0.4380	0.9010
12.60	-0.00124.8300	0.2610	0.3930	33.30	0.1340	2.2000	0.4760	0.9750
13.20	-0.00134.8200	0.2590	0.3980					
13.70	-0.00374.8000	0.2590	0.3970					
14.20	-0.00144.7800	0.2660	0.4000					
14.70	0.0013	4.7600	0.2670	0.4040				
15.30	0.0025	4.7400	0.2670	0.4070				
15.80	0.0026	4.7200	0.2660	0.4090				
16.30	0.0025	4.6900	0.2660	0.4120				
16.90	0.0035	4.6700	0.2680	0.4110				
17.40	0.0010	4.6500	0.2710	0.4120				
17.90	8.89E-4	4.6300	0.2720	0.4160				
18.40	0.0022	4.6000	0.2740	0.4180				
19.00	0.0040	4.5800	0.2800	0.4230				
19.50	0.0061	4.5500	0.2860	0.4250				
20.00	0.0107	4.5200	0.2850	0.4270				
20.60	0.0130	4.4900	0.2860	0.4280				
21.10	0.0155	4.4600	0.2870	0.4290				
21.60	0.0169	4.4300	0.2910	0.4340				
22.20	0.0169	4.4000	0.2910	0.4320				
22.70	0.0250	4.3600	0.2940	0.4350				
23.20	0.0242	4.3200	0.2970	0.4380				
23.70	0.0188	4.2800	0.2960	0.4440				
24.30	0.0217	4.2400	0.2960	0.4510				

Data points used to produce the profiles in Figure A15, along the measurement line C in Figure A12. These data are also available on the PSI ftp site under the name *N05D8posC.txt*.

The columns signify, from left to right: x [mm]; u_{mean} [m/s]; v_{mean} [m/s]; u_{rms} [m/s]; v_{rms} [m/s]

-36.10	-0.13002.3000	0.4870	1.0200	-17.60	-0.01565.0300	0.2450	0.3650
-35.60	-0.11902.5800	0.4510	0.9360	-17.00	-0.01415.0600	0.2440	0.3610
-35.00	-0.08462.9000	0.4050	0.8380	-16.50	-0.01515.0800	0.2410	0.3560
-34.50	-0.05733.1900	0.3710	0.7450	-16.00	-0.01675.1000	0.2370	0.3520
-34.00	-0.03903.4300	0.3570	0.6770	-15.40	-0.01415.1200	0.2300	0.3500
-33.50	-0.02803.6100	0.3440	0.6210	-14.90	-0.01605.1400	0.2300	0.3460
-32.90	-0.02873.7500	0.3320	0.5790	-14.40	-0.01865.1700	0.2300	0.3430
-32.40	-0.03123.8500	0.3240	0.5420	-13.90	-0.01495.1800	0.2260	0.3370
-31.90	-0.02703.9400	0.3240	0.5190	-13.30	-0.01655.2000	0.2240	0.3310
-31.30	-0.02314.0100	0.3200	0.5030	-12.80	-0.02125.2100	0.2260	0.3270
-30.80	-0.02324.0800	0.3170	0.4880	-12.30	-0.01655.2300	0.2200	0.3240
-30.30	-0.02524.1400	0.3090	0.4800	-11.70	-0.01965.2400	0.2190	0.3180
-29.70	-0.02724.1900	0.3060	0.4710	-11.20	-0.01565.2500	0.2180	0.3160
-29.20	-0.02454.2400	0.3050	0.4670	-10.70	-0.01295.2700	0.2190	0.3120
-28.70	-0.02144.2900	0.3020	0.4550	-10.10	-0.01095.2800	0.2180	0.3080
-28.20	-0.01954.3400	0.3000	0.4500	-9.62	-0.01085.2900	0.2130	0.3050
-27.60	-0.02214.3900	0.2990	0.4480	-9.09	-0.01695.2900	0.2080	0.3030
-27.10	-0.02074.4300	0.2940	0.4430	-8.56	-0.01475.3000	0.2080	0.2940
-26.60	-0.02394.4800	0.2870	0.4380	-8.03	-0.00965.3100	0.2100	0.2860
-26.00	-0.02414.5200	0.2810	0.4320	-7.50	-0.01525.3200	0.2090	0.2860
-25.50	-0.02354.5600	0.2780	0.4270	-6.97	-0.01465.3300	0.2040	0.2820
-25.00	-0.02334.6000	0.2750	0.4250	-6.44	-0.01005.3300	0.2030	0.2780
-24.40	-0.02274.6300	0.2750	0.4250	-5.91	-0.01245.3300	0.2030	0.2740
-23.90	-0.02064.6700	0.2760	0.4210	-5.38	-0.01455.3400	0.2040	0.2710
-23.40	-0.02174.7100	0.2730	0.4190	-4.85	-0.01465.3400	0.2040	0.2670
-22.90	-0.02014.7400	0.2700	0.4150	-4.32	-0.01345.3500	0.1990	0.2630
-22.30	-0.01784.7800	0.2680	0.4100	-3.80	-0.01175.3500	0.1990	0.2630
-21.80	-0.01804.8100	0.2660	0.4020	-3.27	-0.01045.3500	0.2000	0.2590
-21.30	-0.01784.8500	0.2650	0.3950	-2.74	-0.01175.3500	0.1980	0.2580
-20.70	-0.01414.8700	0.2610	0.3910	-2.21	-0.01035.3600	0.1980	0.2580
-20.20	-0.01554.9000	0.2580	0.3840	-1.68	-0.01205.3500	0.1970	0.2560
-19.70	-0.01734.9300	0.2590	0.3790	-1.15	-0.01385.3500	0.2000	0.2550
-19.20	-0.01504.9600	0.2570	0.3780	-0.62	-0.01365.3500	0.2010	0.2550
-18.60	-0.01384.9800	0.2540	0.3730	-0.09	-0.01515.3500	0.2050	0.2560
-18.10	-0.01415.0100	0.2480	0.3680	0.44	-0.01475.3500	0.2060	0.2560

0.97	-0.01475.3400	0.2050	0.2550	21.60	0.0189	4.7500	0.2550	0.4050
1.50	-0.01585.3400	0.2060	0.2540	22.20	0.0190	4.7200	0.2610	0.4090
2.03	-0.01685.3300	0.2040	0.2560	22.70	0.0189	4.6800	0.2610	0.4100
2.56	-0.01305.3300	0.2060	0.2580	23.20	0.0219	4.6500	0.2630	0.4150
3.09	-0.01295.3300	0.2070	0.2620	23.70	0.0177	4.6200	0.2620	0.4180
3.62	-0.01525.3200	0.2040	0.2650	24.30	0.0154	4.6000	0.2650	0.4190
4.15	-0.01175.3200	0.2050	0.2680	24.80	0.0158	4.5600	0.2700	0.4280
4.68	-0.01435.3100	0.2070	0.2710	25.30	0.0197	4.5300	0.2750	0.4310
5.21	-0.01405.3000	0.2090	0.2750	25.90	0.0222	4.4900	0.2820	0.4320
5.74	-0.01255.2800	0.2110	0.2800	26.40	0.0188	4.4500	0.2790	0.4380
6.27	-0.01365.2800	0.2100	0.2790	26.90	0.0209	4.4100	0.2800	0.4430
6.80	-0.01085.2600	0.2110	0.2840	27.40	0.0262	4.3700	0.2840	0.4480
7.33	-0.00945.2500	0.2110	0.2860	28.00	0.0293	4.3200	0.2900	0.4540
7.86	-0.00995.2400	0.2110	0.2910	28.50	0.0301	4.2700	0.2900	0.4550
8.38	-0.00795.2300	0.2140	0.2940	29.00	0.0273	4.2300	0.2930	0.4570
8.91	-0.00665.2200	0.2150	0.2970	29.60	0.0310	4.1800	0.2960	0.4600
9.44	-0.00685.2100	0.2190	0.3020	30.10	0.0296	4.1200	0.2970	0.4680
9.97	-0.00765.1900	0.2220	0.3060	30.60	0.0342	4.0700	0.2980	0.4780
10.50	-0.00545.1800	0.2230	0.3150	31.20	0.0390	4.0100	0.3030	0.4880
11.00	-0.00475.1700	0.2240	0.3210	31.70	0.0410	3.9400	0.3070	0.5050
11.60	-0.00355.1500	0.2260	0.3250	32.20	0.0465	3.8600	0.3070	0.5190
12.10	-0.00605.1300	0.2290	0.3250	32.70	0.0487	3.7800	0.3090	0.5290
12.60	-0.00605.1200	0.2290	0.3290	33.30	0.0495	3.6900	0.3100	0.5500
13.20	-0.00235.1000	0.2320	0.3320	33.80	0.0512	3.5800	0.3150	0.5860
13.70	7E-4 5.0800	0.2300	0.3410	34.30	0.0624	3.4300	0.3340	0.6320
14.20	-0.00275.0600	0.2280	0.3490	34.90	0.0843	3.2200	0.3620	0.6970
14.70	-0.00335.0400	0.2350	0.3500	35.40	0.1150	2.9500	0.3950	0.7900
15.30	8.08E-4 5.0200	0.2400	0.3530	35.90	0.1590	2.6500	0.4360	0.8900
15.80	0.0026 5.0100	0.2420	0.3590	36.50	0.1740	2.3500	0.4760	0.9800
16.30	0.0017 4.9900	0.2390	0.3640					
16.90	0.0070 4.9700	0.2420	0.3660					
17.40	0.0052 4.9400	0.2410	0.3720					
17.90	0.0069 4.9200	0.2430	0.3780					
18.40	0.0097 4.9000	0.2420	0.3850					
19.00	0.0160 4.8700	0.2450	0.3870					
19.50	0.0161 4.8500	0.2470	0.3860					
20.00	0.0150 4.8300	0.2480	0.3900					
20.60	0.0140 4.8000	0.2520	0.3960					
21.10	0.0159 4.7700	0.2520	0.4010					

Data points used to produce the profiles in Figure A16, along the measurement line D in Figure A12. These data are also available on the PSI ftp site under the name *N05D8posD.txt*.

The columns signify, from left to right: x [mm]; u_{mean} [m/s]; v_{mean} [m/s]; u_{rms} [m/s]; v_{rms} [m/s]

-33.50	-0.09171.8800	0.4270	1.0600	-14.90	-0.01334.7100	0.2720	0.4020
-32.90	-0.09982.1300	0.4110	0.9870	-14.40	-0.01474.7300	0.2720	0.3960
-32.40	-0.08702.4200	0.3870	0.9080	-13.90	-0.01354.7500	0.2650	0.3950
-31.90	-0.07132.7300	0.3590	0.8170	-13.30	-0.01464.7800	0.2620	0.3900
-31.30	-0.04493.0300	0.3430	0.7320	-12.80	-0.02094.7900	0.2600	0.3880
-30.80	-0.03203.2600	0.3340	0.6680	-12.30	-0.01664.8100	0.2630	0.3860
-30.30	-0.02113.4400	0.3310	0.6150	-11.70	-0.01454.8200	0.2600	0.3830
-29.70	-0.01593.5700	0.3310	0.5730	-11.20	-0.01794.8300	0.2620	0.3780
-29.20	-0.01563.6800	0.3260	0.5470	-10.70	-0.01634.8400	0.2630	0.3720
-28.70	-0.01443.7600	0.3210	0.5270	-10.10	-0.01274.8600	0.2590	0.3720
-28.20	-0.01573.8300	0.3170	0.5110	-9.62	-0.01614.8700	0.2560	0.3680
-27.60	-0.01363.9000	0.3130	0.4990	-9.09	-0.01954.8800	0.2550	0.3690
-27.10	-0.01253.9500	0.3130	0.4920	-8.56	-0.02214.8900	0.2550	0.3660
-26.60	-0.01254.0100	0.3130	0.4850	-8.03	-0.02254.9000	0.2510	0.3650
-26.00	-0.01534.0600	0.3140	0.4780	-7.50	-0.01824.9200	0.2470	0.3650
-25.50	-0.01754.1100	0.3080	0.4710	-6.97	-0.01764.9300	0.2480	0.3630
-25.00	-0.01444.1500	0.3060	0.4650	-6.44	-0.02324.9300	0.2450	0.3580
-24.40	-0.01784.1900	0.2970	0.4570	-5.91	-0.02254.9300	0.2450	0.3550
-23.90	-0.02074.2300	0.2910	0.4510	-5.38	-0.01914.9400	0.2450	0.3530
-23.40	-0.01824.2700	0.2940	0.4460	-4.85	-0.01754.9500	0.2440	0.3530
-22.90	-0.01914.3100	0.2950	0.4390	-4.32	-0.01754.9600	0.2430	0.3530
-22.30	-0.01914.3400	0.2940	0.4370	-3.80	-0.02034.9600	0.2420	0.3520
-21.80	-0.01494.3700	0.2950	0.4360	-3.27	-0.01804.9600	0.2450	0.3530
-21.30	-0.01344.4100	0.2910	0.4340	-2.74	-0.01724.9600	0.2450	0.3510
-20.70	-0.01544.4400	0.2910	0.4340	-2.21	-0.01564.9600	0.2430	0.3480
-20.20	-0.02064.4600	0.2870	0.4300	-1.68	-0.01384.9700	0.2430	0.3470
-19.70	-0.01664.4900	0.2850	0.4260	-1.15	-0.01814.9700	0.2430	0.3470
-19.20	-0.01584.5200	0.2830	0.4220	-0.62	-0.01554.9600	0.2440	0.3470
-18.60	-0.01904.5500	0.2830	0.4220	-0.09	-0.01514.9600	0.2410	0.3470
-18.10	-0.01674.5700	0.2810	0.4170	0.44	-0.01644.9600	0.2400	0.3490
-17.60	-0.00884.6000	0.2780	0.4140	0.97	-0.01554.9600	0.2380	0.3500
-17.00	-0.00914.6200	0.2730	0.4130	1.50	-0.01674.9600	0.2410	0.3500
-16.50	-0.01444.6400	0.2740	0.4080	2.03	-0.01444.9600	0.2420	0.3500
-16.00	-0.01194.6700	0.2740	0.4030	2.56	-0.01114.9500	0.2390	0.3480
-15.40	-0.01234.6900	0.2710	0.4030	3.09	-0.00984.9500	0.2450	0.3490

3.62	-0.00854.9400	0.2490 0.3470	24.30	0.0184 4.2100	0.2910 0.4390
4.15	-0.01404.9300	0.2500 0.3500	24.80	0.0196 4.1700	0.2980 0.4450
4.68	-0.01554.9300	0.2490 0.3520	25.30	0.0194 4.1300	0.3000 0.4460
5.21	-0.01364.9200	0.2520 0.3490	25.90	0.0195 4.1000	0.3010 0.4540
5.74	-0.01204.9200	0.2530 0.3480	26.40	0.0263 4.0600	0.3000 0.4620
6.27	-0.01094.9100	0.2510 0.3460	26.90	0.0309 4.0100	0.3020 0.4660
6.80	-0.01234.9000	0.2530 0.3490	27.40	0.0302 3.9600	0.3040 0.4750
7.33	-0.01444.8900	0.2540 0.3550	28.00	0.0313 3.9000	0.3060 0.4810
7.86	-0.01464.8700	0.2530 0.3570	28.50	0.0307 3.8500	0.3120 0.4900
8.38	-0.01244.8600	0.2570 0.3570	29.00	0.0294 3.7900	0.3160 0.5030
8.91	-0.01354.8500	0.2540 0.3570	29.60	0.0300 3.7200	0.3170 0.5180
9.44	-0.01024.8400	0.2540 0.3560	30.10	0.0274 3.6400	0.3200 0.5390
9.97	-0.00944.8300	0.2550 0.3610	30.60	0.0301 3.5400	0.3230 0.5660
10.50	-0.00964.8100	0.2560 0.3660	31.20	0.0328 3.4100	0.3260 0.6030
11.00	-0.00964.8000	0.2560 0.3650	31.70	0.0376 3.2200	0.3340 0.6510
11.60	-0.00954.7900	0.2560 0.3720	32.20	0.0544 2.9800	0.3470 0.7140
12.10	-0.01074.7700	0.2570 0.3760	32.70	0.0849 2.7000	0.3700 0.8010
12.60	-0.01004.7500	0.2580 0.3790	33.30	0.1060 2.3900	0.4030 0.8980
13.20	-0.00514.7400	0.2560 0.3830			
13.70	-0.00184.7200	0.2590 0.3840			
14.20	-0.00294.7000	0.2590 0.3840			
14.70	-0.00194.6900	0.2580 0.3880			
15.30	0.0026 4.6700	0.2620 0.3890			
15.80	0.0063 4.6500	0.2640 0.3920			
16.30	0.0058 4.6300	0.2650 0.3970			
16.90	0.0073 4.6100	0.2690 0.4020			
17.40	0.0082 4.5900	0.2690 0.4060			
17.90	0.0091 4.5600	0.2690 0.4110			
18.40	0.0099 4.5400	0.2710 0.4120			
19.00	0.0113 4.5200	0.2730 0.4170			
19.50	0.0113 4.4900	0.2760 0.4210			
20.00	0.0085 4.4600	0.2750 0.4210			
20.60	0.0066 4.4400	0.2790 0.4250			
21.10	0.0051 4.4100	0.2800 0.4260			
21.60	0.0075 4.3700	0.2820 0.4230			
22.20	0.0134 4.3400	0.2870 0.4230			
22.70	0.0144 4.3100	0.2910 0.4280			
23.20	0.0155 4.2800	0.2880 0.4290			
23.70	0.0169 4.2500	0.2890 0.4320			

Data points used to produce the profiles in Figure A17, along the measurement line E in Figure A12. These data are also available on the PSI ftp site under the name *N05D8posE.txt*.

The columns signify, from left to right: x [mm]; u_{mean} [m/s]; v_{mean} [m/s]; u_{rms} [m/s]; v_{rms} [m/s]

-20.70	-0.04912.2800	0.3800	0.8400	-2.21	-0.03084.0900	0.3240	0.4520	
-20.20	-0.04682.5300	0.3730	0.7930	-1.68	-0.02804.0900	0.3260	0.4500	
-19.70	-0.04552.7600	0.3700	0.7530	-1.15	-0.02674.1000	0.3260	0.4490	
-19.20	-0.03572.9700	0.3680	0.7150	-0.62	-0.02364.1000	0.3290	0.4510	
-18.60	-0.02773.1200	0.3700	0.6700	-0.09	-0.02154.1000	0.3260	0.4520	
-18.10	-0.02963.2500	0.3630	0.6290	0.44	-0.02374.1000	0.3220	0.4510	
-17.60	-0.03123.3500	0.3550	0.6020	0.97	-0.02354.1000	0.3240	0.4510	
-17.00	-0.03293.4400	0.3620	0.5800	1.50	-0.02364.1000	0.3220	0.4490	
-16.50	-0.03423.5000	0.3640	0.5650	2.03	-0.02944.1000	0.3200	0.4490	
-16.00	-0.03583.5500	0.3630	0.5510	2.56	-0.03184.0900	0.3240	0.4500	
-15.40	-0.03323.6000	0.3600	0.5360	3.09	-0.02824.0900	0.3240	0.4510	
-14.90	-0.02833.6400	0.3600	0.5220	3.62	-0.02574.0800	0.3250	0.4550	
-14.40	-0.03023.6800	0.3610	0.5140	4.15	-0.02454.0700	0.3300	0.4540	
-13.90	-0.03083.7200	0.3600	0.5150	4.68	-0.02754.0700	0.3310	0.4520	
-13.30	-0.03193.7500	0.3560	0.5110	5.21	-0.02474.0600	0.3330	0.4550	
-12.80	-0.02563.7800	0.3520	0.5010	5.74	-0.02394.0500	0.3350	0.4580	
-12.30	-0.02313.8100	0.3480	0.4970	6.27	-0.02034.0300	0.3360	0.4580	
-11.70	-0.02693.8300	0.3460	0.4900	6.80	-0.01914.0200	0.3330	0.4590	
-11.20	-0.03013.8600	0.3450	0.4850	7.33	-0.01684.0100	0.3370	0.4590	
-10.70	-0.03053.8800	0.3460	0.4810	7.86	-0.01604.0000	0.3380	0.4600	
-10.10	-0.02893.9000	0.3450	0.4770	8.38	-0.01543.9800	0.3380	0.4640	
-9.62	-0.03223.9200	0.3430	0.4740	8.91	-0.01543.9700	0.3430	0.4660	
-9.09	-0.03253.9500	0.3420	0.4720	9.44	-0.01203.9600	0.3380	0.4700	
-8.56	-0.03143.9700	0.3350	0.4690	9.97	-0.01283.9400	0.3390	0.4740	
-8.03	-0.03523.9800	0.3340	0.4660	10.50	-0.01423.9300	0.3400	0.4790	
-7.50	-0.03404.0000	0.3320	0.4600	11.00	-0.01113.9100	0.3410	0.4810	
-6.97	-0.03664.0100	0.3360	0.4580	11.60	-0.01343.8800	0.3450	0.4810	
-6.44	-0.03604.0200	0.3370	0.4590	12.10	-0.01273.8600	0.3460	0.4820	
-5.91	-0.03294.0300	0.3370	0.4600	12.60	-0.01203.8400	0.3480	0.4850	
-5.38	-0.03354.0400	0.3370	0.4600	13.20	-0.00843.8200	0.3480	0.4860	
-4.85	-0.03474.0500	0.3350	0.4570	13.70	-0.00353.8000	0.3480	0.4880	
-4.32	-0.03284.0600	0.3300	0.4550	14.20	-0.00183.7700	0.3480	0.4950	
-3.80	-0.03044.0700	0.3270	0.4570	14.70	-0.00513.7400	0.3550	0.5050	
-3.27	-0.02954.0800	0.3270	0.4520	15.30	-0.00323.7100	0.3570	0.5080	
-2.74	-0.02904.0900	0.3250	0.4490	15.80	0.0035	3.6700	0.3580	0.5140

16.30	0.0035	3.6400	0.3530	0.5260
16.90	5.93E-4	3.5900	0.3530	0.5340
17.40	0.0035	3.5500	0.3540	0.5480
17.90	0.0029	3.4900	0.3560	0.5650
18.40	0.0021	3.4200	0.3580	0.5880
19.00	0.0028	3.3400	0.3580	0.6050
19.50	0.0106	3.2300	0.3610	0.6270
20.00	0.0201	3.0900	0.3620	0.6710
20.60	0.0288	2.9200	0.3660	0.7170
21.10	0.0386	2.7200	0.3710	0.7590
21.60	0.0432	2.5100	0.3690	0.7970

ANNEX 3: NOMENCLATURE

General

BPGs	Best Practice Guidelines
CAD	Computer-Aided Design
CAPS	CSNI Activity Proposal Sheet
CFD	Computational Fluid Dynamics
CFD4NRS	Computational Fluid Dynamics for Nuclear Reactor Safety (Workshops)
CPU	Central Processing Unit
CFX	Computation Fluid dynamiX (commercial CFD software from ANSYS®)
CSNI	Committee on the Safety of Nuclear Installations
FLUENT	commercial CFD software from ANSYS®
GOthic™	Generation Of Thermal Hydraulic Information in Containments (software package)
IAEA	International Atomic Energy Agency
IBM	Immersed Boundary Method
ISP	International Standard Problem
KAERI	Korea Atomic Energy Research Institute
LDA/LDV	Laser Doppler Anemometry/Laser Doppler Velocimetry
MATiS-H	Measurements and Analysis of Turbulence in Subchannels – Horizontal
NEA	Nuclear Energy Agency
NRS	Nuclear Reactor Safety
NURETH	Topical Meeting on Nuclear Reactor Thermal Hydraulics
OECD	Organisation for Economic Cooperation and Development
OpenFOAM	Open Source Field Operation and Manipulation (open-source CFD software)
PANDA	Integral Thermal-Hydraulic Test Facility at PSI
PRG	Programme Review Group (of the CSNI)
PSI	Paul Scherrer Institute
R&D	Research and Development
rms	Root-Mean Square
STAR-CCM+®	commercial Computational Continuum Mechanics software from CD-adapco

V&V	Verification and Validation
WG	Writing Group
WGAMA	Working Group on the Analysis and Management of Accidents (of the CSNI)
X, Y, Z	Cartesian Coordinates

Variables

D_H	Hydraulic Diameter
Fr	Froude Number
Re	Reynolds Number
Sc	Schmidt Number
u, v, w	Cartesian Components of Instantaneous Velocity
u', v', w'	Cartesian Components of Fluctuating Velocity
U, V, W	Cartesian Components of Mean Velocity

Turbulence Models

LES	Large Eddy Simulation
RANS	Reynolds-Averaged Navier-Stokes
RSM	Reynolds-Stress Model
SAS	Scale-Adaptive Simulation
SGS	Sub-Grid Scale
SST	Shear Stress Transport
URANS	Unsteady RANS
WALE	Wall-Adapting Local Eddy viscosity

ANNEX 4: COMMENTS FROM PARTICIPANTS

User U11

Benchmarking against PIV is quite helpful to understand the model results and separate error sources. However, in the present case it needs to be performed quite carefully considering the following two observations which may also relativize punctual ‘good’ or ‘bad’ model rankings.

- Velocity profiles obtained by URANS models: It should be considered that the erosion progression is non-linear at the beginning ($t < 1000$ s). Consequently, the arithmetic average of the PIV measurements is not identical to the instantaneous profile in the middle of the averaging period ($\Delta t = 204$ s). This requires that the same averaging procedure is performed for the simulation to allow for a direct comparison. Temporal averaging was not explicitly requested for the PIV comparison and not necessary for URANS simulations (in contrast to LES). Consequently, there might be a systematic discrepancy due to post processing and not model error in the comparison which should be avoided in open evaluations.
- Comparison of velocity profiles: Generally, the present flow characteristic is transient, i.e. a comparison or rating of velocity profiles is only meaningful if the elevation of the jet position (stagnation point, see ‘HeDrop’, Fig. 5.1) is comparable to the experiment. Vice versa, this difference between experiment and simulation may help to understand deviations in the profiles.

User U45

- The sensitivity studies done have revealed a high dependence on the mesh size close to the injection nozzle outlet, where the jet is developed.
- In post-test calculations, it has been demonstrated that with an adequate mesh around the jet, and simulating the heat transfer in the walls, the results with GOTHIC 8.0 fit the experimental data, even with a very coarse mesh compared to other simulations.